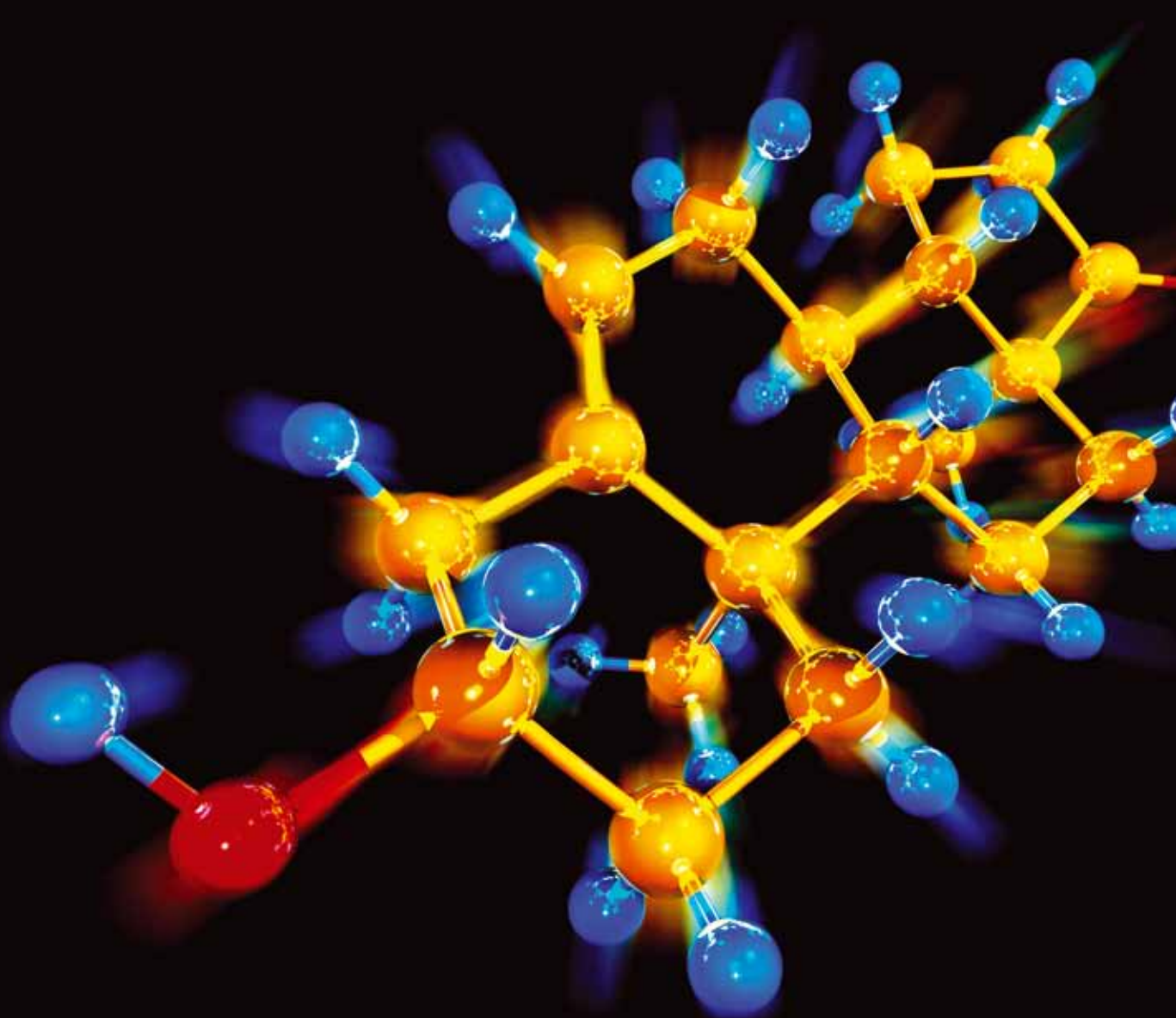


Functionalized Nanocomposites for Environmental Applications

Guest Editors: Tifeng Jiao, Lavinia Balan, Xinqing Chen,
and Qingrui Zhang





Functionalized Nanocomposites for Environmental Applications

Journal of Chemistry

Functionalized Nanocomposites for Environmental Applications

Guest Editors: Tifeng Jiao, Lavinia Balan, Xinqing Chen, and Qingrui Zhang



Copyright © 2014 Hindawi Publishing Corporation. All rights reserved.

This is a special issue published in "Journal of Chemistry." All articles are open access articles distributed under the Creative Commons Attribution License, which permits unrestricted use, distribution, and reproduction in any medium, provided the original work is properly cited.

Contents

Functionalized Nanocomposites for Environmental Applications, Tifeng Jiao, Lavinia Balan, Xinqing Chen, and Qingrui Zhang
Volume 2014, Article ID 419458, 1 page

Degradation of Typical Indoor Air Pollutants Using Fe-Doped TiO₂ Thin Film under Daylight Illumination, Shuaijie Wang, Hao Yu, and Xingxing Cheng
Volume 2014, Article ID 829892, 5 pages

The Preparation of Glucan-Fe₃O₄ Magnetic Nanoparticles and Its In Vivo Distribution in Mice, Fengdan Jin
Volume 2014, Article ID 603267, 4 pages

Different Surfactants-Assisted Hydrothermal Fabrication and Photocatalytic Properties of Bi₂MoO₆ for Methylene Blue Degradation under Simulated Sunlight Irradiation, Wenfeng Guo, Heping Li, Haisheng Ma, and Weixiu Teng
Volume 2014, Article ID 436485, 5 pages

Preparation and Magnetic Properties of Anisotropic (Sm,Pr)Co₅/Fe Nanocomposites Particles via Electroless Plating, Shi Wang, Jin-Ming Ma, and Yan Chen
Volume 2014, Article ID 842495, 5 pages

Preparation and Its Adsorptive Property of Modified Expanded Graphite Nanomaterials, Liqin Wang, Xiujun Fu, E. Chang, Haitao Wu, Kun Zhang, Xianchao Lei, Ruijun Zhang, Xiaowen Qi, and Yulin Yang
Volume 2014, Article ID 678151, 5 pages

Photosensitizers from Spirulina for Solar Cell, Liqui Wang, Liang Tian, Xinxin Deng, Mengyi Zhang, Shuping Sun, Wei Zhang, and Lin Zhao
Volume 2014, Article ID 430806, 5 pages

Adsorption of Monobutyl Phthalate from Aqueous Phase onto Two Macroporous Anion-Exchange Resins, Zhengwen Xu, Yunlong Zhao, Jing Shi, Jiangang Lu, Ling Cheng, and Mindong Chen
Volume 2014, Article ID 689734, 5 pages

Investigation on the Structure and Electrochemical Properties of La-Ce-Mg-Al-Ni Hydrogen Storage Alloy, Yuqing Qiao, Jianyi Xi, Minshou Zhao, Guangjie Shao, Yongchun Luo, and Limin Wang
Volume 2013, Article ID 627582, 6 pages

A Novel Absorbent of Nano-Fe Loaded Biomass Char and Its Enhanced Adsorption Capacity for Phosphate in Water, Hongguang Zhou, Zhenmao Jiang, and Shiqiang Wei
Volume 2013, Article ID 649868, 9 pages

Mesoporous Metal-Containing Carbon Nitrides for Improved Photocatalytic Activities, Jie Luo, Zhao-Jie Cui, and Guo-Long Zang
Volume 2013, Article ID 945348, 6 pages

Electrochemiluminescent Detection of Hydrogen Peroxide via Some Luminol Imide Derivatives with Different Substituent Groups, Tifeng Jiao, Qinjin Huang, Yong Xiao, Xihai Shen, Jingxin Zhou, and Faming Gao
Volume 2013, Article ID 375372, 6 pages

Editorial

Functionalized Nanocomposites for Environmental Applications

Tifeng Jiao,¹ Lavinia Balan,² Xinqing Chen,³ and Qingrui Zhang⁴

¹ School of Environmental and Chemical Engineering, Yanshan University, Qinhuangdao 066004, China

² Institute of Materials Science of Mulhouse (IS2M), 15 Rue Jean Starcky, P.O. Box 2488, 68057 Mulhouse Cedex, France

³ Department of Chemical and Biomolecular Engineering, Hong Kong University of Science and Technology, Clear Water Bay, Kowloon, Hong Kong

⁴ Department of Environmental Engineering, Yanshan University, Qinhuangdao 066004, China

Correspondence should be addressed to Tifeng Jiao; tfjiao@ysu.edu.cn

Received 4 March 2014; Accepted 4 March 2014; Published 26 March 2014

Copyright © 2014 Tifeng Jiao et al. This is an open access article distributed under the Creative Commons Attribution License, which permits unrestricted use, distribution, and reproduction in any medium, provided the original work is properly cited.

During the last decades, using functionalized nanocomposites with nanoscale precision represents one of the most important bottom-up approaches for nanotechnology and has become a major issue in the field of environmental chemistry. The chemical functionalization and self-assemblies of nanocomposites and subsequent environmental applications of well-defined micro-/nanostructures have multiple important impacts upon various areas. In this sense, the sophisticated nanocomposites with multiple components have deepened the insight of nanomaterials and enriched the content of environmental chemistry.

This special issue addresses the research studies on the functionalized process and environmental applications of nanocomposites. It contains eleven selected research articles. Z. Xu et al. prepared the adsorption performance of monobutyl phthalate onto macroporous base anion-exchange resins. H. Zhou et al. reported a new absorbent of Fe loaded biomass char and investigated the enhanced adsorption capacity for phosphate in water. J. Luo et al. prepared the synthesis of mesoporous Fe contained g-C₃N₄ (m-Fe-C₃N₄) photocatalyst by using SiO₂ nanoparticles as hard template and dicyandiamide as precursor and investigated the photocatalytic activity of photodegradation of Rhodamine. B. S. Wang et al. reported the preparation of iron-doped titania thin film by means of sol-gel method to degrade typical indoor air pollutants under daylight illumination. L. Wang et al. reported the use of living spirulina as novel photosensitizer to construct spirulina biosolar cell. T. Jiao et al. prepared the design of some luminol imide

derivatives with different substituent groups and investigated the electrochemiluminescent detection of hydrogen peroxide with a view of developing new biosensors. F. Jin reported the preparation of glucan-Fe₃O₄ magnetic nanoparticles and in vivo distribution in mice. L. Wang et al. prepared modified expanded graphite samples and measured the sorption capacity for some oils. W. Guo et al. prepared Bi₂MoO₆ single-crystallites by hydrothermal method in the presence of different surfactants and measured the photocatalytic activities for the degradation of methylene blue. Y. Qiao et al. demonstrated the investigation on the structure and electrochemical characteristics of La-Ce-Mg-Al-Ni hydrogen storage alloy. S. Wang et al. reported the preparation and magnetic properties of anisotropic (Sm,Pr)Co₅/Fe nanocomposites particles by electroless plating. The effect of Fe content on the magnetic properties of the magnets is also discussed.

Altogether, the guest editors would like to express sincere appreciation to all the authors for their contribution. Moreover, thanks are extended to all reviewers for their time spent on enhancing the quality of these papers.

Tifeng Jiao
Lavinia Balan
Xinqing Chen
Qingrui Zhang

Research Article

Degradation of Typical Indoor Air Pollutants Using Fe-Doped TiO₂ Thin Film under Daylight Illumination

Shuaijie Wang, Hao Yu, and Xingxing Cheng

School of Environmental and Chemical Engineering, Yanshan University, Qinhuangdao 066004, China

Correspondence should be addressed to Shuaijie Wang; wangshuaijie@ysu.edu.cn

Received 22 November 2013; Accepted 24 January 2014; Published 2 March 2014

Academic Editor: Lavinia Balan

Copyright © 2014 Shuaijie Wang et al. This is an open access article distributed under the Creative Commons Attribution License, which permits unrestricted use, distribution, and reproduction in any medium, provided the original work is properly cited.

A type of iron-doped titania thin film was prepared by means of sol-gel method to degrade indoor formaldehyde (HCHO), ammonia (NH₃), and benzene (C₆H₆) under sunlight. The photocatalysts were characterized by X-ray diffraction (XRD), scanning electron microscopy (SEM), UV-Vis spectroscopy, and energy dispersive spectra (EDS). The results showed that the iron was doped in the TiO₂ photocatalyst successfully. The absorption edge of doped TiO₂ had red shifts and the doped TiO₂ had a stronger absorption than the pure TiO₂ in the visible region. Fe-doped TiO₂ thin film prepared with the optimal preparation condition could remove indoor HCHO, NH₃ and C₆H₆ effectively under solar light irradiation. The removal percentage of HCHO, NH₃ or C₆H₆ after 9 h photocatalytic reaction under solar light reached 55%, 53.1%, and 37.5%, respectively, when they existed in the air individually. When the three pollutants were mixed in the air, the removal percentage decreased to 33.3%, 28.3%, and 28%. The degradation reaction of the three pollutants followed the pseudo first-order kinetics, which reflects that the photocatalytic reaction was controlled by the surface chemical reaction and the reaction rate was controlled by concentration of reactants.

1. Introduction

People are paying more and more attention to the pollution caused by indoor decoration with the improvement of living standard and indoor decoration gradually becoming popular [1–3]. Among the numerous indoor air pollutants, formaldehyde, ammonia, and benzene are the most representatives, which come from the furnishings and decorating materials, causing nausea, chest tightness, wheezing, skin rashes, allergic reaction, and chronic poisoning [4, 5].

Photocatalysis technology has been proved to be potentially advantageous for indoor air purification [6], and titania is the most common used photocatalyst for its high photocatalytic activity, stable physical and chemical properties, low cost, and nontoxicity [7–9]. However, with its high-energy band gap (ca. 3.0 eV for rutile and 3.2 eV for anatase), titania photocatalysis reacts only under ultraviolet light. But the ultraviolet light energy only accounts for 4%–6% of solar energy reaching the ground, so the solar energy cannot be utilized efficiently in the photocatalytic process [10–12]. In addition, the high degree for recombination between

photogenerated electron-hole pairs restricts the large-scale application of titania.

Doping is one of the important methods of improving visible light photocatalytic activity of titania [13–15]. Transition metal dopants have been widely used to improve the photoefficiency of the electronic process as well as the response to the visible part of the spectrum. Kim et al. reported that Fe-doped TiO₂ could extend the spectral response to the visible region and the photocatalytic activity was greatly enhanced [16]. Choi et al. conducted a systematic study of metal ions doping into TiO₂ for 21 metal ions. Among various transition metal ions, Fe³⁺ was considered to be a successful doping element due to its half-filled electronic configuration [17].

In this paper, Fe-doped TiO₂ photocatalysts were attempted to degrade three typical indoor air pollutants: formaldehyde, ammonia, and benzene under daylight illumination. Usually, formaldehyde, ammonia, and TVOC exist in the indoor air at the same time, but there are few reports on the photocatalytic degradation of mixed indoor air pollutants. So, we not only studied the photocatalytic degradation of formaldehyde, ammonia, and benzene

when they exist in indoor air separately, but also studied photocatalytic degradation of the mixed formaldehyde, ammonia, and benzene in the indoor air. To avoid TiO_2 powder suspending in the indoor air, the Fe-doped TiO_2 thin films were prepared with flat glass as carrier. The research finding provides a feasible way for enhancement of indoor air quality.

2. Materials and Methods

2.1. Photocatalyst Preparation. Pure and Fe-doped TiO_2 thin films were prepared by sol-gel technique. The sol was prepared with tetrabutyl titanate as precursor, anhydrous ethanol as solvent, deionized water or $\text{Fe}(\text{NO}_3)_3$ solution as reactive substance, and glacial acetic acid as stabilizer. 7 mL of tetrabutyl titanate was dissolved in 50 mL of anhydrous ethanol. The mixed solution was sealed with plastic wrap and stirred for 0.5 h at room temperature to form solution 1. 14 mL glacial acetic acid was dropped into solution 1 with constant stirring for 0.5 h in air to form solution 2. Then 6 mL deionized water or $\text{Fe}(\text{NO}_3)_3$ solution of different concentrations was added dropwise in solution 2 within 60 min under vigorous stirring at room temperature to form the sol, followed by aging for 24 h to prepare the gel. The plate glass was inserted vertically into the gel. After keeping 10 seconds, it was pulled out of the gel with the speed of 12 cm/min. Thus, the gel film was formed on the glass surface. Then the glass coated with the sol was dried for 20 min at 100°C. At last, the glass was calcined for 2 h at 500°C (20°C/min).

2.2. Photocatalyst Characterization. The crystal structure of pure and Fe-doped TiO_2 was determined by a D-max-2500/PC X-ray diffractometer (XRD) equipped with Cu-K α radiation. Morphology of Fe-doped TiO_2 thin film was examined by HITACHI (Japan) S-4800 scanning electron microscopy (SEM). The ultraviolet-visible (UV-Vis) absorption spectra of pure and Fe-doped TiO_2 thin films were recorded on a Shimadzu (Japan) UV-2550 spectrophotometer. The energy dispersive spectra of the Fe-doped TiO_2 thin film were recorded on JEM-2010 transmission electron microscopy (TEM).

2.3. Degradation Test of Gaseous Indoor Pollutants. The degradation test was performed on a self-designed, cuboid, airtight, glass reactor ($60 \times 60 \times 20$ cm) with a hole, which was connected to sampling tube of KC-6D air sampler. An electric fan was installed on the bracket of the airtight reactor in order to circulate the mixture of pollutants (individual formaldehyde, ammonia, benzene, or the mixture of three pollutants) and air. Eight pieces of coated glass were placed vertically and evenly in the reactor. A predetermined amount of formaldehyde was injected in vessel under dark. The photoreactor was then kept in darkness for 2 h to allow the adsorption of formaldehyde into photocatalyst to approach the state of equilibrium. The photoreactor was then exposed to sunlight to activate the photocatalytic degradation. The experiments were carried out in good sunny days of summer (June to July) with a maximum temperature of 30°C (between

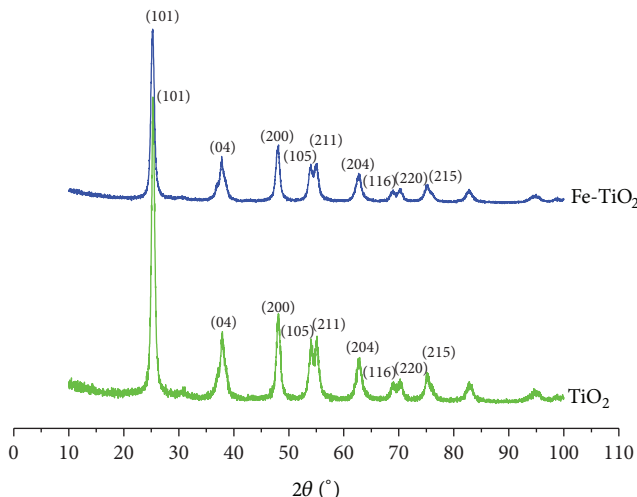


FIGURE 1: XRD spectra of TiO_2 catalysts.

8 a.m. to 5 p.m.). The intensity of indoor sunlight was in the range between 500 and 1000 lux. The concentration of formaldehyde, ammonia, and benzene was periodically measured every 60 min. The formaldehyde concentration was measured with the 3-methyl-2-benzothiazolinone hydrazone hydrochloride (MBTH) spectrophotometric method. The ammonia concentration was measured with Nessler's reagent spectrophotometric method. The benzene concentration was measured by the benzene detector.

3. Results and Discussion

3.1. Results of Characterization

3.1.1. XRD Spectra. Figure 1 shows the XRD patterns of undoped TiO_2 and Fe-doped TiO_2 with the doping proportion (mole ratio) which is 1.00%. The result showed that both samples had anatase structure mainly with the formation of characteristic diffraction peaks at $2\theta = 25.28^\circ$, 37.80° , 48.05° , 53.89° , 55.06° , and 62.69° , corresponding to (101), (04), (200), (105), (211), and (204) crystal surface. Compared to undoped TiO_2 , the patterns of Fe-doped TiO_2 became weak and broadening, which indicated that the crystallite sizes decreased. From the obtained XRD peaks the crystallite size of the catalysts was determined by applying Scherrer's formula. The formula is given below:

$$D = \frac{0.89\lambda}{(\beta \cdot \cos \theta)}, \quad (1)$$

where D = crystallite size (nm), λ = X-ray wavelength (1.5406 Å), β = width of the obtained peak at half maximum, and θ = contour peak angle (radian). According to Scherrer's formula, the crystallite size of Fe-doped TiO_2 was 13.1 nm, which was less than that of undoped TiO_2 14.6 nm.

3.1.2. SEM Image. Figure 2 shows the SEM photograph of Fe-doped TiO_2 thin film with the doping proportion (mole ratio)

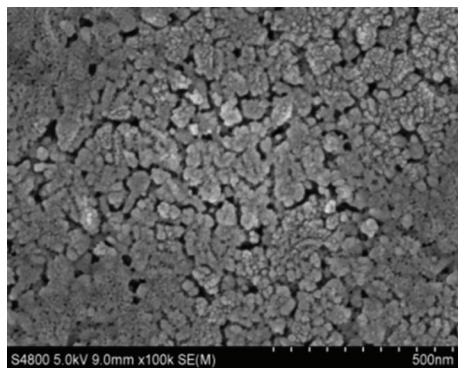


FIGURE 2: SEM photograph of Fe-doped TiO₂ thin film.

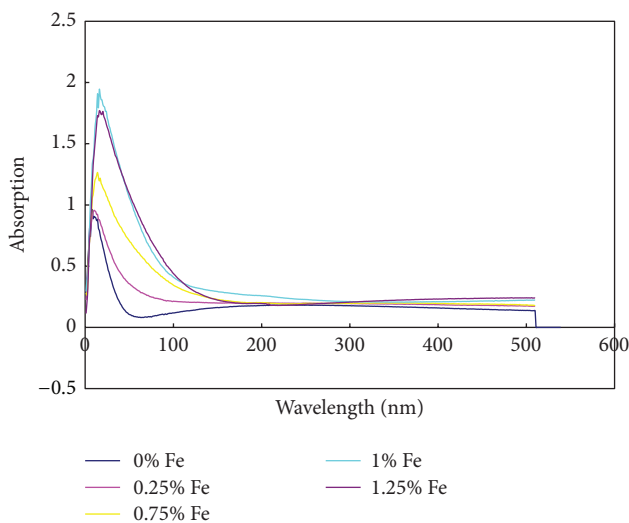


FIGURE 3: UV-Vis absorption spectra.

which is 1.00%. From the image, the thin film was coated on the plate glass smoothly and uniformly.

3.1.3. UV-Vis Spectra of Photocatalyst. Figure 3 shows the ultraviolet-visible (UV-Vis) absorption spectra of the undoped and different Fe-doped TiO₂ thin films (the doping mole ratios are 0.25%, 0.75%, 1.00%, and 1.25%). According to Figure 3, the absorption edge of Fe-doped TiO₂ has red shifts and the doped TiO₂ has a stronger absorption than the pure TiO₂ in the visible region. Since doped TiO₂ can absorb light in a wider range of wavelength and use more light energy than undoped TiO₂, a high photocatalytic activity should be expected.

3.1.4. EDS Spectra. Figure 4 shows the energy dispersive spectra of the Fe-doped TiO₂ thin films with the doping proportion (mole ratio) which is 1.00%. The result showed that the iron was doped in the TiO₂ photocatalyst successfully, and the mole ratio of Fe and Ti was very close to 1%.

TABLE 1: Degradation ratios of individual formaldehyde, ammonia, and benzene.

Iron dopant amount (mole fraction) %	Degradation ratio of HCHO (%)	Degradation ratio of NH ₃ (%)	Degradation ratio of C ₆ H ₆ (%)
0	35.2	39.5	26
0.25	37.1	41.0	28.6
0.75	40.4	50.3	35.2
1.00	55.0	53.1	37.5
1.25	38.9	46.2	34.2

3.2. Photocatalytic Experiment

3.2.1. Degradation of Individual Formaldehyde, Ammonia, and Benzene. Table 1 shows the degradation ratios of formaldehyde, ammonia, and benzene after 9 h photocatalytic reaction under solar light when they exist in air individually. The results showed that the photocatalytic activities of Fe-doped TiO₂ thin films were higher than pure TiO₂ thin film and the photocatalytic activity of Fe-doped TiO₂ thin film increased with the doping amount of iron when iron dopant amount was smaller than 1.00%. When the doping amount of iron was 1.00%, the photocatalytic activity was the highest. The degradation ratios of formaldehyde, ammonia, and benzene reached 55%, 53.1%, and 37.5%, respectively. This is due to the fact that new impurity levels are introduced between the conduction and valence bands; with the substitution for Ti⁴⁺ by Fe³⁺ in the structure of TiO₂, the electrons can be promoted from the valence band to these impurity levels [18]. It can induce more photogenerated electrons and holes to participate in the photocatalytic reactions. So Fe-doped TiO₂ has narrowed band gap than pure TiO₂ and could increase the absorption in the visible-light region, which is consistent with the result of UV-Vis absorption spectra analysis. Besides, Fe³⁺ can effectively inhibit the recombination of photogenerated electrons and holes and enhance the photocatalytic activity. But the photocatalytic activity of Fe-doped TiO₂ reduced when the mole fraction of Fe³⁺ was more than 1%, because the excess amounts of Fe³⁺ might cover the surface of TiO₂, increased the number of recombination centers, decreased the photo quantum efficiency, and led to low photoactivity.

3.2.2. Degradation of the Mixture of Formaldehyde, Ammonia, and Benzene. Since the photocatalytic activity of Fe-doped TiO₂ thin film with the doping amount of iron was 1.00% which was the highest, the photocatalytic degradation experiment of mixed formaldehyde, ammonia, and benzene was conducted with this optimal Fe-doped TiO₂ thin film. The results showed that although the three pollutants were mixed in the air, they were still removed effectively after 9 h photocatalytic reaction under solar light. The degradation ratios of formaldehyde, ammonia, and benzene in gas mixture were 33.3%, 28.3%, and 28% separately, but they were lower than the degradation ratios of formaldehyde, ammonia, and benzene existing in air separately (55.0%, 53.1%, and 37.5%). This is due to the fact that gas molecules occupy fully the

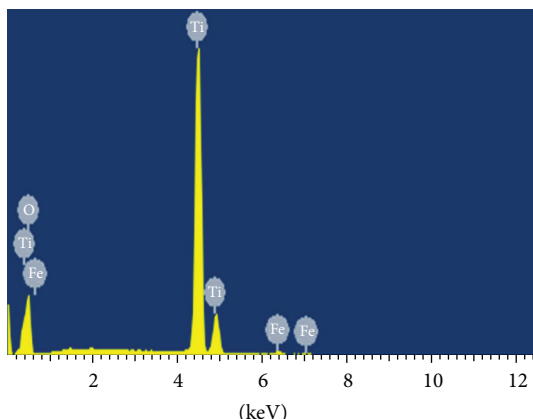


FIGURE 4: EDS spectra.

active sites of the photocatalyst, different molecules compete with each other, and the intermediate product of different pollutant accumulating on the photocatalyst surface prevents the effective contact of gas molecules and photocatalyst.

3.2.3. Kinetics of Photocatalytic Reaction. Formaldehyde, ammonia, and benzene exist in the indoor air at the same time usually, so the kinetics of photocatalytic reaction was studied with the experimental data of mixed pollutants over the optimal designed Fe-doped TiO_2 thin film; that is, Fe(III) dopant amount was 1%. Langmuir-Hinshelwood (L-H) equation has been widely used to describe the process of photocatalytic reaction. At low reactant concentration, which is a reasonable assumption for most indoor air pollution problems, the L-H model is simplified to a pseudo first-order expression:

$$\ln\left(\frac{C}{C_0}\right) = -kt, \quad (2)$$

where the reactant residue (C/C_0) is a ratio of the instantaneous concentration of gaseous formaldehyde(C) to the initial concentration (C_0), k is the reaction rate constant that is determined by linear regression of the data $\ln(C/C_0)$ versus the exposure time (t). The experimental data were fitted by plotting $-\ln(C/C_0)$ against irradiation time. The fitting result was shown in Figure 5.

From Figure 5, we could see that the degradation reaction of formaldehyde, ammonia, and benzene followed the pseudo first-order kinetics with the correlation coefficient $R^2 = 0.96$, 0.98 , and 0.99 , respectively. The reaction rate constants of formaldehyde, ammonia, and benzene were 0.043 h^{-1} , 0.035 h^{-1} , and 0.035 h^{-1} , respectively. This shows that the photocatalytic reaction is controlled by surface chemical reaction and reaction rate is controlled by reactant concentration.

4. Conclusions

The Fe-doped TiO_2 thin film was prepared by means of sol-gel method. The solar light catalytic activity of TiO_2

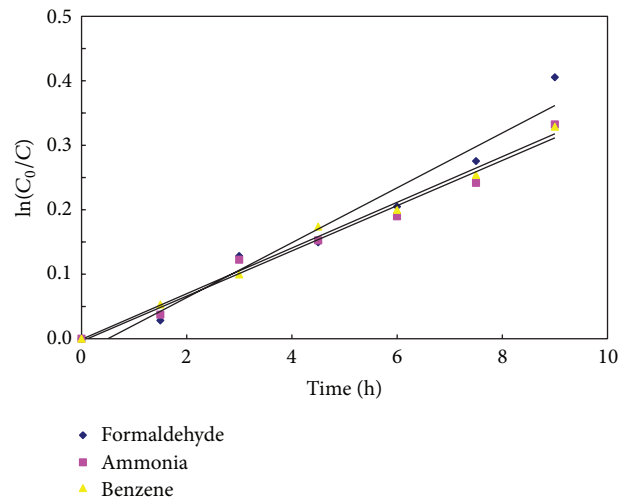


FIGURE 5: Kinetics of degradation reaction of the mixed pollutants.

was improved significantly by doping with iron (III). Using the optimal Fe-doped TiO_2 photocatalyst, the formaldehyde, ammonia, and benzene could be removed effectively whether existing separately or mixedly in the air. But the degradation ratios of formaldehyde, ammonia, and benzene in gas mixture after 9 h photocatalytic reaction under solar light (33.3%, 28.3%, and 28%) were lower than those of formaldehyde, ammonia, and benzene existing in air individually (55%, 53.1%, and 37.5%). So the photocatalytic degradation of indoor air pollutants using solar light is very promising. The photocatalytic degradation reaction kinetic of three pollutants followed the pseudo first-order kinetic model, the photocatalytic reaction was controlled by the surface chemical reaction, and the reaction rate was controlled by concentration of reactants.

Conflict of Interests

The authors declare that there is no conflict of interests regarding the publication of this paper.

Acknowledgments

The authors greatly acknowledge the financial support from the Tianjin North China Geological Exploration Bureau Research Project and the Hebei Postdoctoral Science Foundation.

References

- [1] Y. Lu, W. Li, W. Wang, and C. Ma, "Combination of activated carbon with TiO_2 for the photodegradation of indoor formaldehyde (I)," *Acta Energiae Solaris Sinica*, vol. 29, no. 1, pp. 114–118, 2008.
- [2] J. Yang, D. Li, Z. Zhang, Q. Li, and H. Wang, "A study of the photocatalytic oxidation of formaldehyde on $\text{Pt}/\text{Fe}_2\text{O}_3/\text{TiO}_2$," *Journal of Photochemistry and Photobiology A*, vol. 137, no. 2-3, pp. 197–202, 2000.

- [3] Z. Wang, Z. Bai, H. Yu, J. Zhang, and T. Zhu, "Regulatory standards related to building energy conservation and indoor-air-quality during rapid urbanization in China," *Energy and Buildings*, vol. 36, no. 12, pp. 1299–1308, 2004.
- [4] Y. Zhao, B. Chen, Y. Guo, F. Peng, and J. Zhao, "Indoor air environment of residential buildings in Dalian, China," *Energy and Buildings*, vol. 36, no. 12, pp. 1235–1239, 2004.
- [5] Y. Feng, S. Wen, X. Wang et al., "Indoor and outdoor carbonyl compounds in the hotel ballrooms in Guangzhou, China," *Atmospheric Environment*, vol. 38, no. 1, pp. 103–112, 2004.
- [6] W. H. Ching, M. Leung, and D. Y. C. Leung, "Solar photocatalytic degradation of gaseous formaldehyde by sol-gel TiO₂ thin film for enhancement of indoor air quality," *Solar Energy*, vol. 77, no. 2, pp. 129–135, 2004.
- [7] K. Hashimoto, H. Irie, and A. Fujishima, "TiO₂ photocatalysis: a historical overview and future prospects," *Japanese Journal of Applied Physics*, vol. 44, no. 12, pp. 8269–8285, 2005.
- [8] N. Nishikawa, S. Kaneko, H. Katsumata et al., "Photocatalytic degradation of allergens in water with titanium dioxide," *Fresenius Environmental Bulletin*, vol. 16, no. 3, pp. 310–314, 2007.
- [9] D. V. Kozlov, E. A. Paukshtis, and E. N. Savinov, "The comparative studies of titanium dioxide in gas-phase ethanol photocatalytic oxidation by the FTIR *in situ* method," *Applied Catalysis B*, vol. 24, no. 1, pp. L7–L12, 2000.
- [10] X. Hong, Z. Wang, W. Cai et al., "Visible-light-activated nanoparticle photocatalyst of iodine-doped titanium dioxide," *Chemistry of Materials*, vol. 17, no. 6, pp. 1548–1552, 2005.
- [11] S. Sakthivel and H. Kisch, "Daylight photocatalysis by carbon-modified titanium dioxide," *Angewandte Chemie—International Edition*, vol. 42, no. 40, pp. 4908–4911, 2003.
- [12] X.-Z. Shen, Z.-C. Liu, S.-M. Xie, and J. Guo, "Degradation of nitrobenzene using titania photocatalyst co-doped with nitrogen and cerium under visible light illumination," *Journal of Hazardous Materials*, vol. 162, no. 2–3, pp. 1193–1198, 2009.
- [13] R. Asahi, T. Morikawa, T. Ohwaki, K. Aoki, and Y. Tage, "Visible-lightphotocatalysis in nitrogen-doped titanium oxides," *Science*, vol. 293, pp. 269–271, 2001.
- [14] L. Siamiolo, M. Valigi, D. Gazzoli, and R. Amadelli, "Photo-electro catalytic oxidation of aromatic alcohols on visible light-absorbing nitrogen-doped TiO₂," *Electrochimica Acta*, vol. 55, no. 26, pp. 7788–7795, 2010.
- [15] W. Zhao, W. Ma, C. Chen, J. Zhao, and Z. Shuai, "Efficient degradation of toxic organic pollutants with Ni₂O₃/TiO_{2-x}B_x under visible irradiation," *Journal of the American Chemical Society*, vol. 126, no. 15, pp. 4782–4783, 2004.
- [16] D. H. Kim, H. S. Hong, S. J. Kim, J. S. Song, and K. S. Lee, "Photocatalytic behaviors and structural characterization of nanocrystalline Fe-doped TiO₂ synthesized by mechanical alloying," *Journal of Alloys and Compounds*, vol. 375, no. 1–2, pp. 259–264, 2004.
- [17] W. Choi, A. Termin, and M. R. Hoffmann, "The role of metal ion dopants in quantum-sized TiO₂: correlation between photoreactivity and charge carrier recombination dynamics," *Journal of Physical Chemistry*, vol. 98, no. 51, pp. 13669–13679, 1994.
- [18] Q. Wang, S. Xu, and F. Shen, "Preparation and characterization of TiO₂ photocatalysts co-doped with iron (III) and lanthanum for the degradation of organic pollutants," *Applied Surface Science*, vol. 257, no. 17, pp. 7671–7677, 2011.

Research Article

The Preparation of Glucan- Fe_3O_4 Magnetic Nanoparticles and Its In Vivo Distribution in Mice

Fengdan Jin

Key Laboratory of Applied Chemistry, Yanshan University, Qinhuangdao, Hebei 066004, China

Correspondence should be addressed to Fengdan Jin; fengdanjin@ysu.edu.cn

Received 30 October 2013; Revised 31 December 2013; Accepted 5 January 2014; Published 23 February 2014

Academic Editor: Lavinia Balan

Copyright © 2014 Fengdan Jin. This is an open access article distributed under the Creative Commons Attribution License, which permits unrestricted use, distribution, and reproduction in any medium, provided the original work is properly cited.

The glucan- Fe_3O_4 magnetic nanoparticles were prepared by hydrothermal method. The mixture of FeCl_2 and glucan was stirred vigorously for half an hour under low temperature (15°C). KOH of 1 mol/L was dropwise added, slowly, into the solution until the pH to 12. Immediately, KNO_3 was added and the temperature was raised to 75°C for an hour. All the processes of Fe_3O_4 crystal particles generation were under nitrogen. An atomic absorption spectrometry quantitative analysis method was built to determine the in vivo distribution of the glucan- Fe_3O_4 magnetic nanoparticles in mice. The diameter of glucan- Fe_3O_4 magnetic nanoparticles was about 25 nm and they were taken up by the liver primarily after intravenous administration via the tail.

1. Introduction

Magnetic induction heating treatment of cancer is a new development of heat treatment in recent years. Fe_3O_4 has a high specific surface area and a strong tendency to aggregate. It can reduce the surface energy of the particle by surface modification. It is the most widely used nanomagnetic materials in magnetic hyperthermia [1–3]. Wang et al. found that the Fe_3O_4 magnetic fluid demonstrates excellent stability and fast magnetotemperature response, which can be used both in magnetic resonance imaging and magnetic fluid hyperthermia [4]. Glucan can adjust the biocompatibility and response characteristics of the magnetic nanoparticles by modifying its surface, and therefore it could meet different aspects of the application requirements in biotechnology, medicine, and pharmaceuticals [5]. Research for the process of absorption, distribution, metabolism, and clearance in vivo of glucan- Fe_3O_4 magnetic nanoparticles can more fully investigate its effects and safety in vivo.

The biological effects and biological safety of nanomedicine are very important. In the development of nanotechnology, while simultaneously carrying out its safety studies, nanotechnology has the potential to become the first new technologies that benefit for humanity which were carefully evaluated before a negative effect even occurs [6, 7]. It is an important research direction for nanomaterials to

study the process of absorption, distribution, metabolism, and clearance in vivo and the mechanism of interaction between various nanomaterials and biomechanism of the target organ. Currently, due to the restriction of qualitative and quantitative detection to the nanoscale materials organism in vivo, these experimental data was little. This work requires long-term accumulation and development to establish and improve the research system.

Glucan- Fe_3O_4 magnetic nanoparticles were prepared by hydrothermal method and an atomic absorption spectrometry was built to investigate the distribution of glucan- Fe_3O_4 magnetic nanoparticles in mice tissue.

2. Materials and Methods

2.1. Preparation of Glucan- Fe_3O_4 . 0.01 mol of $\text{FeCl}_2 \cdot 4\text{H}_2\text{O}$ was dissolved in 20 mL of deionized degassing water. It was poured into a solution containing 10 g of glucan. The mixture was stirred vigorously for half an hour under low temperature (15°C). Then, KOH (1 mol/L) was dropwise added into the solution slowly (0.003 mol/min) until the pH of the solution was increased to 10~12. Immediately, the temperature was raised to 75°C and 10 mL KNO_3 solution (250 mg) was added rapidly. The mixture was stirred for an hour. Finally, ferrous salt is oxidized to Fe_3O_4 crystal particles and a black colloid

was generated. All the processes of Fe_3O_4 crystal particles generation were under nitrogen. The chemical reaction equation is



The obtained black product was transferred to a beaker and adjusted to $\text{pH} = 7.0$ with 0.1 mol/L of hydrochloric acid. An NdFeB magnet was placed under the bottom of the beaker. After all of the particles sedimentation, the supernatant was decanted. The sediment was washed by deionized water 5 times repeatedly. The magnetic nanoparticles were purified with a $0.22\ \mu\text{m}$ membrane filter (the purpose is to remove large particles unmodified) and were freeze-dried to powder.

2.2. Animal Experiments. The mice were injected with glucan- Fe_3O_4 nanoparticles solution (after high temperature sterilization) according to the dose of 5.68 mg/kg. The control group was injected with normal saline. After administration of 0, 0.25, 0.5, 1, 3, 6, 12, 24, and 48 h, the mice were killed by cervical dislocation, dissected out heart, liver, spleen, lung, and kidney of each mouse. Each organization was weighed accurately and placed in digestion tanks, added 4 mL of HNO_3 (65%) and 0.5 mL of H_2O_2 (30%) and microwave digestion. The residue was cooling for a while and was diluted to 10 mL. The samples were determined in AA-7000 atomic absorption spectrophotometer (Shimadzu, Japan) at the atomic absorption wavelength of 258.9 nm, the spectral passband of 0.7 nm, and the operating current of 10 mA. The increased quantity of Fe in various organs after administration was obtained by the Fe content in various organs at each time minus the Fe content in corresponding organs of the control group. It was converted into the increased quantity of Fe_3O_4 in various organs after administration. The targeted rate in various organs was calculated by

$$\frac{\text{the increased } \text{Fe}_3\text{O}_4 \text{ in an organ at } t \text{ time}}{\text{the increased } \text{Fe}_3\text{O}_4 \text{ in the sum organs at } t \text{ time}} \times 100\%. \quad (2)$$

3. Results and Discussion

3.1. Preparation of Glucan- Fe_3O_4 . Preparation methods of magnetic nanoparticles were precipitation, oxidation, and microemulsion [8, 9]. Hydrothermal method was chosen because of the products narrow size distribution and low degree of aggregation.

To improve the experimental conditions, the dosage of glucan, KOH and KNO_3 and the experimental temperature were investigated. Dispersant effect of the surfactant was mainly in its adjustment of particle surface wettability. The concentration of surfactant is critical to this adjustment. When the quantity of glucan was less, glucan coated thin, and the soft agglomeration phenomenon occurred. The repulsive force (V_R) generated between the surfactants is insufficient to overcome the Van der Waal attractive force (V_A) between the magnetic particles and the magnetic attraction force (V_N). The macromolecule glucan was used as surfactant, and the electrostatic repulsion force between the particles was

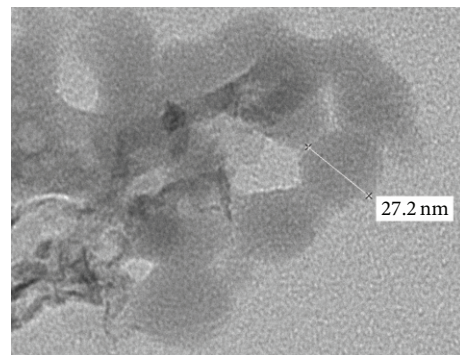


FIGURE 1: TEM of glucan- Fe_3O_4 nanoparticles.

composed of the electrostatic double layer repulsion force and steric effect. With the increase of the quantity of glucan, the glucan layer was thicker. The two repulsions force increased, and a barrier was formed which the V_A and V_N were difficult to penetrate. So, the particles were scattered well and covered well, and the number of nucleations increased, resulting in the fact that the average particle size was smaller. Excess glucan caused the coating layer to be thicker. The interaction between the polymer chains could not be ignored. Not only the particle sizes increased, but also the subsequent washing process became more difficult. When the glucan was less than 10 g, the products were layered. When the glucan was from 10 g to 15 g, there was little difference in the nanoparticle size and the morphology.

The magnetic particles were obtained by Fe^{2+} oxidized with weak oxidant KNO_3 under alkaline conditions. Slightly higher temperature and excess KOH were the suitable conditions for production of Fe_3O_4 magnetic nanoparticles. To temperature, the results showed that the oxidation reaction was difficult when the temperature was below 60°C, and a large number of black precipitates were produced when the temperature was too high (80°C). So, the temperature was set to 75°C in the oxidized process. The pH of the reaction system was changed to 8, a layered brown suspension was obtained, to 10, a black uniformly dispersed suspension was obtained, and, to 12, a black uniformly dispersed suspension was obtained. So, pH value was set to 10. Visible, in this condition (temperature was 75°C, pH value was 10), the smallest particle size was obtained.

3.2. Characterization of Glucan- Fe_3O_4

3.2.1. Transmission Electron Microscopy (TEM) and Atomic Force Microscope (AFM). The freeze-dried powder of magnetic nanoparticles was diluted into corresponding concentration solutions. They were pipetted a drop of liquid drops in the microgrid holes (for TEM) and mica sheet (for AFM), respectively, and dried by airing. The size and morphology of the products were examined by HT7650 transmission electron microscopy (Hitachi; Japan) and Multimode 8 atomic force microscope (Veeco; USA). The nanoparticles were in spherical shape with no agglomeration of particles. The dispersion was very uniform. The size of glucan- Fe_3O_4

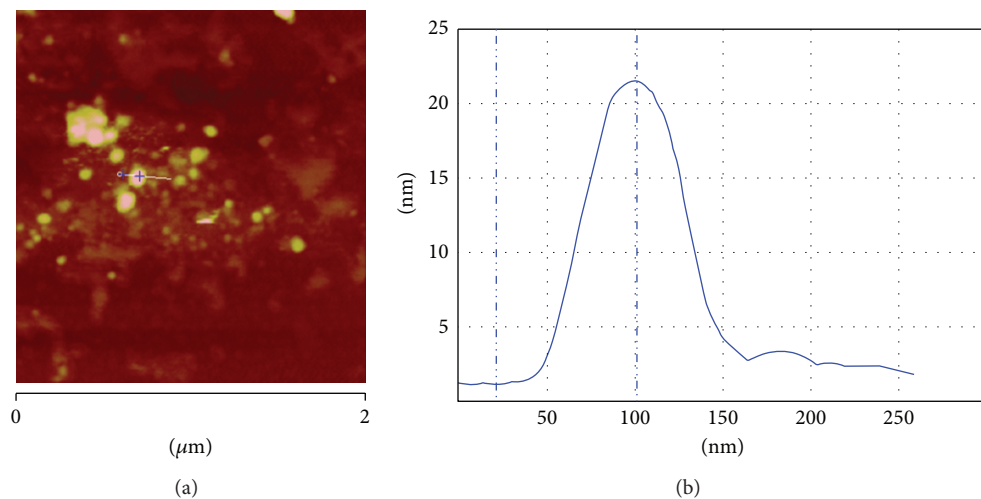


FIGURE 2: AFM of the glucan- Fe_3O_4 nanoparticles: the height of the selected particle in (a) was shown in (b).

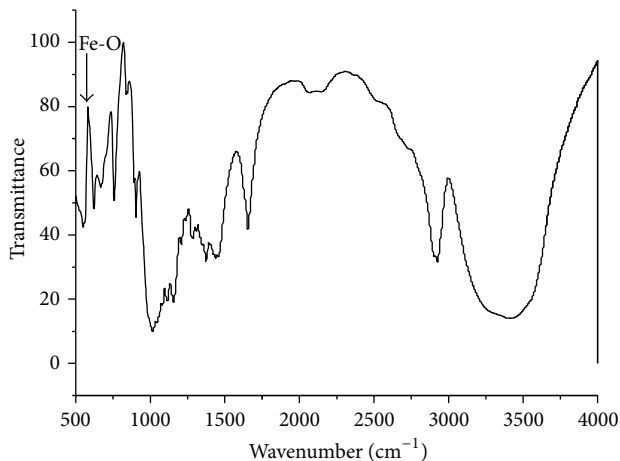


FIGURE 3: Infrared absorption spectrum of the glucan- Fe_3O_4 nanoparticles.

magnetic nanoparticles was calculated by Nano Measurer 1.2.5. The particle size was about 25 nm (Figures 1 and 2).

3.2.2. Infrared Absorption Spectrum (IR). The freeze-dried powder of magnetic nanoparticles and glucan-40 were pressed into tablets with KBr, respectively. The infrared absorption was examined by Nicolet iS10 FT-IR (Thermo Fisher Scientific, USA). The result was shown in Figure 3. The magnetic nanoparticle has a strong absorption peak in $\sigma 580 \text{ cm}^{-1}$ which was the Fe-O stretching vibration peak. The IR spectra characteristic absorption peaks of glucan were reflected at the magnetic nanoparticles, especially in $\sigma 1,000\text{--}1,200 \text{ cm}^{-1}$ fingerprint region. Since magnetic nanoparticles have been cleaned several times after the synthesis, the not coated glucan-40 could not subside to bottom of the beaker by the magnet. However, the obvious characteristic peaks of glucan appeared in the IR spectra of the final products. This proved that the prepared magnetic nanoparticles have been covered with glucan.

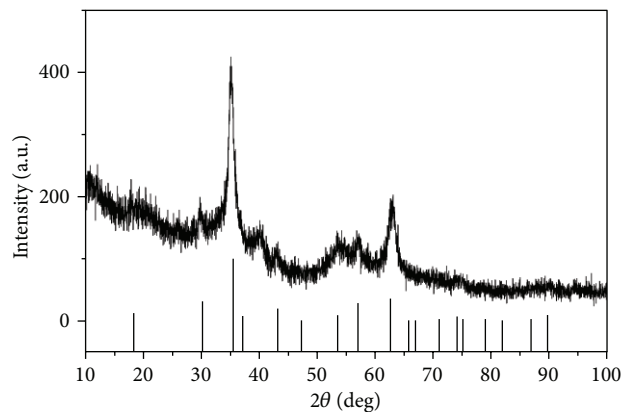


FIGURE 4: XRD of the glucan- Fe_3O_4 nanoparticles.

TABLE 1: The recovery of atomic absorption spectrometry method ($n = 5$).

Tissue	Content of Fe ($\mu\text{g}/\text{mg}$)	Added (μg)	Found (μg)	Recovery (%)	RSD (%)
Heart	22.9	2.0	24.6	98.6	1.0
		10.0	10.0	99.8	1.1
Liver	41.6	2.0	43.3	99.3	1.6
		10.0	10.1	100.6	2.3
Spleen	39.7	2.0	41.4	99.4	1.5
		10.0	10.1	100.6	1.4
Lung	18.6	2.0	20.4	98.9	2.1
		10.0	10.0	100.3	2.7
Kidney	18.9	2.0	20.8	99.5	2.8
		10.0	9.9	98.7	1.8

3.2.3. X-Ray Diffraction (XRD). The information of composition of the materials and the structure or morphology of atoms or molecules can be obtained by a D/max-2500/PC X-ray diffractometer (Rigaku Corporation; Japan). Measurement result was shown in Figure 4. The characteristic

TABLE 2: The distribution of the glucan- Fe_3O_4 nanoparticles in mice at different sampling points (% ID/g, $n = 6$).

Tissue	0 min	0.25 h	0.5 h	1 h	3 h	6 h	12 h	24 h	48 h
Heart	3.21	0.94	0.75	1.65	0.68	7.98	8.45	6.42	5.42
Liver	25.46	20.75	14.52	47.25	10.45	14.16	24.87	12.65	7.64
Spleen	9.24	18.57	16.81	10.34	12.73	11.41	19.67	16.34	12.98
Lung	13.61	3.21	6.14	2.46	2.11	3.98	3.14	3.51	5.68
Kidney	1.72	0.43	0.34	0.51	0.65	1.99	1.81	2.31	3.57

peaks of various crystal faces in the map (2.968, 2.535, 2.103, 1.719, 1.614, 1.478, and 1.271) were consistent completely with the Fe_3O_4 characteristic peaks in XRD pattern of the standard PDF card (JCPDS card number 19-0629) provided by International Powder Federation. This indicates that the prepared magnetic nanoparticles were Fe_3O_4 .

3.3. Method Validation of Atomic Absorption Spectrometry. The stock solution was formulated by spectral pure Fe liquid. Fe standard series solutions (1.00, 2.00, 3.00, and 4.00 $\mu\text{g/mL}$) were determined according to the working conditions of the instrument, establishing a standard curve automatically by the instrument. Regression equation was $Y = 5.9876X + 3.2654$. The correlation coefficient was 0.9992. Intraday precision was less than 4% interday precision was less than 6% of the various organs. The recovery data of the method was described in Table 1. The glucan- Fe_3O_4 magnetic liquid was made for immediate use. The 2 h satbility of the liquid was 1.26%. From these results, the distribution of Fe in mice was reliable and accurate.

3.4. The Distribution of Glucan- Fe_3O_4 . The tissue distribution of glucan- Fe_3O_4 at different times was shown in Table 2. The distribution was different in Fe_3O_4 in tissues and organs. The concentration was more in liver and spleen. Liver and spleen might be its target organ *in vivo*. The targeted rate in liver at 1 h after administration was 47.25%. Furthermore, the time of the distribution peak of Fe_3O_4 in various tissues and organs was different. In the heart and liver, the concentration peak was at 7 h and 48 h. The distribution curve in the spleen changed wavy. The concentration was higher at 0.25 h and 12 h and then decreased gradually. In the lungs, the concentration was great at the moment of administration and decreased rapidly. Then it was at a certain level with no significant fluctuations.

4. Conclusions

The present study described the successful preparation method of glucan- Fe_3O_4 magnetic nanoparticles and the particle size is about 25 nm. Also, the development of simple, sensitive, selective, and rapid atomic absorption spectrometry quantitative analysis method for the accurate determination of Fe_3O_4 in mice's tissues was formulated. The tissue distribution data was conducive to investigate the actions and safety *in vivo* of nanoparticles.

Conflict of Interests

The author declares that there is no conflict of interests regarding the publication of this paper.

Acknowledgments

Financial support from the National Natural Science Foundation of China (Grant 51202213), Excellent Young Scientist Funding of Hebei Province (Grant Y2012005), and Qinhuangdao city Science & Technology Research & Development Program (no. 201001A120) is acknowledged.

References

- [1] W. Pon-On, S. Meejoo, and I.-M. Tang, "Substitution of manganese and iron into hydroxyapatite: core/shell nanoparticles," *Materials Research Bulletin*, vol. 43, no. 8-9, pp. 2137–2144, 2008.
- [2] F.-Y. Cheng, C.-H. Su, Y.-S. Yang et al., "Characterization of aqueous dispersions of Fe_3O_4 nanoparticles and their biomedical applications," *Biomaterials*, vol. 26, no. 7, pp. 729–738, 2005.
- [3] A. A. Gouda and Z. Al. Mallah, "Development and validation of sensitive spectrophotometric method for determination of two antiepileptics in pharmaceutical formulations," *Spectrochimica Acta A*, vol. 105, pp. 488–496, 2013.
- [4] Y. M. Wang, X. Cao, G. H. Liu et al., "Synthesis of Fe_3O_4 magnetic fluid used for magnetic resonance imaging and hyperthermia," *Journal of Magnetism and Magnetic Materials*, vol. 323, no. 23, pp. 2953–2959, 2011.
- [5] X. L. Li, K. L. Yao, and Z. L. Liu, "CFD study on the magnetic fluid delivering in the vessel in high-gradient magnetic field," *Journal of Magnetism and Magnetic Materials*, vol. 320, no. 11, pp. 1753–1758, 2008.
- [6] Y. L. Zhao, *Nanotoxicology, in Encyclopedia of Nanoscience and Nanotechnology*, American Scientific, Stevenson Ranch, Calif, USA, 2005.
- [7] E. J. Furlani and E. P. Furlani, "A model for predicting magnetic targeting of multifunctional particles in the microvasculature," *Journal of Magnetism and Magnetic Materials*, vol. 312, no. 1, pp. 187–193, 2007.
- [8] R. Y. Hong, J. H. Li, H. Z. Li, J. Ding, Y. Zheng, and D. G. Wei, "Synthesis of Fe_3O_4 nanoparticles without inert gas protection used as precursors of magnetic fluids," *Journal of Magnetism and Magnetic Materials*, vol. 320, no. 9, pp. 1605–1614, 2008.
- [9] Y. Zhao, Z. Qiu, and J. Huang, "Preparation and analysis of Fe_3O_4 magnetic nanoparticles used as targeted drug carriers," *Chinese Journal of Chemical Engineering*, vol. 16, no. 3, pp. 451–455, 2008.

Research Article

Different Surfactants-Assisted Hydrothermal Fabrication and Photocatalytic Properties of Bi_2MoO_6 for Methylene Blue Degradation under Simulated Sunlight Irradiation

Wenfeng Guo,^{1,2} Heping Li,¹ Haisheng Ma,¹ and Weixiu Teng¹

¹ Hebei Key Laboratory of Applied Chemistry, School of Environmental and Chemical Engineering, Yanshan University, Qinhuangdao 066004, China

² State Key Laboratory of Metastable Materials Science and Technology, Yanshan University, Qinhuangdao 066004, China

Correspondence should be addressed to Wenfeng Guo; wfguo@ysu.edu.cn

Received 8 November 2013; Accepted 16 December 2013; Published 19 February 2014

Academic Editor: Xinqing Chen

Copyright © 2014 Wenfeng Guo et al. This is an open access article distributed under the Creative Commons Attribution License, which permits unrestricted use, distribution, and reproduction in any medium, provided the original work is properly cited.

Bi_2MoO_6 single-crystallites were synthesized by a simple hydrothermal method in the presence of surfactant sodium dodecyl sulfate (SDS), polyvinyl pyrrolidone (PVP), or cetyl trimethyl ammonium bromide (CTAB). The samples were characterized by X-ray diffraction (XRD), transmission electron microscopy (TEM), and ultraviolet-visible diffuse reflectance spectra (UV-vis DRS) techniques. The photocatalytic activities of the as-fabricated Bi_2MoO_6 samples were measured for the degradation of methylene blue (MB) under the Xe light illumination. It is shown that the introduction of surfactant have a crucial influence on the size and morphology of the Bi_2MoO_6 product. Among the as-fabricated Bi_2MoO_6 samples, the ones derived hydrothermally with CTAB showed outstanding photocatalytic activities for the addressed reaction under simulated sunlight irradiation, attributed to the ultrafine nanocrystals and the higher surface areas.

1. Introduction

Recently, many Aurivillius-based compounds [1] have been reported which exhibit interesting properties suitable for photocatalytic applications. Bismuth molybdates have the general chemical formula $\text{Bi}_2\text{O}_3 \cdot n\text{MoO}_3$ where $n = 3, 2$ or 1 , corresponding to the α - $\text{Bi}_2\text{Mo}_3\text{O}_{12}$, β - $\text{Bi}_2\text{Mo}_2\text{O}_9$, and γ - Bi_2MoO_6 . Among this family, γ - Bi_2MoO_6 with Aurivillius structure is the simplest and probably the most studied example.

It was well known that the microstructure and morphology of photocatalysts are important factors affecting photocatalytic properties [2]. Various synthesis methods of γ - Bi_2MoO_6 have been reported, including hard template method [3], solution combustion method [4], ultrasonic-assisted synthesis [5], citrate complex method [6], coprecipitation method [7], and hydrothermal synthesis [8, 9]. Within them, the hydrothermal route is one of the most effective methods for synthesizing γ - Bi_2MoO_6 nanostructures. This process can be described as a reaction of precursors in a close system in the presence of a solvent. It is possible to control the

shape and size of products by adjusting the processing parameters, such as different solvents and reactants, surfactants, reaction temperature, and time [10–12]. Different surfactants used in this approach were effective to fabricate nanoparticles with controllable phases and morphologies, and thus to affect the property of the product. In this paper, γ - Bi_2MoO_6 is synthesized by a simple hydrothermal method, the influence of surfactants SDS, PVP and CTAB on the microstructure, morphology, and photocatalytic activities of the catalysts is investigated. It is found that the γ - Bi_2MoO_6 synthesized in the presence of surfactant CTAB exhibits an excellent photocatalytic activity in the decomposition of MB under simulated sunlight irradiation (500-W Xe light illumination).

2. Experimental

2.1. Materials. Bismuth nitrate, sodium molybdate, MB, sodium hydroxide, nitric acid, absolute alcohol, SDS, PVP, and CTAB were provided by Sinopharm Chemical Reagent

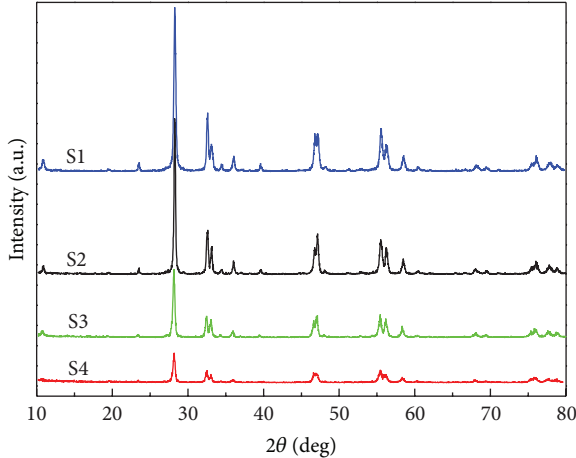


FIGURE 1: XRD patterns of S1–S4 samples.

Co., Ltd. (Shanghai, China). All chemicals were of analytic grade and used without treating further for purification.

2.2. Preparation of the Bi_2MoO_6 Sample. $\gamma\text{-Bi}_2\text{MoO}_6$ were prepared by a simple hydrothermal synthesis. Briefly, while stirring, $\text{Bi}(\text{NO}_3)_3 \cdot 5\text{H}_2\text{O}$ (1.947 g) was dissolved in 10 mL nitric acid solution (2 mol/L) to form solution A. Then, 0.483 g Na_2MoO_4 was dissolved in 10 mL sodium hydroxide solution (4 mol/L) under stirring to form solution B. Thirdly, solution B was dropwised into solution A to form homogeneous solution C. 0.189 g of SDS, PVP, and CTAB was added into solution C, respectively. The pH = 5 values of the solution were then adjusted with concentrated sodium hydroxide under stirring. After being vigorously stirred for 30 min, the resulting precursor suspension was transferred into a 50 mL capacity Teflon-lined stainless steel autoclave, which was subsequently heated to 180°C and maintained for 22 h. Subsequently, the autoclave was cooled to room temperature naturally. The obtained samples were filtered, washed with deionized water for several times, and dried at 80°C in air. The sample obtained without surfactant was denoted as S1, and the samples obtained by adding SDS, PVP, and CTAB were denoted as S2, S3, and S4, respectively.

2.3. Characterization. X-ray powder diffraction (XRD) patterns were recorded on a Shimadzu XRD-6000 X-ray diffractometer ($\text{Cu K}\alpha$ source) at a scan rate of 4°/min with the 2θ range from 20° to 80°. The crystal size was estimated from the Scherrer equation, $D = K\lambda/\text{FWHM} \cos \theta$, where D is the crystal size, λ is the wavelength of the X-ray radiation, and K is usually taken as 0.9, FWHM is the full width at half maximum in radian of the sample. Transmission electron microscopy (TEM) images were recorded on a JEOL JEM-2010 transmission electron microscope at an accelerating voltage of 200 kV. UV-visible absorption spectra and diffuse reflectance spectra (DRS) were recorded on a Lambda 2500 UV-visible spectrophotometer (Japan island ferry).

2.4. Photocatalytic Degradation of MB Experiment. MB was used as a convenient photostable organic molecule to assay

photochemical activity of $\gamma\text{-Bi}_2\text{MoO}_6$. The prepared $\gamma\text{-Bi}_2\text{MoO}_6$ samples (50 mg) were dispersed into an aqueous solution (100 mL) of MB (10 mg/L⁻¹). The suspension was sonicated for 30 min, followed by stirring in the dark for 120 min to ensure adsorption-desorption equilibrium prior to irradiation. The suspension was then irradiated while stirring by using a 500-W Xe lamp (MAX-302, Asahi Spectra, USA). The initial and final reaction temperatures for MB solution were measured as 25 ± 3°C, respectively. Samples for analysis were taken from the reaction suspension after different reaction time and centrifuged at 3500 rpm for 10 min to remove the particles. The MB concentration from the upper clear solution was analyzed according to the absorption intensity at 664 nm in the measured UV-vis spectra.

3. Results and Discussion

3.1. XRD Analysis. The XRD technique was used to identify the crystalline phases of the as-prepared $\gamma\text{-Bi}_2\text{MoO}_6$ samples, and the XRD patterns are shown in Figure 1. By comparing the XRD pattern of the standard $\gamma\text{-Bi}_2\text{MoO}_6$ sample (JCPDS PDF# 72-1524 or 71-2086), it can be realized that all of the Bragg diffraction peaks of each as-fabricated bismuth molybdate sample in the 2θ range of 10–80° could be well indexed, as indicated in Figure 1 (S1–S4). In other words, all of the $\gamma\text{-Bi}_2\text{MoO}_6$ samples were single-phase and possessed an orthogonal crystal structure, in good consistency with the results reported by other researchers [7, 8, 13]. For four Bi_2MoO_6 samples, there were some discrepancies in peak intensity, indicating that the $\gamma\text{-Bi}_2\text{MoO}_6$ crystallinity was a little different from sample to sample, depending upon the fabrication conditions adopted.

3.2. TEM Analysis. Figure 2 shows the TEM images of the as-prepared $\gamma\text{-Bi}_2\text{MoO}_6$ without or with surfactants. The TEM image in Figure 2(a) shows that bigger $\gamma\text{-Bi}_2\text{MoO}_6$ aggregated particles are composed of sheet-like nanocrystals without any surfactant. In Figure 2(b), the as-prepared $\gamma\text{-Bi}_2\text{MoO}_6$ with SDS is self-organized into a bigger branch-like architecture with irregular morphology. The TEM image in Figure 2(c)

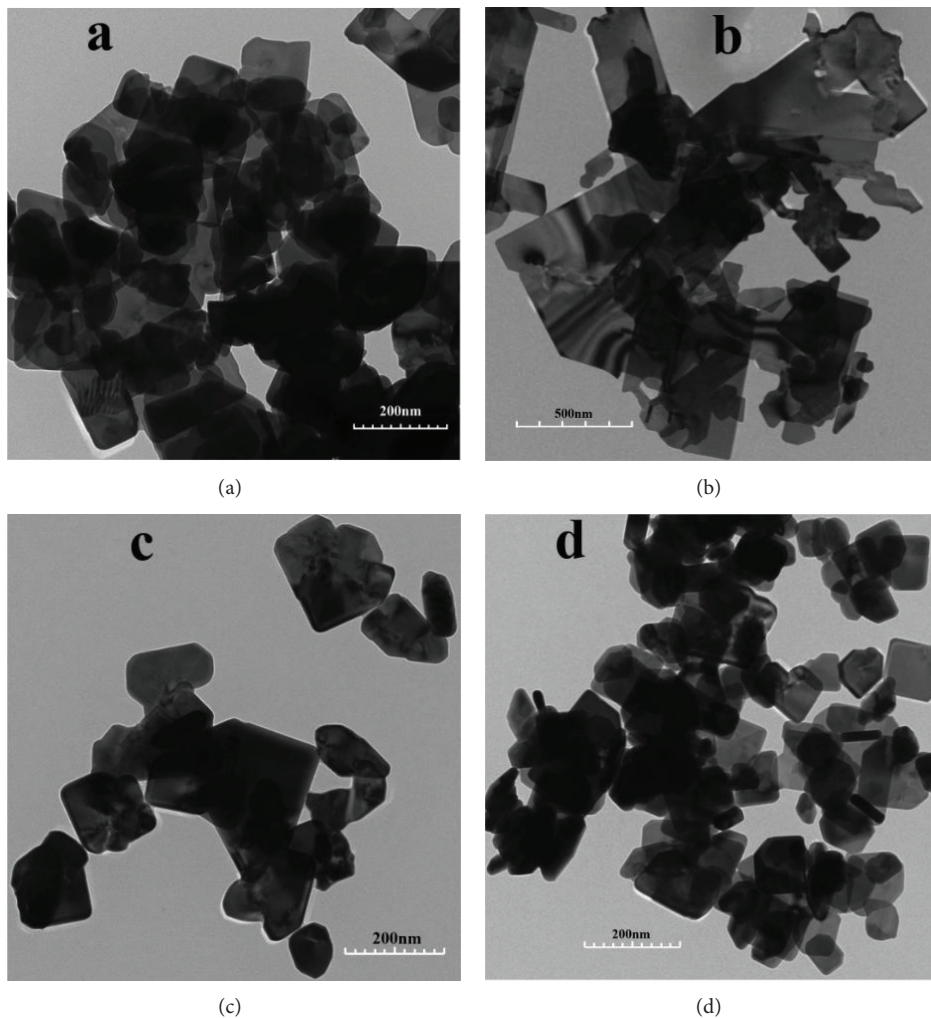


FIGURE 2: TEM images of the various photocatalysts: (a) S1, (b) S2, (c) S3, and (d) S4, respectively.

shows that the γ - Bi_2MoO_6 is composed of nanosheets with different sizes when adding PVP surfactant. Figure 2(d) shows that the TEM images of the γ - Bi_2MoO_6 assisted by CTAB are composed of smaller nanocrystals with thinner sheet-like and regular morphology. It is concluded that surfactants affect the morphology and the particle size of γ - Bi_2MoO_6 during the hydrothermal process.

3.3. Photocatalytic Activities. To demonstrate the photocatalytic activity, MB was chosen as photodegradation target under simulated sunlight irradiation. Figure 3 showed the time-dependent absorption spectra of MB solution during the photodegradation process in the presence of different γ - Bi_2MoO_6 samples (S1–S4). The absorption peaks at 664 nm corresponding to MB diminished gradually as the irradiation time extended. Compared with the absorption peaks in S2 and S1, those in S3 and S4 dramatically decreased and completely disappeared after about 90 min, in particular that in S4. It suggested that S4 exhibited the highest photocatalytic activity among all the γ - Bi_2MoO_6 samples. The variation of

MB concentrations (C/C_0) with irradiation time over the different γ - Bi_2MoO_6 samples was shown in Figure 4, where C_0 and C are the concentrations of MB solution before irradiation and after the irradiation. For comparison, direct photolysis of MB in the absence of γ - Bi_2MoO_6 was performed under the same conditions. It was clearly seen that MB concentration in the absence of the catalysts hardly changed with the increase of irradiation time. The as-synthesized γ - Bi_2MoO_6 products with different surfactants exhibited remarkable variation in photocatalytic activities for MB degradation. Under Xe lamp irradiation within 90 min, the MB photocatalytic degradation ratio (98% and 96.1%) is achieved by S4 and S3 samples, noticeably better photocatalytic activities than the S2 and S1. Among γ - Bi_2MoO_6 products, S4 exhibited superior photocatalytic activity than other products. It was mainly because photocatalytic activities increased with the decrease of the particle size. The probable mechanism is that the surface area of small particle size provides more active sites during the photocatalytic process [14, 15]. The superior activity of S4 might be ascribed to its relatively small particle size by CTAB assisted growth.

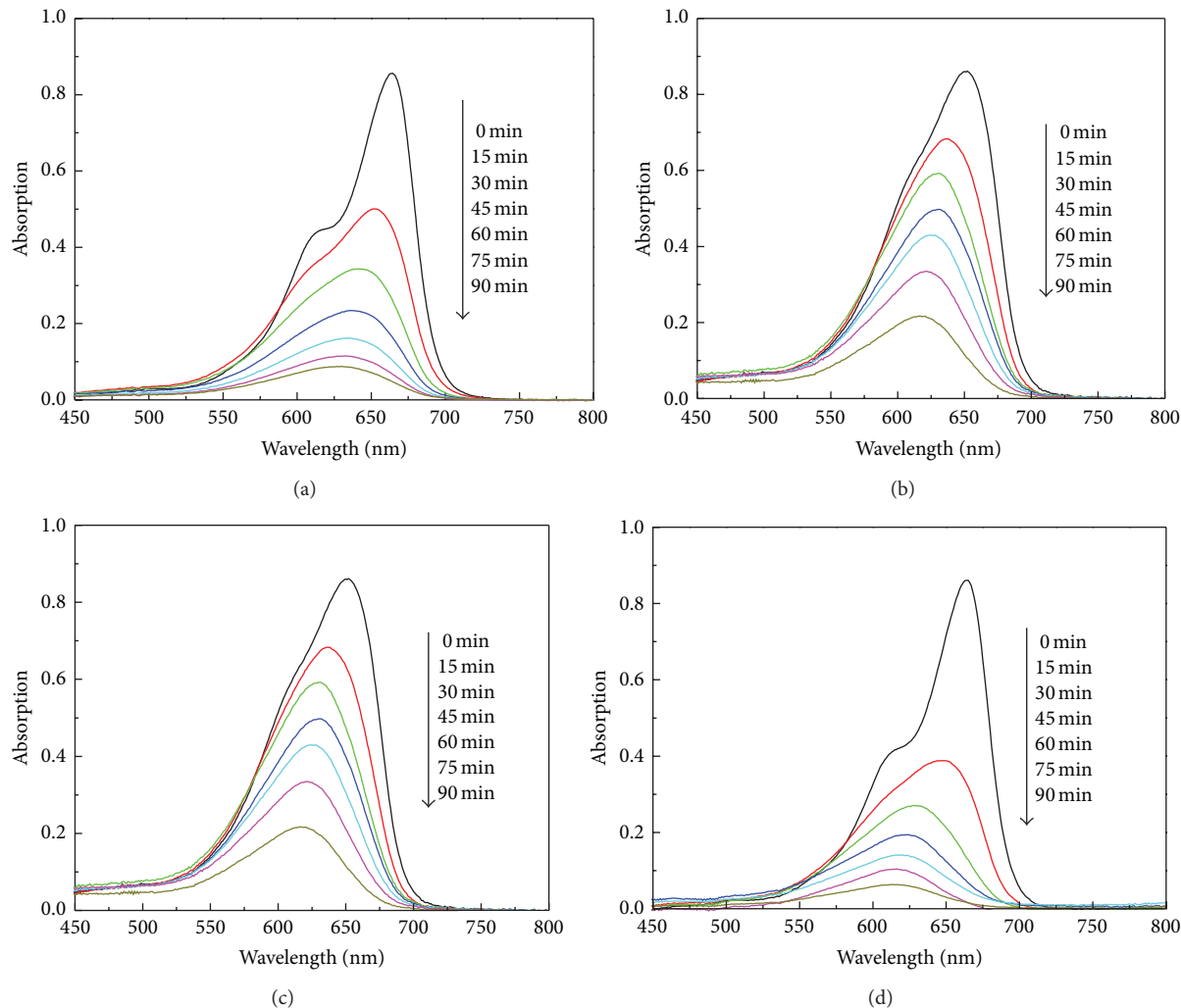


FIGURE 3: UV-vis absorption spectra of the MB solution in the presence of various photocatalysts under simulated sunlight irradiation: (a) S1, (b) S2, (c) S3, and (d) S4, respectively.

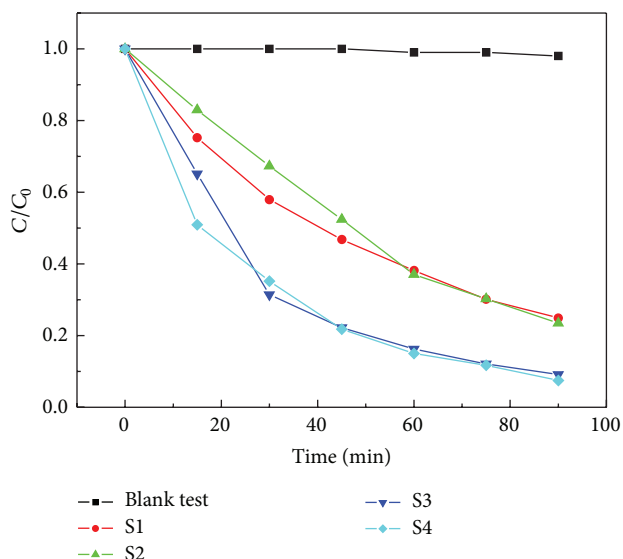


FIGURE 4: Photocatalytic degradation ratio of MB versus irradiation time by using various photocatalysts.

4. Conclusion

In conclusion, γ -Bi₂MoO₆ was synthesized by a simple hydrothermal method in the presence of surfactants SDS, PVP, and CTAB. The surfactants can affect the particle size, surface area, morphology, and the photocatalytic activity of γ -Bi₂MoO₆. It is also found that surfactant CTAB has a promotive effect on the photocatalytic activity of γ -Bi₂MoO₆ sample, due to the surface area of small particle size providing more active sites during the photocatalytic process. Under a 500 W Xe lamp irradiation, the γ -Bi₂MoO₆ obtained by using CTAB as surfactant can degrade MB 98% in 90 min.

Conflict of Interests

The authors declare that there is no conflict of interests regarding the publication of this paper.

References

- [1] A. Kubacka, M. Fernández-García, and G. Colón, "Advanced nanoarchitectures for solar photocatalytic applications," *Chemical Reviews*, vol. 112, no. 3, pp. 1555–1614, 2012.

- [2] Y. Huang, J. Wu, M. Huang, J. Lin, and Y. Huang, "Influence of surfactants on the morphology and photocatalytic activity of Bi_2WO_6 by hydrothermal synthesis," *Science China Chemistry*, vol. 54, no. 1, pp. 211–216, 2011.
- [3] W. Yin, W. Wang, and S. Sun, "Photocatalytic degradation of phenol over cage-like Bi_2MoO_6 hollow spheres under visible-light irradiation," *Catalysis Communications*, vol. 11, no. 7, pp. 647–650, 2010.
- [4] D. Saha, G. Madras, and T. N. Guru Row, "Solution combustion synthesis of $\gamma(\text{L})\text{-Bi}_2\text{MoO}_6$ and photocatalytic activity under solar radiation," *Materials Research Bulletin*, vol. 46, no. 8, pp. 1252–1256, 2011.
- [5] L. Zhou, W. Wang, and L. Zhang, "Ultrasonic-assisted synthesis of visible-light-induced Bi_2MO_6 ($\text{M} = \text{W}, \text{Mo}$) photocatalysts," *Journal of Molecular Catalysis A*, vol. 268, no. 1-2, pp. 195–200, 2007.
- [6] C. Belver, C. Adán, and M. Fernández-García, "Photocatalytic behaviour of Bi_2MO_6 polymetalates for rhodamine B degradation," *Catalysis Today*, vol. 143, no. 3-4, pp. 274–281, 2009.
- [7] A. Martínez-de la Cruz and S. Obregón Alfaro, "Synthesis and characterization of $\gamma\text{-Bi}_2\text{MoO}_6$ prepared by co-precipitation: photoassisted degradation of organic dyes under vis-irradiation," *Journal of Molecular Catalysis A*, vol. 320, no. 1-2, pp. 85–91, 2010.
- [8] L. Zhang, T. Xu, X. Zhao, and Y. Zhu, "Controllable synthesis of Bi_2MoO_6 and effect of morphology and variation in local structure on photocatalytic activities," *Applied Catalysis B*, vol. 98, no. 3-4, pp. 138–146, 2010.
- [9] H. Li, K. Li, and H. Wang, "Hydrothermal synthesis and photocatalytic properties of bismuth molybdate materials," *Materials Chemistry and Physics*, vol. 116, no. 1, pp. 134–142, 2009.
- [10] X. Lin, H. Li, L. Yu et al., "Efficient removal rhodamine B over hydrothermally synthesized fishbone like BiVO_4 ," *Materials Research Bulletin*, vol. 48, no. 10, pp. 4424–4429, 2013.
- [11] L. Zhang, H. Wang, Z. Chen, P. K. Wong, and J. Liu, " Bi_2WO_6 micro/nano-structures: synthesis, modifications and visible-light-driven photocatalytic applications," *Applied Catalysis B*, vol. 106, no. 1-2, pp. 1–13, 2011.
- [12] T. Yang, D. Xia, G. Chen, and Y. Chen, "Influence of the surfactant and temperature on the morphology and physico-chemical properties of hydrothermally synthesized composite oxide BiVO_4 ," *Materials Chemistry and Physics*, vol. 114, no. 1, pp. 69–72, 2009.
- [13] X. Zhao, T. Xu, W. Yao, and Y. Zhu, "Photodegradation of dye pollutants catalyzed by $\gamma\text{-Bi}_2\text{MoO}_6$ nanoplate under visible light irradiation," *Applied Surface Science*, vol. 255, no. 18, pp. 8036–8040, 2009.
- [14] L. Zhang, W. Wang, L. Zhou, and H. Xu, " Bi_2WO_6 nano- and microstructures: shape control and associated visible-light-driven photocatalytic activities," *Small*, vol. 3, no. 9, pp. 1618–1625, 2007.
- [15] C. Zhang and Y. Zhu, "Synthesis of square Bi_2WO_6 nanoplates as high-activity visible-light-driven photocatalysts," *Chemistry of Materials*, vol. 17, no. 13, pp. 3537–3545, 2005.

Research Article

Preparation and Magnetic Properties of Anisotropic (Sm,Pr)Co₅/Fe Nanocomposites Particles via Electroless Plating

Shi Wang, Jin-Ming Ma, and Yan Chen

Provincial Key Laboratory of Applied Chemistry, College of Environmental and Chemical Engineering, Yanshan University, Qinhuangdao 066004, China

Correspondence should be addressed to Yan Chen; chenyan@ysu.edu.cn

Received 8 November 2013; Revised 10 January 2014; Accepted 10 January 2014; Published 16 February 2014

Academic Editor: Lavinia Balan

Copyright © 2014 Shi Wang et al. This is an open access article distributed under the Creative Commons Attribution License, which permits unrestricted use, distribution, and reproduction in any medium, provided the original work is properly cited.

Anisotropic (Sm,Pr)Co₅/Fe nanocomposites particles were prepared by electroless plating iron on the surface of (Sm,Pr)Co₅ nanoflakes after being prepared by ball milling for 4 h. A uniform and continuous coating layer was obtained due to the addition of complexing agent and the particle size of the reduced Fe particles was in the range of 10~20 nm. When the nominal addition of Fe was 15 wt%, the nanocomposites show enhanced remnant and saturation magnetization: $M_r = 53.35$ emu/g, $M_s = 73.08$ emu/g compared to the noncoated nanoflakes with $M_r = 48.52$ emu/g, $M_s = 60.15$ emu/g, while the coercivity drops from 10.33 kOe to 8.89 kOe. The effect of Fe content on the magnetic properties of the magnets is also discussed.

1. Introduction

Nanocomposite magnetic materials have drawn extensive attention since they were reported by Coehoorn et al. [1] in 1988. The theoretical maximum magnetic energy product, (BH)_{max}, of anisotropy nanocomposite permanent magnets material can be as high as 1090 kJ/m³ (137 MGOe) [2], which is much higher than that of any single-phase permanent magnets. However, until now, (BH)_{max} of the nanocomposite magnets is still much lower than the theoretical value. An important factor restricting the development of the (BH)_{max} is the microstructure of theoretical models which is difficult to control. Generally speaking, an efficient exchange coupling needs to meet two conditions: (i) the size of the soft magnetic phase should be scaled to double domain wall width of the hard magnetic phase and (ii) soft magnetic phase should be uniformly distributed. So far, most of the nanocomposite magnets are fabricated following the conventional top-down routes, for example, high-energy mechanical milling, and melt spinning, but they are all isotropic materials with low (BH)_{max} [3–12]. The other “bottom-up” approach has actually attracted more attention, since it allows for the nanoparticles to be distributed uniformly and for the hard phase to be aligned and form an optimum structure so as to ensure efficient exchange coupling. A number of attempts have been

made to synthesize nanocomposite magnetic materials via the bottom-up way. Zeng et al. [13] used simple mechanical blending of Fe nanoparticles with Sm-Co permanent magnet powders, but the magnetic soft phase tended to agglomerate which led to the reduction in exchange coupling. Marinescu et al. [14] reported the use of a chemical deposition method to fabricate Sm-Co/nano-Fe composite, yielding relatively good magnetic properties. Zeng et al. [15] reported the fabrication of FePt-Fe₃Pt nanocomposites using nanoparticle self-assembly with (BH)_{max} of the nanocomposites exceeding the single phase by over 50 percent. However, although the particle size can be reduced to a certain degree, the agglomeration is inevitable.

In this paper, the electroless plating technique was applied to fabricate the (Sm,Pr)Co₅/Fe nanocomposites materials. The addition of complexing agent can control the deposition rate of the iron to form a continuous and uniform coating layer. The effect of the Fe content on magnetic properties was also investigated.

2. Experiment

The (Sm_{0.58}Pr_{0.42})Co₅ powders were milled mechanically for 4 h using a SPEX 8000 high-energy ball mill. The initial

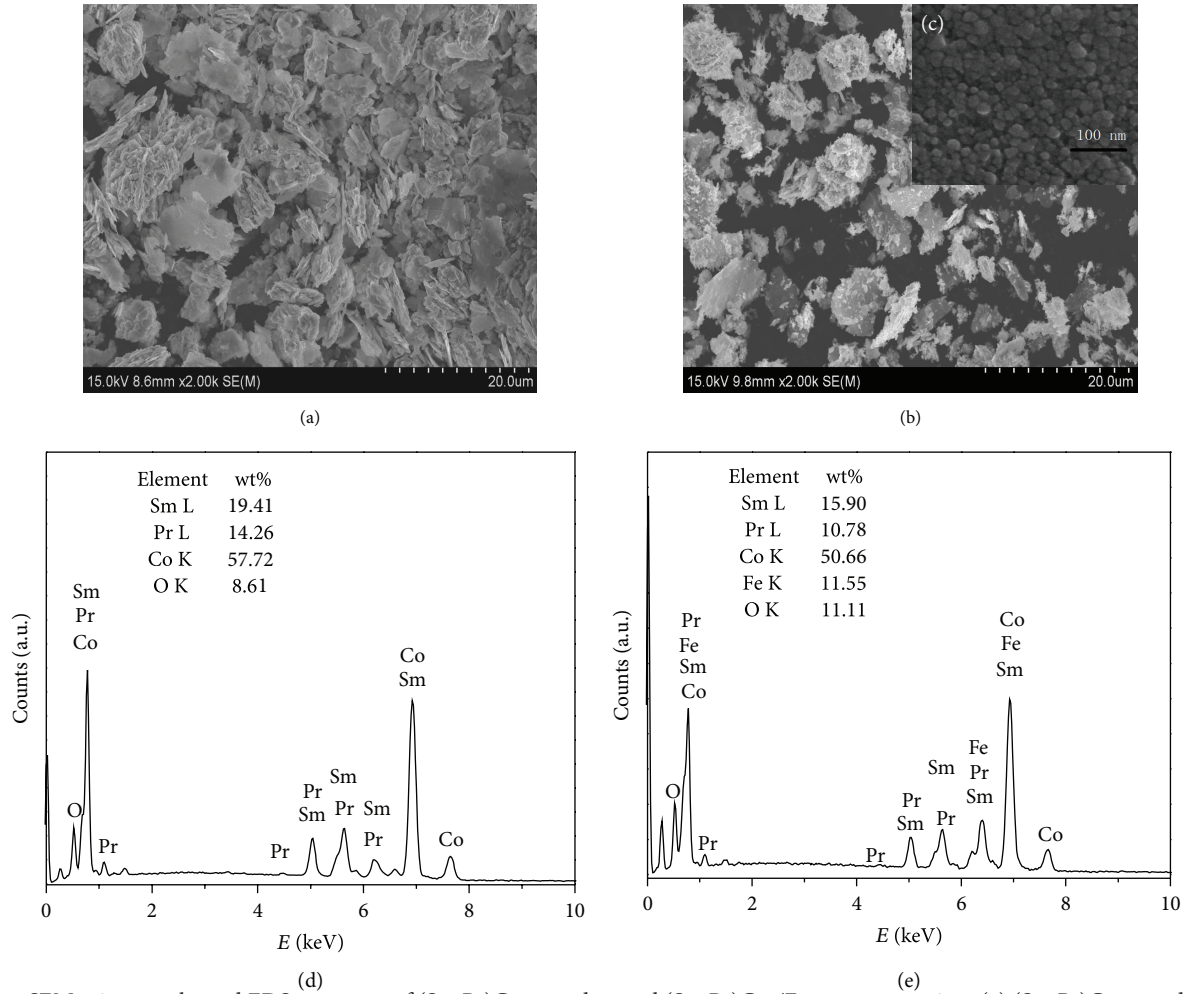
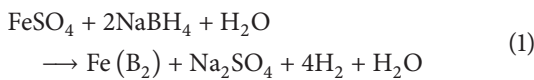


FIGURE 1: SEM micrographs and EDS spectrum of (Sm,Pr)Co₅ powders and (Sm,Pr)Co₅/Fe nanocomposites. (a) (Sm,Pr)Co₅ powders after ball milling for 4 h; ((b) and (c)) (Sm,Pr)Co₅/Fe nanocomposites for different magnifications; ((d) and (e)) EDS spectrum of (Sm,Pr)Co₅ and (Sm,Pr)Co₅/Fe nanocomposites and the element mass percentage.

adding amount of the (Sm_{0.58}Pr_{0.42})Co₅ powders was 2 g and the ball to powder ratio was 10:1 and the diameter of the steel ball is about 12 mm. During the process, heptane was used as the solvent with oleic acid used as the surfactant; the content in total mass was 10 wt.% and 55 wt.%, respectively. The synthesis of (Sm,Pr)Co₅/Fe nanoparticles was carried out under Argon atmosphere in a three-necked bottle. The following chemicals were used to synthesize the composite nanoparticle: (Sm,Pr)Co₅ (0.12 g), FeSO₄·7H₂O (0.1 g), C₆H₅Na₃O₇·2H₂O (0.6 g), and NaBH₄ (0.0625 g). In the first step, all the reagents except the reducing agent (NaBH₄) were dissolved in deionizer water and then diluted to 100 mL inside the container. Polyvinylpyrrolidone was added as surfactant to protect the particles from oxidation and avoid the soft magnetic phase aggregation [16]. In the end, NaBH₄ was dissolved in the deionizer water and then poured into the bottle slowly under the condition of continuous ultrason and mechanical stirring. The final chemical equation can be described as follows:



After reacting for 40 min, the powders were collected via magnetic separation and were washed by ethanol for several times. The composite powders were dried in a vacuum environment for further investigation.

The coating morphology and composition of the powders were characterized by scanning electron microscopy (SEM) equipped with an energy dispersion X-ray spectrometer (EDS). The crystal structure was determined by X-ray diffraction (XRD) using the Cu K α radiation, with the diffraction angular range from $2\theta = 25^\circ$ to 90° . The magnetic properties were investigated by a vibrating sample magnetometer (VSM). The powders were aligned under a 4 kOe field and solidified with epoxy resin for the VSM and XRD measurements.

3. Results and Discussion

SEM images of noncoated powders and coated nanocomposites are shown in Figure 1. The typical SEM image of (Sm,Pr)Co₅ powders is presented in Figure 1(a). It can be seen that after ball milling for 4 h, powders' agglomeration

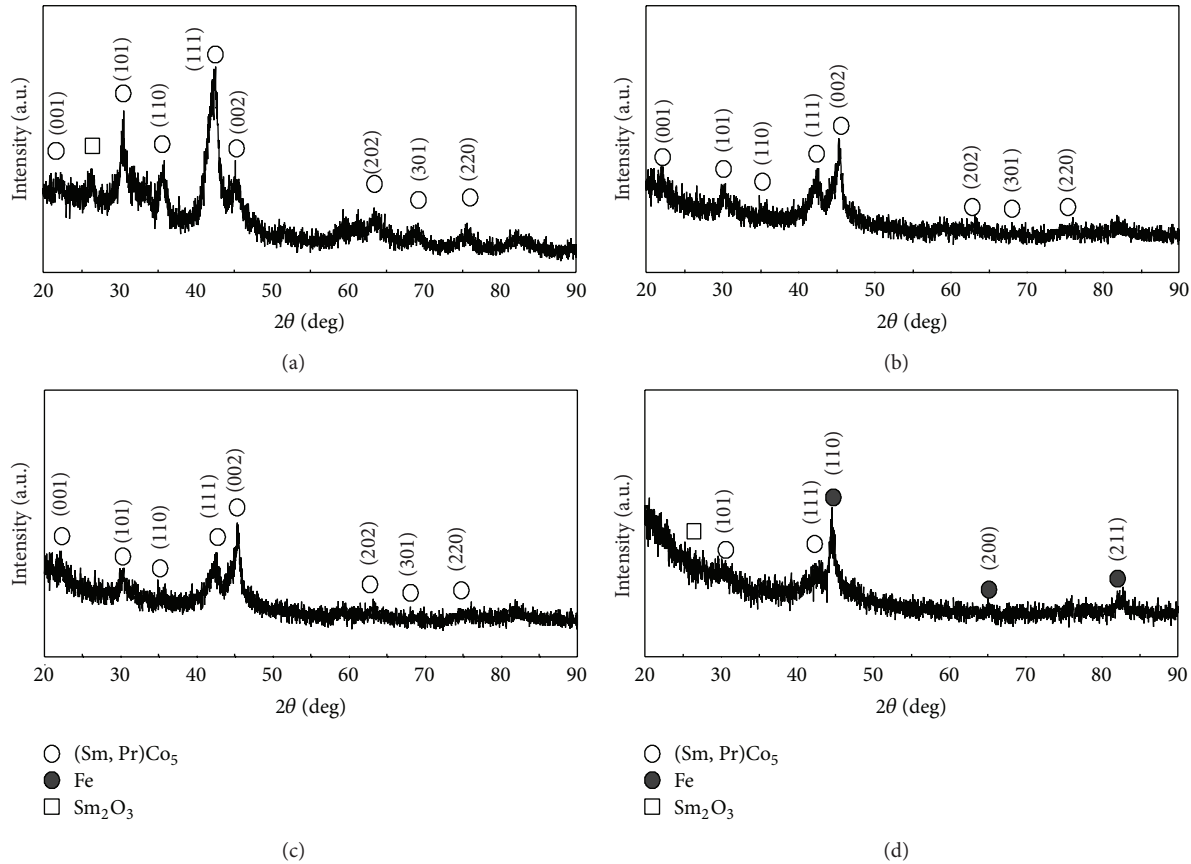


FIGURE 2: XRD patterns of (Sm,Pr)Co₅ nanoflakes: (a) nonaligned; (b) magnetically aligned; (c) (Sm,Pr)Co₅/Fe nanocomposites magnetically aligned; (d) (Sm,Pr)Co₅/Fe nanocomposites annealed at 450°C.

is still obvious and the particles have a flaky-like structure. The thickness of the nanoflakes is about 50~100 nm, with the length range from 0.5 to 8 μm . The nanoflakes provide a large specific surface area for further coating. Figures 1(b) and 1(c) show the SEM micrographs of the (Sm,Pr)Co₅/Fe nanocomposites at different magnifications. From Figure 1(b), the flakes are coated with a large amount of nanoparticles, but a few of the nanoparticles are also aggregated separately. The inset Figure 1(c) shows the much greater magnification of nanocomposites; a layer of continuous nanoparticles is coated on the surface and the particles' size is about 10~20 nm. The iron layer distributes uniformly and not simply stacks together. The elemental composition and mass fraction of the nanocomposites are revealed by the energy dispersive X-ray spectroscopy. Figures 1(d) and 1(e) show the energy spectrum of (Sm,Pr)Co₅ and (Sm,Pr)Co₅/Fe, respectively. The mass fraction of iron is 11.5%, which indicates that the nanocomposites have a relatively high content of soft phase. However, the iron coating content relative to the composite powder stoichiometry was 15% in mass. The content is still lower than the nominal content we initially added, which implies that the iron particles are not fully deposited on the surface of (Sm,Pr)Co₅ and fewer iron particles nucleate and grow directly in the solution. It is worth mentioning that the oxidation is inevitable during the process of ball milling

and electroless plating, which would lead to a decrease in magnetic properties.

Figures 2(a) and 2(b) show the XRD patterns of the sample of (Sm,Pr)Co₅ nanoflakes nonaligned and aligned, respectively. The diffraction peaks can be indexed as the standard SmCo₅ (JCPDS NO.35-1400). After magnetic alignment, the (002) peak becomes dominant, indicating a strong *c*-axis crystallographic alignment [16]. The results are consistent with the report of Cui et al. [17, 18]. But there are no obvious diffraction peaks of iron in the XRD pattern of (Sm,Pr)Co₅/Fe nanoflakes (Figure 2(c)). The possible reason was that the iron grain was too small or partly crystallized, so the intensity of the iron diffraction peak was weak and partly covered by the (Sm,Pr)Co₅ peaks. Therefore, (Sm,Pr)Co₅/Fe nanocomposites were annealed by vacuum at 450°C for 10 minutes. Figure 2(d) shows the XRD pattern of (Sm,Pr)Co₅/Fe nanocomposites after annealing treatment. The iron diffraction peaks could be indexed (JCPDS NO.06-0696), which proved the existence of iron. Oxidation of (Sm,Pr)Co₅ occurred during the annealing process due to the remaining surfactant being removed incompletely. Moreover, the main diffraction peaks of Fe-B compounds cannot be indexed which proves the nonexistence of the Fe-B compounds and the particle layer is Fe nanoparticle coated on the (Sm,Pr)Co₅ surface.

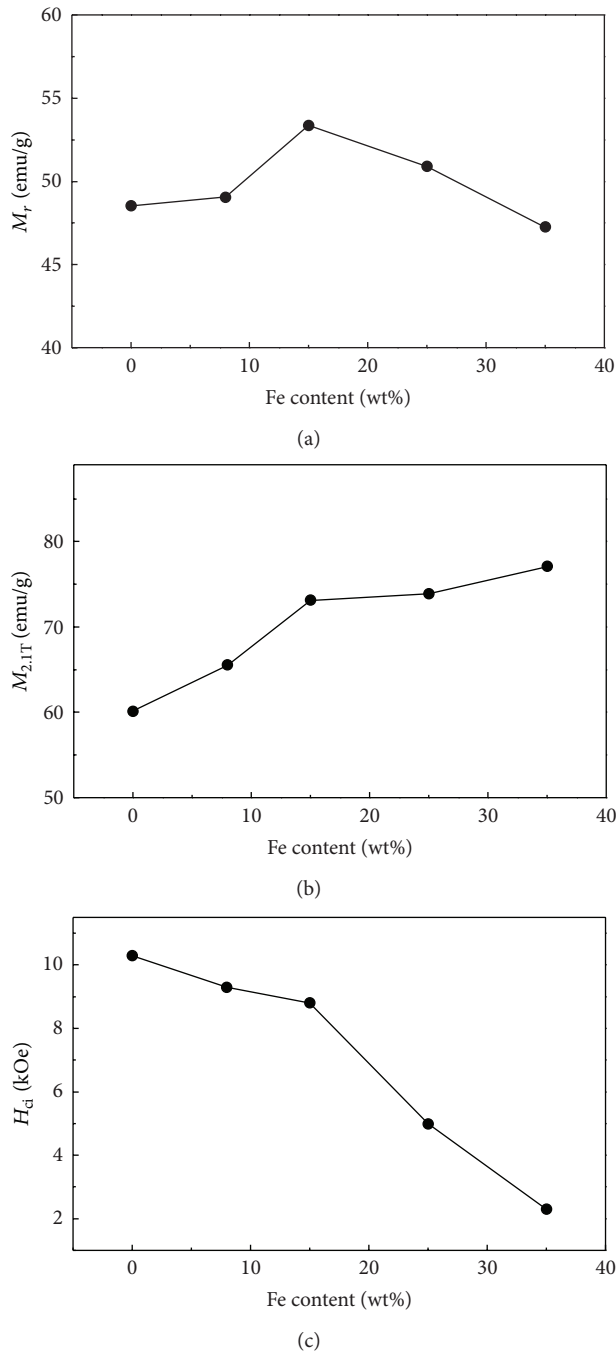


FIGURE 3: Magnetic properties of $(\text{Sm},\text{Pr})\text{Co}_5/\text{Fe}$ nanocomposites with different Fe contents.

The magnetic properties of composite $(\text{Sm},\text{Pr})\text{Co}_5/\text{Fe}$ nanoflakes with different iron contents are shown in Figure 3. The nanocomposites were measured in the direction parallel to the c -axis. It can be seen that the remnant magnetization shows a trend of first increasing then decreasing with the content of iron increases and reaches the maximum value when the iron content is 15% in weight. Although the saturation magnetization increases gradually with the increase of iron content as we expect, the coercivity drops

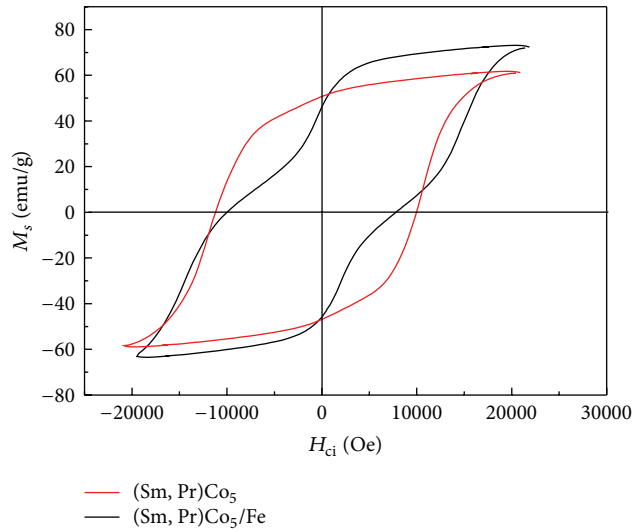


FIGURE 4: Magnetic hysteresis loops of aligned $(\text{Sm},\text{Pr})\text{Co}_5$ nanoflakes and $(\text{Sm},\text{Pr})\text{Co}_5/\text{Fe}$ nanocomposites.

dramatically. Figure 4 shows the magnetic hysteresis loops of the $(\text{Sm},\text{Pr})\text{Co}_5$ nanoflakes and the $(\text{Sm},\text{Pr})\text{Co}_5/\text{Fe}$ nanocomposites with 15 wt.% Fe content. The magnetic properties of $(\text{Sm},\text{Pr})\text{Co}_5/\text{Fe}$ nanocomposites nonannealing are shown below: $M_r = 53.35$ emu/g, $M_s = 73.08$ emu/g, and $H_{ci} = 8.89$ kOe; the magnetic properties of $(\text{Sm},\text{Pr})\text{Co}_5$ nanoflakes are presented as a reference: $M_r = 48.52$ emu/g, $M_s = 60.15$ emu/g, and $H_{ci} = 10.33$ kOe. However, the magnetic hysteresis loop of $(\text{Sm},\text{Pr})\text{Co}_5/\text{Fe}$ is not smooth and there is an obvious collapse in the second quadrant, which indicates that the exchange coupling effect between the magnetically soft and hard phase is not strong. The possible reasons for this may be that the particle size and the distribution of the soft phase are not precise enough to achieve the requirements of the theory.

4. Conclusion

In summary, we prepared $(\text{Sm},\text{Pr})\text{Co}_5/\text{Fe}$ nanocomposites via electroless plating. The addition of a complexing agent effectively controls the coating morphology, to obtain a continuous and uniform Fe layer. The nanocomposites show enhanced magnetic properties when the nominal addition of Fe was 15 wt.%, $M_r = 53.35$ emu/g, $M_s = 73.08$ emu/g, and $H_{ci} = 8.89$ kOe compared to the properties of uncoated nanoflakes $M_r = 48.52$ emu/g, $M_s = 60.15$ emu/g, and $H_{ci} = 10.33$ kOe. The coercivity drops dramatically with the increase of Fe content, and also the magnetic hysteresis loop of the nanocomposite shows an obvious collapse in the second quadrant.

Conflict of Interests

The authors declare that there is no conflict of interests regarding the publication of this paper.

References

- [1] R. Coehoorn, D. B. de Mooij, J. P. W. B. Duchateau, and K. H. J. Buschow, "Novel permanent magnetic materials made by rapid quenching," *Journal of Applied Physics*, vol. 49, no. 8, pp. 669–670, 1988.
- [2] R. Skomski, "Aligned two-phase magnets: permanent magnetism of the future? (Invited)," *Journal of Applied Physics*, vol. 76, no. 10, pp. 7059–7064, 1994.
- [3] R. Fischer, T. Schrefl, H. Kronmüller, and J. Fidler, "Phase distribution and computed magnetic properties of high-remanent composite magnets," *Journal of Magnetism and Magnetic Materials*, vol. 150, no. 3, pp. 329–344, 1995.
- [4] D. Goll, M. Seeger, and H. Kronmüller, "Magnetic and micro structural properties of nanocrystalline exchange coupled PrFeB permanent magnets," *Journal of Magnetism and Magnetic Materials*, vol. 185, no. 1, pp. 49–60, 1998.
- [5] P. G. McCormick, W. F. Miao, P. A. I. Smith, J. Ding, and R. Street, "Mechanically alloyed nanocomposite magnets (invited)," *Journal of Applied Physics*, vol. 83, no. 11, pp. 6256–6261, 1998.
- [6] S.-Y. Chu, S. A. Majetich, M.-Q. Huang, and R. T. Fingers, "Synthesis and magnetic behavior of $\text{SmCo}_{5(1-x)}\text{Fe}_x$ nanocomposite magnets," *Journal of Applied Physics*, vol. 93, no. 10, pp. 8146–8148, 2003.
- [7] W. Li, L. Li, Y. Nan et al., "Controllable nanocrystallization in amorphous $\text{Nd}_9\text{Fe}_{85}\text{B}_6$ via combined application of severe plastic deformation and thermal annealing," *Applied Physics Letters*, vol. 91, no. 6, Article ID 062509, 2007.
- [8] Q. Nguyen, C. N. Chinnasamy, S. D. Yoon et al., "Functionalization of FeCo alloy nanoparticles with highly dielectric amorphous oxide coatings," *Journal of Applied Physics*, vol. 103, no. 7, Article ID 07D532, 2008.
- [9] P. Saravanan, M. Premkumar, A. K. Singh, R. Gopalan, and V. Chandrasekaran, "Study on morphology and magnetic behavior of SmCo_5 and SmCo_5/Fe nanoparticles synthesized by surfactant-assisted ball milling," *Journal of Alloys and Compounds*, vol. 480, no. 2, pp. 645–649, 2009.
- [10] C.-B. Rong, Y. Zhang, N. Poudyal, X.-Y. Xiong, M. J. Kramer, and J. P. Liu, "Fabrication of bulk nanocomposite magnets via severe plastic deformation and warm compaction," *Applied Physics Letters*, vol. 96, no. 10, Article ID 102513, 2010.
- [11] C.-B. Rong, Y. Zhang, N. Poudyal et al., "Self-nanoscaling of the soft magnetic phase in bulk SmCo/Fe nanocomposite magnets," *Journal of Materials Science*, vol. 46, no. 18, pp. 6065–6074, 2011.
- [12] S. C. Sun, Z. Q. Qi, H. Q. Chen et al., "Effects of $\text{Al}_{0.3}\text{Ga}_{0.7}\text{As}$ interlayer with pulsed atomic layer epitaxy on heterogeneous integration of GaAs/Ge grown by MOCVD," *Journal of Alloys and Compounds*, vol. 590, pp. 1–4, 2014.
- [13] Q. Zeng, Y. Zhang, M. J. Bonder, G. C. Hadjipanayis, and R. Radhakrishnan, "Bulk $\text{SmCo}_5/\alpha\text{-Fe}$ composite by plasma pressure consolidation," *IEEE Transactions on Magnetics*, vol. 39, no. 5, pp. 2974–2976, 2003.
- [14] M. Marinescu, J. F. Liu, M. J. Bonder, and G. C. Hadjipanayis, "Fe-nanoparticle coated anisotropic magnet powders for composite permanent magnets with enhanced properties," *Journal of Applied Physics*, vol. 103, no. 7, Article ID 07E120, 2008.
- [15] H. Zeng, J. Li, J. P. Liu, Z. L. Wang, and S.-H. Sun, "Exchange-coupled nanocomposite magnets by nanoparticle self-assembly," *Nature*, vol. 420, no. 6914, pp. 395–398, 2002.
- [16] X.-L. Wang, H.-L. He, F.-Q. Wang et al., "Preparation and magnetic properties of anisotropic $(\text{Sm},\text{Pr})\text{Co}_5/\text{Co}$ composite particles," *Journal of Magnetism and Magnetic Materials*, vol. 324, no. 5, pp. 889–892, 2012.
- [17] B. Z. Cui, A. M. Gabay, W. F. Li, M. Marinescu, J. F. Liu, and G. C. Hadjipanayis, "Anisotropic SmCo_5 nanoflakes by surfactant-assisted high energy ball milling," *Journal of Applied Physics*, vol. 107, no. 9, Article ID 09A721, 2010.
- [18] B. Z. Cui, W. F. Li, and G. C. Hadjipanayis, "Formation of SmCo_5 single-crystal submicron flakes and textured polycrystalline nanoflakes," *Acta Materialia*, vol. 59, no. 2, pp. 563–571, 2011.

Research Article

Preparation and Its Adsorptive Property of Modified Expanded Graphite Nanomaterials

Liqin Wang,^{1,2} Xiujun Fu,¹ E. Chang,¹ Haitao Wu,¹ Kun Zhang,¹ Xianchao Lei,¹ Ruijun Zhang,² Xiaowen Qi,³ and Yulin Yang³

¹ Hebei Key Laboratory of Applied Chemistry, College of Environmental and Chemical Engineering, Yanshan University, Qinhuangdao 066004, China

² State Key Laboratory of Metastable Materials Science and Technology, Yanshan University, Qinhuangdao 066004, China

³ College of Mechanical Engineering, Yanshan University, Qinhuangdao, Hebei 066004, China

Correspondence should be addressed to Liqin Wang; wangliqin@ysu.edu.cn

Received 6 November 2013; Revised 8 January 2014; Accepted 9 January 2014; Published 12 February 2014

Academic Editor: Lavinia Balan

Copyright © 2014 Liqin Wang et al. This is an open access article distributed under the Creative Commons Attribution License, which permits unrestricted use, distribution, and reproduction in any medium, provided the original work is properly cited.

Modified expanded graphite (MEG) samples were prepared by strong acid treatment modification. As-prepared MEG samples were characterized by the means of FE-SEM, XRD, FT-IR, N₂ physical adsorption measurements, and TG-DTA. The influences of expanded volume and oil viscosity on adsorptive property of MEG samples were investigated. The results suggest that MEG samples have high crystallinity. The pores of MEG samples can be divided into three levels from FE-SEM images. All of the functional groups of MEG samples are nonpolar. The expansion temperature of modified expandible graphite starts at about 700°C. The sorption capacity of MEG increases gradually with expanded volume and oil viscosity increase. When the expanded volume of MEG samples is 320 mL/g, its maximum sorption capacity is up to 84.681 g/g for gear oil with the highest viscosity.

1. Introduction

In recent years, the spill oils pollutions have caused extensive and widespread concerns. Spill oils not only severely pollute the marine environment but also threaten the human lives. The expanded graphite (EG) with a majority of macropores [1–3] and nonpolar surface make it as an excellent material for absorbing nonpolar and macromolecular compounds, especially for various kinds of oils. EG has been usually prepared through the sequential intercalating, washing, drying, and puffing from the natural flake graphite [4, 5]. Many scholars have paid more attention to research the relationships between the preparation conditions, pore structure, and its sorption capacities [6–8]. Furthermore, EG has also been widely applied in waste gas removal [9], catalysts carrier [10–12], medical materials [13], and many other fields [14–16]. However, EG has some disadvantages such as fragile, light mass and low expanded ratio by one step processing, so that a lot of studies have been focused on its modification researches [17–25]. The modification methods for EG mainly include strong acid treatment modification, in-situ modification,

surfactant modification, and surface coating modification [26, 27].

In this paper, H₂O₂ was used as the oxidant, concentrated H₂SO₄ was used as the intercalator, and the MEG samples were prepared by strong acid treatment modification. The MEG samples were characterized by FE-SEM, XRD, FT-IR, N₂ physical adsorption measurements, and TG-DTA. Six kinds of industrial oils such as gasoline, kerosene, diesel oil, machine oil, crude oil, and gear oil were used as sorbents to investigate the sorption capacity of MEG samples.

2. Experimental

2.1. Materials. 3599-flake graphite, concentrated H₂SO₄ (98 wt.%), H₂O₂ solution (30 wt.%), distilled water, gasoline, kerosene, diesel oil, machine oil, crude oil, and gear oil were used.

2.2. Preparation. Weighed 2 g of expandible graphite was put into a beaker, and then it was mixed with concentrated H₂SO₄

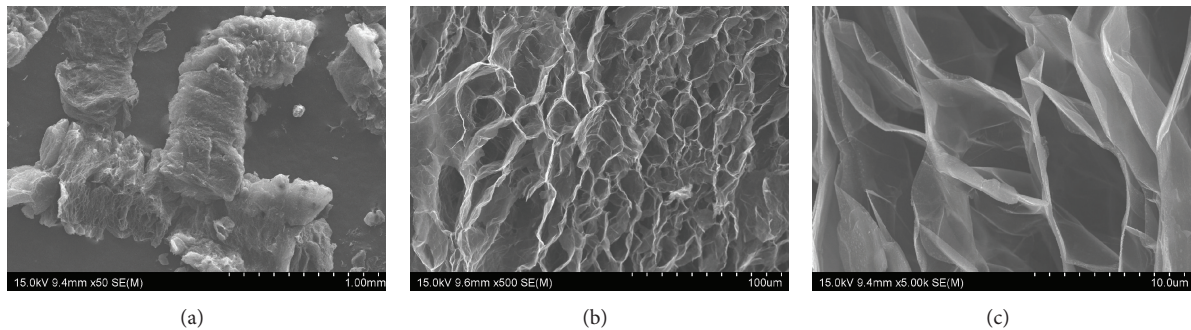


FIGURE 1: FE-SEM images of the MEG samples.

and H_2O_2 solution (volume ratio 10 : 1.5) and was stirred with them until it formed an even mixture. Then, the beaker was put in the water bath at 45°C, and the mixture was stirred vigorously for 90 min. After the mixture was washed and dried, the expansible graphite was obtained. Weighed 2 g of expansible was put graphite into a beaker, and then the expansible graphite was mixed with concentrated H_2SO_4 and H_2O_2 solution (volume ratio 10 : 1.25) again, and the obtained mixture was also stirred vigorously at 45°C for 90 min. After the mixture was washed and dried and calcined at 900°C for 15 s in a muffle furnace, the preparation of MEG samples was accomplished.

2.3. Characterization. The morphology of MEG samples was studied by the field emission scanning electron microscopy (FE-SEM) of S4800. The crystal structure of the samples was determined by the X-ray powder diffractometer (XRD) of D/MAX-rB, which was radiated by $\text{Cu K}\alpha$ with the pipe pressure of 40 mV, the wavelength (λ) is 1.54056 Å, and the diffraction angle is in the range of 10°–80°. The chemical functional groups in the samples were analyzed by the Fourier transformation-infrared spectroscope (FT-IR, EQUINOX55). The N_2 adsorption-desorption isotherms and pore size distribution plots were measured by NOVA4000e automatic physical adsorption apparatus, and the measurement was performed at 77 K, the outgas temperature was 250°C, and the BJH modeling was used for the pore size determination. Moreover, the thermogravimetric analysis and differential thermal analysis (TG-DTA) curves of the samples were carried out by CRY-2P and WRT-3P analyzer. The atmosphere set during the analysis was argon, and the heating rate was 10°C/min.

2.4. Adsorptive Property. A certain amount of seawater and some kind of industrial oils were added into the 200 mL beaker to simulate the spill oil on the sea. m g of MEG samples was immersed into the liquid mixture, and then MEG samples that absorbed oil and seawater mixture was put on the funnel covered with filter screen (mass m_0 , g) until the MEG samples have reached the saturation adsorption amount and weighed MEG samples with filter screen (mass m_1 , g) at that time. The sorption capacity (mass m_2 , g/g) of the MEG samples can be calculated by the following formula:

$$m_2 = \frac{m_1 - m_0 - m}{m} \quad (1)$$

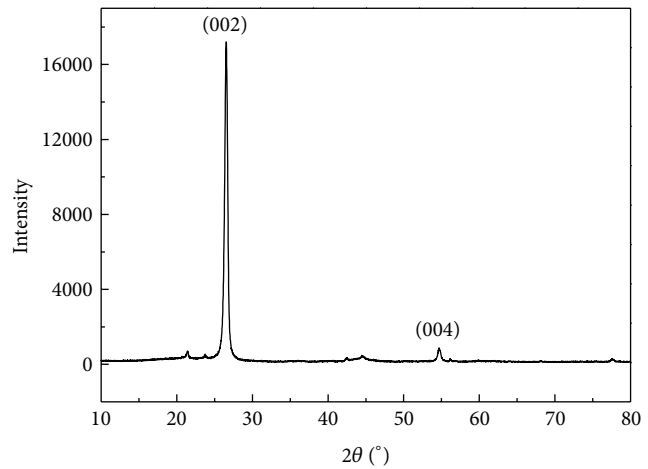


FIGURE 2: XRD pattern of the MEG samples.

3. Results and Discussion

3.1. FE-SEM Analysis. Figure 1 shows FE-SEM images of the MEG samples. The morphology of the MEG samples is worm-like as shown in Figure 1(a), and there are a lot of V-type pores that can also be observed on the surface. These V-type pores with dimension from several dozens of μm to several hundreds of μm are the I level pores, the willow leaf-type pores with dimension from several μm to several dozens of μm as shown in Figure 1(b) are ascribed to the II level pores. The pores with dimension from 0.1 μm to several μm as seen from Figure 1(c) come from the up and down on the pore walls of the II level pores and are assigned to the III level pores in the MEG samples. It is the particular loose and porous structures that would provide MEG samples with good adsorption property for the macromolecular compounds.

3.2. XRD Pattern. XRD pattern of the MEG is shown in Figure 2. There are two obvious characteristic diffraction peaks located at 2θ equal to 26.4° and 54.9°, which corresponded to the (002) and (004) crystal planes, respectively. Crystal phase composition of MEG samples is identified as graphite-2H phase according to the standard card of PDF number 41-1487. Thus, it can be inferred that the MEG samples still maintain the crystal structure of natural graphite itself [28], and it also belongs to the graphite crystal.

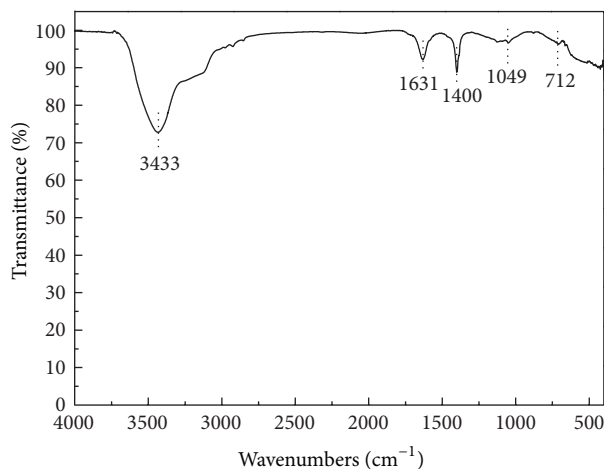


FIGURE 3: FT-IR spectra of the MEG samples.

3.3. FT-IR Spectra. Figure 3 displays FT-IR spectra of the MEG. The peaks at 3433 cm^{-1} and 1631 cm^{-1} are described as stretching vibration absorption peak and deformation vibration absorption peak from water molecules, respectively. They may be derived of adsorbed water from MEG samples and potassium bromide crystal used for pressing pieces and the surface hydroxyl group. The strong peak at 1400 cm^{-1} is considered the absorption of the methylene fat hydrocarbon from graphitic carbon skeleton. A weak absorption peak at 1049 cm^{-1} belongs to stretching vibration of C–O–C. The weaker peak at 712 cm^{-1} corresponds to the absorption of SO_4^{2-} , and this may be related to inadequate expansion of modified expandable graphite under heat treatment. The results indicate that a large number of intercalator groups basically disappear after high temperature expansion, and MEG samples can be assigned to nonpolar materials.

3.4. N_2 Physical Adsorption Analysis. N_2 adsorption-desorption isotherms and pore size distribution plots of the MEG are illustrated in Figure 4. The adsorption-desorption isotherms correspond to the typical type II isotherms (IUPAC, 1985), suggesting the existence of macropores and showing an unobvious hysteresis between adsorption and desorption isotherms.

As shown in Figure 4, there is a small fraction of mesopores in the MEG samples, and the pore diameter is from 2 nm to 7 nm. These pores with nanometer scale within 100 nm are attributed to the III level pores of the MEG. Combining with FE-SEM analysis results, the present work divides the pores of MEG into three levels, and it is in agreement with reports [29–31] in the literature. In addition, according to the N_2 physical adsorption analysis results, the BET specific surface area of the MEG samples is $26\text{ m}^2/\text{g}$, and the pore volume of the MEG samples is $0.069\text{ cm}^3/\text{g}$ by the BJH modeling.

3.5. TG-DTA Analysis. Figure 5 describes TG-DTA curves of modified expandable graphite. As shown in Figure 5, there is an endothermic peak at 60°C , and the corresponding mass loss appears in the TG curve, which inferred that some amo-

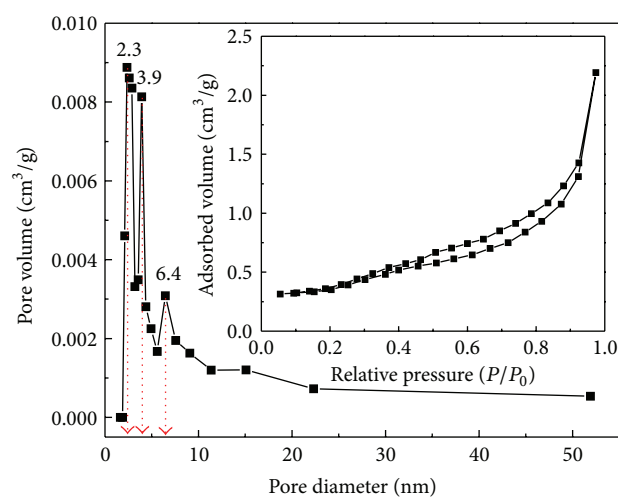
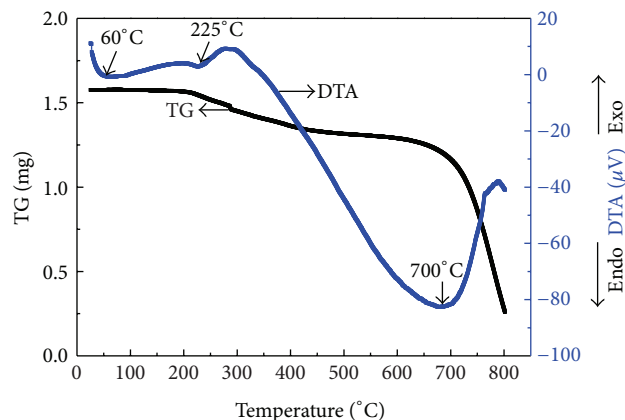
FIGURE 4: N_2 adsorption-desorption isotherms and pore size distribution plots of the MEG samples.

FIGURE 5: TG-DTA curves of MEG precursors.

unt of absorbed water in the samples has been evaporated. Another endothermic peak appears at 225°C in the DTA curve, which is attributed to the dehydration of bound water. There is a broad and strong endothermic peak at 700°C in the DTA curve, and there is obvious mass loss in the TG curve accordingly. This could be ascribed to the decomposition of H_2SO_4 -GICs (graphite intercalation compounds) and the burn of graphite, so some S–O and CO_x species diffuse out of graphite gallery. The results show that the onset expansion temperature of modified expandable graphite should be scheduled at 700°C by using muffle furnace.

3.6. Adsorptive Property

3.6.1. Influence of Expanded Volume on Adsorptive Property of the MEG. The maximum sorption capacity of MEG with different expanded volume for kerosene, crude oil, and gear oil is shown in Figure 6. For the same kind of oil, the maximum sorption capacity of MEG increases gradually with the increase of the expanded volume. When the expanded volume of MEG varies between 100 mL/g , 150 mL/g , 190 mL/g , 250 mL/g , and 320 mL/g , the maximum sorption capacities

TABLE 1: The effect of oil viscosity on sorption capacity of the MEG.

Kinds	Gasoline	Kerosene	Diesel oil	Machine oil	Crude oil	Gear oil
Viscosity (Pa·s)	0.001	0.002	0.008	0.156	0.626	1.407
Oil absorption (g/g)	43.25	47.657	50.879	55.128	65.537	84.681

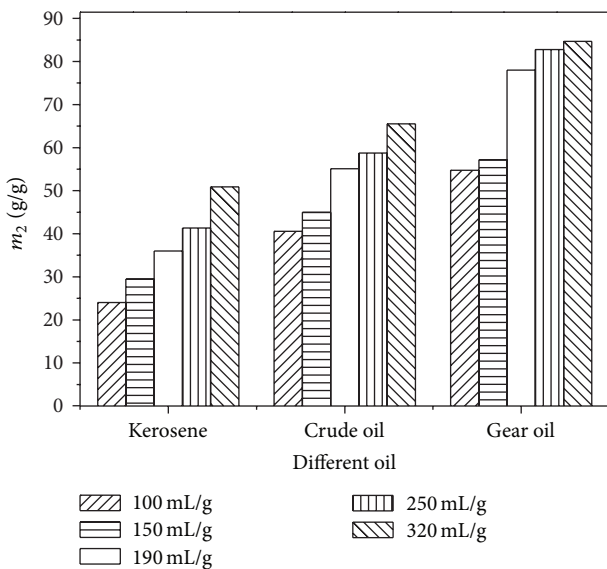


FIGURE 6: The effect of expanded volume on sorption capacity of the MEG samples.

for gear oil are 54.741 g/g, 57.192 g/g, 78.004 g/g, 82.802 g/g, and 84.681 g/g, respectively. Moreover, for the same expanded volume, the maximum sorption capacities arrange in the order of gear oil > crude oil > kerosene. When the expanded volume of MEG is 320 mL/g, the maximum sorption capacities of MEG samples are 50.879 g/g, 65.537 g/g, and 84.681 g/g for kerosene, crude oil and gear oil, respectively. The reasons are as follows: the I level V-type pores make the main contributions to the formation of MEG intertwining space, and the II level willow leaf-type pores constitute a unique internal storage space. So the synergy between the I level pores and the II level pores provides MEG samples with outstanding adsorptivity for several industrial oils [32]. Moreover, the number of the I and II level pores increases with expanded volume increase. So that with the expanded volume increasing, the sorption capacity of MEG samples for oils also increases obviously. The maximum sorption capacity of MEG samples for gear oil is up to 84.681 g/g.

3.6.2. Influence of Oil Viscosity on Adsorptive Property of the MEG. The effect of oil viscosity on sorption capacity of the MEG is listed in Table 1. The results show that the oil viscosity has a great influence on the sorption capacity of MEG, and the maximum sorption capacity of MEG increases gradually with the increase of the oil viscosity for the same expanded volume. For the low viscosity oil, such as gasoline, kerosene and diesel oil, the maximum sorption capacities of MEG are 43.25 g/g, 47.657 g/g and 50.879 g/g, respectively. For the high viscosity machine oil and crude oil, the maximum sorption capacities

of MEG are 55.128 g/g and 65.537 g/g, respectively. And for the highest viscosity gear oil, the maximum sorption capacity of MEG can be up to 84.681 g/g. The main reason probably is that the higher viscosity oil has the higher glutinosity and density, and lower liquidity. In other words, high viscosity will be beneficial to the adhesion of MEG and oils.

4. Conclusions

To expand and develop the expanded volume of EG and MEG samples were prepared by the strong acid treatment modification. According to above characterization and experiment results, the MEG samples have high graphite crystallinity. The pores of MEG samples can be divided into three levels by FE-SEM. All of the functional groups of MEG samples are nonpolar. The expansion temperature of modified expansible graphite starts at about 700°C. The sorption capacity of MEG increases gradually with the expanded volume and oil viscosity increase. When expanded volume of MEG samples is 320 mL/g, the maximum sorption capacity is up to 84.681 g/g for gear oil with the highest viscosity. It is the property of multipores and worm-like structures that provide the MEG with high sorption capacity, and it will be a kind of promising adsorptive material in the future.

Conflict of Interests

The authors declare that there is no conflict of interests regarding the publication of this paper.

Acknowledgments

This work was financially supported by the Science & Technology Pillar Program of Hebei Province (no. 12276716D) and the Science & Technology Research Program of Hebei Province (no. ZD20131010).

References

- [1] C.-Y. Guo and C.-Y. Wang, "Study on preparation of activated mesocarbon microbeads/expanded graphite composites for electrical double layer capacitors," *Composites Science and Technology*, vol. 67, no. 7-8, pp. 1747–1750, 2007.
- [2] A. B. Nair, P. Kurian, and R. Joseph, "Effect of expanded graphite on thermal, mechanical and dielectric properties of ethylene-propylene-diene terpolymer/hexa fluoropropylene-vinylidenefluoride dipolymer rubber blends," *European Polymer Journal*, vol. 49, pp. 247–260, 2013.
- [3] X.-J. Yu, J. Wu, Q. Zhao, and X.-W. Cheng, "Preparation and characterization of sulfur-free exfoliated graphite with large exfoliated volume," *Materials Letters*, vol. 73, pp. 11–13, 2012.

- [4] Z. Ying, X. Lin, Y. Qi, and J. Luo, "Preparation and characterization of low-temperature expandable graphite," *Materials Research Bulletin*, vol. 43, no. 10, pp. 2677–2686, 2008.
- [5] S. T. Kim, J. Ryu, and Y. Kato, "Optimization of magnesium hydroxide composite material mixed with expanded graphite and calcium chloride for chemical heat pumps," *Applied Thermal Engineering*, vol. 50, pp. 485–490, 2013.
- [6] B. Mortazavi, F. Hassouna, A. Laachachi et al., "Experimental and multiscale modeling of thermal conductivity and elastic properties of PLA/expanded graphite polymer nanocomposites," *Thermochimica Acta*, vol. 552, pp. 106–113, 2013.
- [7] X. Yue, H. Wang, S. Wang, F. Zhang, and R. Zhang, "In-plane defects produced by ball-milling of expanded graphite," *Journal of Alloys and Compounds*, vol. 505, no. 1, pp. 286–290, 2010.
- [8] F. Y. Kang, Y. P. Zheng, H. Zhao et al., "Sorption of heavy oils and biomedical liquids into exfoliated graphite—Research in China," *New Carbon Materials*, vol. 18, no. 3, pp. 161–1173, 2003.
- [9] N. Z. Cao, W. C. Shen, S. Z. Wen, and Y. J. Liu, "Application of expanded graphite adsorption material to environmental protection," *Environmental Engineering*, vol. 14, no. 3, pp. 27–29, 1996.
- [10] S. F. Zhao, X. Y. Pang, R. F. Li, H. X. Li, and T. Gao, "Study on the catalysis of expandable in transesterification reaction of animal oil," *Carbon*, vol. 4, pp. 19–22, 2007.
- [11] W. Li, C. Han, W. Liu, M. Zhang, and K. Tao, "Expanded graphite applied in the catalytic process as a catalyst support," *Catalysis Today*, vol. 125, no. 3-4, pp. 278–281, 2007.
- [12] I. M. Afanasov, O. I. Lebedev, B. A. Kolozhvary, A. V. Smirnov, and G. van Tendeloo, "Nickel/Carbon composite materials based on expanded graphite," *New Carbon Materials*, vol. 26, no. 5, pp. 335–340, 2011.
- [13] W. Shen, S. Wen, N. Cao et al., "Expanded graphite—a new kind of biomedical material," *Carbon*, vol. 37, no. 2, pp. 356–358, 1999.
- [14] Y. L. Zhong and T. M. Swager, "Enhanced electrochemical expansion of graphite for in situ electrochemical functionalization," *Journal of the American Chemical Society*, vol. 134, pp. 17896–17899, 2012.
- [15] L. Yu, Y. H. Zhang, W. S. Tong et al., "Hierarchical composites of conductivity controllable polyaniline layers on the exfoliated graphite for dielectric application," *Composites A*, vol. 43, pp. 2039–2045, 2012.
- [16] G. Katsukis, J. Malig, C. Schulz-Drost, S. Leubner, N. Jux, and D. M. Guldi, "Toward combining graphene and QDs: assembling CdTe QDs to exfoliated graphite and nanographene in water," *ACS Nano*, vol. 6, no. 3, pp. 1915–1924, 2012.
- [17] G. Wang, Q. Sun, Y. Zhang, J. Fan, and L. Ma, "Sorption and regeneration of magnetic exfoliated graphite as a new sorbent for oil pollution," *Desalination*, vol. 263, no. 1–3, pp. 183–188, 2010.
- [18] X. Q. Yue, R. J. Zhang, F. C. Zhang, and L. Q. Wang, "Decomposition of crude oil absorbed into expanded graphite/TiO₂/NiO composites," *Desalination*, vol. 252, no. 1–3, pp. 163–166, 2010.
- [19] L. Q. Wang, X. N. Yang, X. L. Zhao, R. J. Zhang, and Y. L. Yang, "Preparation and characterization of expanded graphite with ZnO composites," *Advanced Materials Research*, vol. 197–198, pp. 770–773, 2011.
- [20] A. Goshadrou and A. Moheb, "Continuous fixed bed adsorption of C.I. Acid Blue 92 by exfoliated graphite: an experimental and modeling study," *Desalination*, vol. 269, no. 1–3, pp. 170–176, 2011.
- [21] P. Krawczyk, "Effect of ozone treatment on properties of expanded graphite," *Chemical Engineering Journal*, vol. 172, no. 2–3, pp. 1096–1102, 2011.
- [22] Q. W. Han, Q. Zhang, T. P. Li, and L. Zhang, "Testing on electricity character of modified expanded graphite," *China Material Technology and Equipment*, no. 6, pp. 39–41, 2009.
- [23] L. X. Sun, Z. G. Cheng, X. B. Zhao, Y. Cheng, M. Fu, and Q. Liu, "Study of the adsorption of formaldehyde on a modified exfoliated graphite," *Carbon*, no. 4, pp. 36–39, 2007.
- [24] Z. Wu, Y. L. Dong, D. Xu, P. Du, and Z. D. Han, "Study on the dispersion of expanded graphite in POE and its influences on the properties of composites," *Chemical Engineer*, pp. 4–7, 2011.
- [25] C. X. Yan, Z. G. Cheng, W. L. Wu, and M. Fu, "Research on decoloring of wastewater containing methyl orange by modified expanded graphite," *Journal of Jiangsu Polytechnic University*, vol. 22, no. 1, pp. 21–25, 2010.
- [26] C. F. Li, X. M. Luo, and B. Hou, "Surface modification and tribological performance of expanded graphite (EG) as lubricating oil additives," *Lubrication Engineering*, vol. 32, no. 7, pp. 111–113, 2007.
- [27] T. Placke, V. Siozios, R. Schmitz et al., "Influence of graphite surface modifications on the ratio of basal plane to "non-basal plane" surface area and on the anode performance in lithium ion batteries," *Journal of Power Sources*, vol. 200, pp. 83–91, 2012.
- [28] Y. H. Peng and S. X. Jiang, "Preparation of expanded graphite by potassium chlorate," *Non-Metallic Mines*, vol. 35, no. 3, pp. 38–40, 2012.
- [29] W. C. Shen and N. Z. Cao, "The porous structure and surface chemical state of expanded graphite," in *Proceedings of the European Carbon Conference*, vol. 18, pp. 348–349, The Royal Society of Chemistry.
- [30] M. Inagaki and T. Suwa, "Pore structure analysis of exfoliated graphite using image processing of scanning electron micrographs," *Carbon*, vol. 39, no. 6, pp. 915–920, 2001.
- [31] M. Inagaki, M. Toyoda, F. Y. Kang, Y. P. Zhang, and W. C. Shen, "Pore structure of exfoliated graphite—a report on a joint research project under the scientific cooperation program between NSFC and JSPS," *New Carbon Material*, vol. 18, pp. 241–249, 2003.
- [32] H. Zhao, W. Zhou, W. C. Shen, and F. Y. Kang, "Pore structure of exfoliated graphite and its varieties of liquid sorption," *Materials Science & Engineering*, vol. 20, no. 2, pp. 153–155, 2002.

Research Article

Photosensitizers from Spirulina for Solar Cell

Liqiu Wang,¹ Liang Tian,¹ Xinxin Deng,¹ Mengyi Zhang,²
Shuping Sun,¹ Wei Zhang,¹ and Lin Zhao¹

¹ College of Environmental and Chemical Engineering, Yanshan University, Qinhuangdao, Hebei 066004, China

² College of Life Sciences, Nankai University, Tianjin 300071, China

Correspondence should be addressed to Liqiu Wang; liqiuwang@tom.com

Received 8 November 2013; Accepted 11 December 2013; Published 2 February 2014

Academic Editor: Xinqing Chen

Copyright © 2014 Liqiu Wang et al. This is an open access article distributed under the Creative Commons Attribution License, which permits unrestricted use, distribution, and reproduction in any medium, provided the original work is properly cited.

Spirulina is a kind of blue-green algae with good photosynthetic efficiency and might be used for photovoltaic power generation. So this paper used living spirulina as novel photosensitizer to construct spirulina biosolar cell. The results showed that spirulina had the photoelectric conversion effect, and could let the spirulina biosolar cell have $70\text{ }\mu\text{A}$ photocurrent. Meanwhile, adding glucose sucrose or chitosan in the spirulina anode chamber, they could make the maxima current density of the cell greatly increased by $80\text{ }\mu\text{A}$, $100\text{ }\mu\text{A}$, and $84\text{ }\mu\text{A}$, respectively, and the sucrose could improve the maximum power density of the cell to 63 mW/m^{-2} . Phycobiliprotein played an important role in the photosynthesis of spirulina. So in this paper phycobiliprotein was extracted from spirulina to composite with squaraine dye to sensitize nanocrystalline TiO_2 photoanode for building dye sensitized solar cell, and the photoelectric properties of the cell also were investigated.

1. Introduction

Many photosensitizers [1–4] have been used to construct photo devices, such as organic dyes, inorganic nanomaterials, and biomass. Solar cells are the main photo devices that achieve the conversion of light energy into electrical energy. In particular, the solar cells based on photosynthesis principle of plants and algae, have great potential for the development and application [5–9]. In 1911, British botanist Potter discovered that microbes could produce current [10]. After the 1980s, electron transfer intermediates were widely used for improving output power of the microbial fuel cell greatly. In 1999, Tatsuo Yagishita et al. studied *Synechococcus* with glucose to make electricity production [11]. Researchers in University of Massachusetts found that iron reducing bacteria *Rhodospirillum* could metabolize carbohydrates and produce electricity [12]. US scientist Logan injected new vitality to the research of microbial fuel cell (MFC) by his studies in wastewater treatment and microbiological power generation [13–17]. Spirulina is ancient blue-green algae [18], and the growth and expansion of spirulina are rapid, easy, and convenient due to its cultivation pH 8.6–9.5 and lower demands for the environment [19, 20]. It has the solar energy utilization efficiency up to 18% and the photosynthetic

efficiency up to 43% (more than 3 times high to those of advanced plants) due to its phycobiliprotein. So this paper intended to extract phycobiliprotein from spirulina and used it as photosensitizer to sensitize nano- TiO_2 to equip the dye sensitized solar cell [21]. Meanwhile, we applied the living spirulina to build the spirulina biosolar cell [22, 23] and investigated the electrical properties of the cell and the influence of carbohydrates on photoelectric performance of the cell.

2. Experimental

2.1. *Spirulina Cultivation and Extraction of Phycobiliprotein*. Spirulina was cultivated with medium Zarrouk or medium spirulina at 28°C under 3000 lx light and 12 L/12 D photoperiod and was trained for 20 days [24] for the experiment. Phycobiliprotein was extracted from the spirulina by repeated freezing and melting technology under ultrasonic.

2.2. *TiO_2 Film and Its Sensitization with the Phycobiliprotein and Phycobiliprotein Squaraine*. Nanometer TiO_2 film was prepared on glass electrode by sol-gel from butyl titanate,

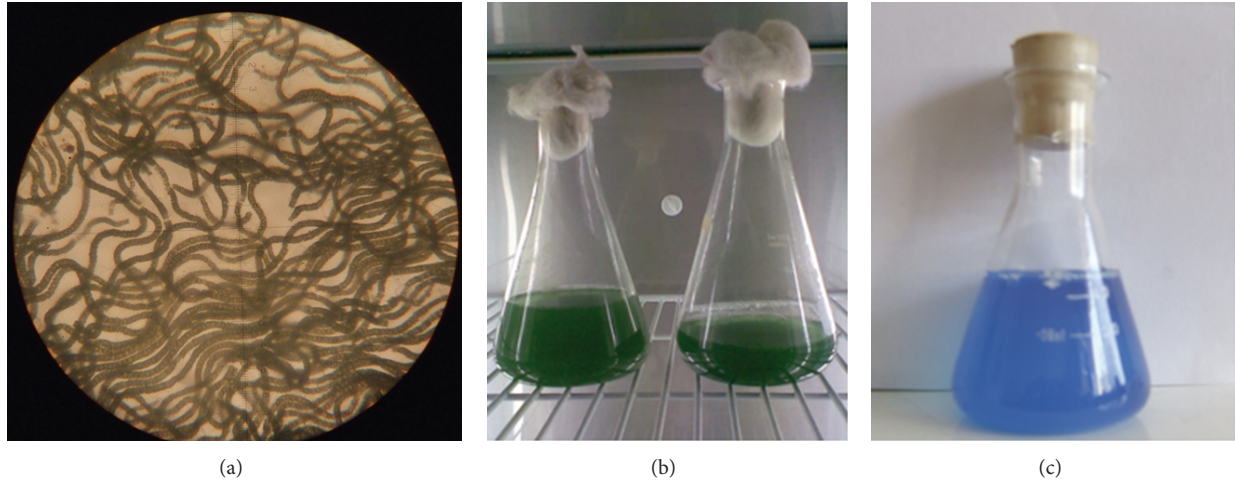


FIGURE 1: The sample of live spirulina under microscope (a) and in incubator (b) and the phycobiliprotein extracted (c).

diethanolamine, ethyl alcohol, and PEG and was sensitized with the phycobiliprotein or phycobiliprotein squaraine by impregnated method, respectively. The squaraine dye with N-p-carboxybenzyl group was synthesized by the reference [25].

2.3. Construction of Spirulina Biosolar Cell. Spirulina biosolar cell consisted of anode chamber and cathode chamber separated by clapboard, and the clapboard was equipped with proton exchange membrane (Nafion, 14 cm²). Two graphite electrodes in the anode and cathode chamber (about 10 cm²) were placed closely to both sides of the proton exchange membrane, and Ag/AgCl reference electrode in the anode chamber was close to the anode. Spirulina in the culture medium (240 mL) with or without glucose, sucrose, or chitosan was added to the anode chamber, while the culture medium (240 mL) was in the cathode chamber.

2.4. Detection of the Spirulina Biosolar Cell. The spirulina biosolar cell was placed under a xenon light source with the distance of 22 cm to the surface of anolyte. Photoelectric conversion performance of the solar cell was detected at 28°C under xenon lamp by electrochemical workstation.

3. Results and Discussion

3.1. Spirulina and Phycobiliprotein Photosensitizers. Figure 1 showed that the spirulina cultivated was green and spirochete, while the phycobiliprotein extracted from spirulina was blue. The maximum fluorescence emission wavelength of the phycobiliprotein was 650 nm. The phycobiliprotein sensitized the nano-TiO₂ film anode and assembled it into the dye sensitized solar cell with KI/I₂ acetonitrile solution as electrolyte and graphite as cathode. The results showed that the phycobiliprotein could improve the photovoltage and current of the nano-TiO₂ film to 273 mV and 4.2 mA, while using the phycobiliprotein squaraine as the photosensitizer, they could be 407 mV and 5.7 mA.

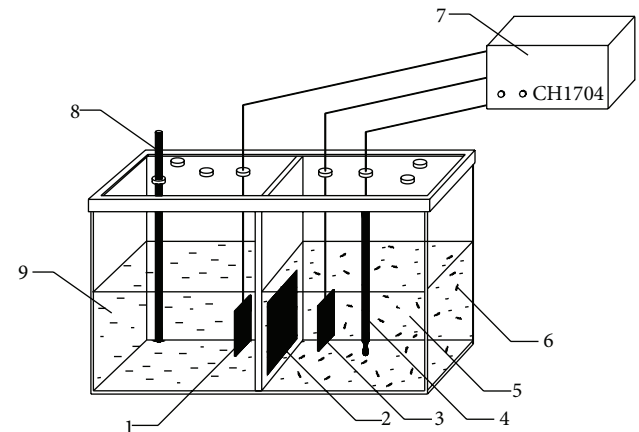


FIGURE 2: Schematic structure of the spirulina biosolar cell. 1: cathode, 2: proton exchange membrane, 3: anode, 4: reference electrode, 5: anolyte, 6: spirulina, 7: electrochemical workstation, 8: intake tube, and 9: catholyte.

3.2. The Spirulina Biosolar Cell and Its Working Principle. Structure and working principle of the spirulina biosolar cell were shown in Figures 2 and 3. Spirulina as electricity generation algae in the anolyte emitted electrons by its photosynthesis and respiration metabolism under light, and the electrons were transferred to the anode. At the same time, the protons were produced, then transferred to the cathode surface after penetrating the proton exchange membrane, and at last the protons reacted with oxygen and electrons to form water.

3.3. Photocurrent of the Spirulina Biosolar Cell. Figure 4 showed changing curves of the current with time for the cells under the dark and light. B1 represented the curve for the cell with 240 mL culture medium in each of the chambers, while S1 for the cell with 240 mL spirulina cultivated for twenty days in anode chamber and 240 mL culture medium in

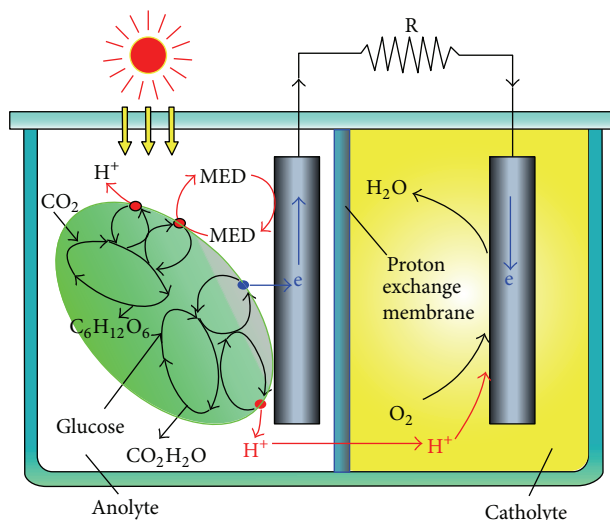


FIGURE 3: Electrons transfer mechanism of the spirulina biosolar cell.

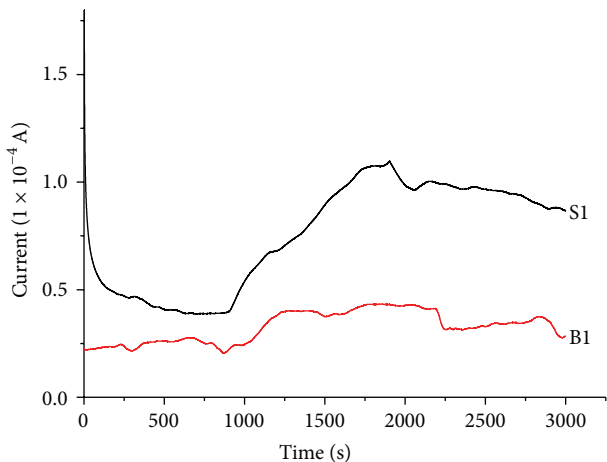


FIGURE 4: Current-time curves of the solar cell with and without spirulina under light and dark. B1: without spirulina; S1: with spirulina.

the cathode chamber. There was no light in 900 s. When lighting at the 900 s, the current rose, and fell when the lighting was removed at the 1900 s. B1 indicated that polarization current of the cell increased 19 μ A due to the elevated temperature of the solution and the reduction of internal resistance in solution under the illumination. The current of the cell under illumination had largely been increased (S1) by 70 μ A due to the electron produced from spirulina by photosynthesis, and after the light was removed, the current decreased a little. Figure 5 showed that the current of the spirulina biosolar cell should be increased by 240 μ A under the light for 6 h.

3.4. Influence of Carbohydrates on Photocurrent of the Solar Cell. Figure 6 showed the influence of carbohydrates on photocurrent of the spirulina biosolar cell under the dark

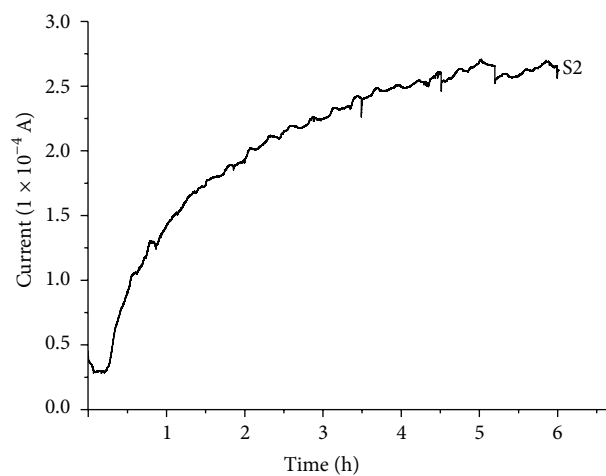


FIGURE 5: Current-time curve of the spirulina biosolar cell under the light for 6 h.

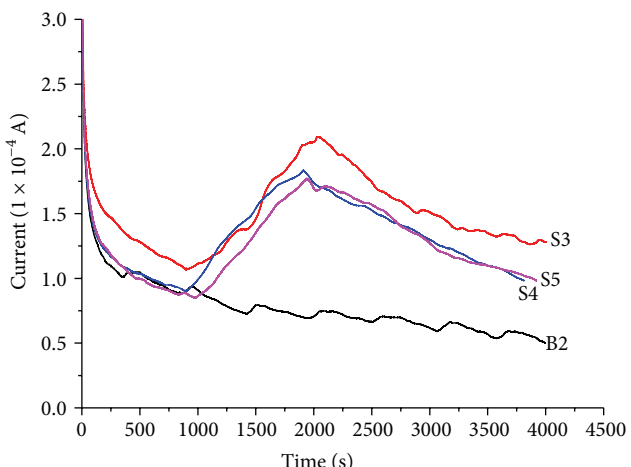


FIGURE 6: Current-time curves of the solar cell with sucrose in the anode chamber under the light and dark for three times. With spirulina, S3: the first time, S4: the second time, S5: the third time; B2.

and light. B2 indicated the changing of current with time for the cell with 2 g sucrose in 240 mL culture medium anode chamber. S3 showed that the current generated by the spirulina biosolar cell with 2 g sucrose in anode chamber had been increased by 100 μ A and indicated that the presence of sucrose could promote the electrons production significantly in photosynthesis of spirulina. After the light was removed, the current of the cell had a slight decrease. S4 and S5 explained that the maxima current only had a little decrease while repeating the experiments due to the slight loss of spirulina. Figure 7 showed that the photocurrent of the spirulina biosolar cell with 3.8 g sucrose in anode chamber was increased 389 μ A under the light for 4 h.

The influence of other carbohydrates on photocurrent of the spirulina biosolar cell was investigated. The results were shown in Table 1. The date indicated that glucose and chitosan made the photocurrent of the solar cell increase about 80 μ A

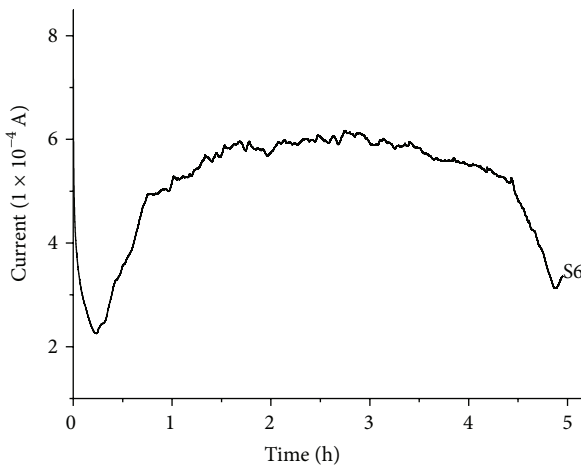


FIGURE 7: Current-time curve of the spirulina solar cell with sucrose under the light for 4 h.

TABLE 1: Current of the biosolar cell with spirulina and carbohydrates.

Anolyte	I_1 (μA)	I_2 (μA)	ΔI (μA)
C	20	39	19
C + S	32	102	70
C + S + Glucose	114	194	80
C + S + Sucrose	101	201	100
C + S + Chitosan	82	166	84

C: culture medium, S: spirulina, I_1 : current at 900 s, I_2 : current at 1900 s, and ΔI : the photocurrent difference.

and $84 \mu\text{A}$, respectively. Among them, the photoelectric conversion effect of the spirulina biosolar cell with sucrose was the best and could be improved approximately by $100 \mu\text{A}$.

Carbohydrates might improve the photosynthesis rate and photoelectric conversion of the spirulina biosolar cell due to their improving of the activity of hexokinase (an enzyme relating to the cyanobacterial photosynthesis). In the process, the carbohydrates were likely to compensate for lack of a carbon source and conducive to consumption reducing of ATP and NADPH in carbon utilization of the cells. These exogenous carbohydrates provided electrons as the endogenous starch or glucose did and made the electrons flow to PS I. Meanwhile, they improved proton gradient of crossing thylakoid membrane, photosynthetic phosphorylation level of cell, and the efficiency of emitting electrons from spirulina.

4. Conclusions

Phycobiliprotein-squaraine composite had good efficiency for widening and strengthening the UV-Vis light absorption and fluorescence emission of TiO_2 film and improving the photovoltage and photocurrent of the DSSC. Living spirulina had photoelectric conversion effect and could transmit the photoelectrons by its photosynthesis out of its cytomembrane in spirulina biosolar cell. Carbohydrates could improve the photocurrent of the solar cell further. Among them, sucrose

was the best additive and could let the current and the power density of the spirulina biosolar cell increase by $100 \mu\text{A}$ and 30 mW/m^{-2} , respectively. Spirulina biosolar cell will have a large potential for practical applications.

Conflict of Interests

The authors declare that they have no direct financial relation with the commercial identities mentioned in this paper that might lead to a conflict of interests for any of them.

Acknowledgments

The authors would like to thank Hebei Natural Science Foundation (no. B2011203231) and the Hebei Key Laboratory of Applied Chemistry Sea Grant (Yanshan University) for providing the financial support for this project.

References

- [1] B. O'Regan and M. Grätzel, "A low-cost, high-efficiency solar cell based on dye-sensitized colloidal TiO_2 films," *Nature*, vol. 353, no. 6346, pp. 737–740, 1991.
- [2] P. V. Kamat and G. C. Schatz, "Nanotechnology for next generation solar cells," *Journal of Physical Chemistry C*, vol. 113, no. 35, pp. 15473–15475, 2009.
- [3] L. Q. Wang, P. J. Wang, Y. Liu et al., "Near-infrared indocyanine materials for bioanalysis and nano- TiO_2 photoanodes of solar cell," *Journal of Nanomaterials*, vol. 2013, Article ID 695107, 5 pages, 2013.
- [4] T. F. Jiao, Y. Wang, Q. R. Zhang et al., "Preparation and photocatalytic property of gold nanoparticles by using two bolaform cholesteryl imide derivatives," *Journal of Dispersion Science and Technology*, vol. 34, no. 12, pp. 1675–1682, 2013.
- [5] Y. X. Shi, R. B. Guo, X. H. Xu, and X. L. Fan, "Preliminary study on microalgae solar cell," *Renewable Energy Resources*, vol. 27, no. 3, pp. 15–17, 2009.
- [6] H. He, Y. Feng, H. Li, and D. Li, "Construction of a microbial fuel cell using *Chlorella vulgaris*," *The Chinese Journal of Process Engineering*, vol. 9, no. 1, pp. 133–137, 2009.
- [7] X. Y. Wu, C. X. Zhou, Y. F. Zhi, and L. Y. Chen, "Progress of microbial fuel cell with microalgae," *Environmental Science and Technology*, vol. 35, no. 4, pp. 82–86, 2012.
- [8] Z. Yongjin, J. Pisciotta, R. B. Billmyre, and I. V. Baskakov, "Photosynthetic microbial fuel cells with positive light response," *Biotechnology and Bioengineering*, vol. 104, no. 5, pp. 939–946, 2009.
- [9] S. T. Jiang, Y. J. Guan, S. L. Bai, and Y. C. Yang, "Electricity generation characteristics of microbial fuel cell using glucose as substrate," *China Water and Wastewater*, vol. 25, no. 23, pp. 38–40, 2009.
- [10] M. C. Potter, "Electrical effects accompanying the decomposition of organic compounds," *Proceedings of the Royal Society of London B*, vol. 84, no. 571, pp. 260–276, 1911.
- [11] T. Yagishita, S. Sawayama, K. Tsukahara, and T. Ogi, "Effects of glucose addition and light on current outputs in photosynthetic electrochemical cells using *Synechocystis* sp. PCC6714," *Journal of Bioscience and Bioengineering*, vol. 88, no. 2, pp. 210–214, 1999.

- [12] S. K. Chaudhuri and D. R. Lovley, "Electricity generation by direct oxidation of glucose in mediatorless microbial fuel cells," *Nature Biotechnology*, vol. 21, no. 10, pp. 1229–1232, 2003.
- [13] B. E. Logan, "Simultaneous wastewater treatment and biological electricity generation," *Water Science and Technology*, vol. 52, no. 1-2, pp. 31–37, 2005.
- [14] G. V. Subhash, R. Chandra, and S. V. Mohan, "Microalgae mediated bio-electrocatalytic fuel cell facilitates bioelectricity generation through oxygenic photomixotrophic mechanism," *Bioresource Technology*, vol. 136, pp. 644–653, 2013.
- [15] E. Fernando, T. Keshavarz, and G. Kyazze, "Simultaneous co-metabolic decolourisation of azo dye mixtures and bioelectricity generation under thermophilic (50°C) and saline conditions by an adapted anaerobic mixed culture in microbial fuel cells," *Bioresource Technology*, vol. 127, pp. 1–8, 2013.
- [16] C. C. Lin, C. H. Wei, C. I. Chen, C. J. Shieh, and Y. C. Liu, "Characteristics of the photosynthesis microbial fuel cell with a spirulina platensis biofilm," *Bioresource Technology*, vol. 135, pp. 640–643, 2013.
- [17] J. C. W. Lan, K. Raman, C. M. Huang, and C. M. Chang, "The impact of monochromatic blue and red LED light upon performance of photo microbial fuel cells (PMFCs) using chlamydomonas reinhardtii transformation F5 as biocatalyst," *Biochemical Engineering Journal*, vol. 78, pp. 39–43, 2013.
- [18] G. L. Jin, S. B. Zhang, and H. Y. Wang, "The effect of vitamin C on growth of alga spirulina platensis," *Fisheries Science*, vol. 27, no. 4, pp. 203–204, 2008.
- [19] F. F. Guo, W. Zong, and Y. W. Qu, "Prospects of development and use of spirulina," *Science and Technology Information*, vol. 6, pp. 16–16, 2008.
- [20] Z. H. Song and G. I. Huang, "Toxicity of triphenyltin to Spirulina subsalsa," *Bulletin of Environmental Contamination and Toxicology*, vol. 64, no. 5, pp. 723–728, 2000.
- [21] A. C. M. S. Esteban and E. P. Enriquez, "Graphene-anthocyanin mixture as photosensitizer for dye-sensitized solar cell," *Solar Energy*, vol. 98, pp. 392–399, 2013.
- [22] R. A. Timmers, D. P. B. T. B. Strik, H. V. M. Hamelers, and C. J. N. Buisman, "Electricity generation by a novel design tubular plant microbial fuel cell," *Biomass and Bioenergy*, vol. 51, pp. 60–67, 2013.
- [23] R. A. Timmers, D. P. B. T. B. Strik, H. V. M. Hamelers, and C. J. N. Buisman, "Characterization of the internal resistance of a plant microbial fuel cell," *Electrochimica Acta*, vol. 72, pp. 165–171, 2012.
- [24] E. J. Olguín, "Phycoremediation: key issues for cost-effective nutrient removal processes," *Biotechnology Advances*, vol. 22, no. 1-2, pp. 81–91, 2003.
- [25] L. Q. Wang, X. J. Peng, W. B. Zhang, F. Yin, J. N. Cui, and X. Q. Gao, "Synthesis and spectral properties of novel water-soluble near-infrared fluorescent indocyanines," *Chinese Chemical Letters*, vol. 16, no. 3, pp. 341–344, 2005.

Research Article

Adsorption of Monobutyl Phthalate from Aqueous Phase onto Two Macroporous Anion-Exchange Resins

Zhengwen Xu,^{1,2} Yunlong Zhao,^{1,2} Jing Shi,³ Jiangang Lu,^{1,2} Ling Cheng,^{1,2} and Mindong Chen^{1,2}

¹ Jiangsu Key Laboratory of Atmospheric Environment Monitoring and Pollution Control,
Nanjing University of Information Science and Technology, Nanjing 210044, China

² School of Environmental Science & Engineering, Nanjing University of Information Science and Technology,
Nanjing 210044, China

³ School of Sciences, China Pharmaceutical University, Nanjing 211198, China

Correspondence should be addressed to Zhengwen Xu; zhouxu3037@sina.com and Jing Shi; 347475315@qq.com

Received 19 November 2013; Accepted 13 December 2013; Published 8 January 2014

Academic Editor: Qingrui Zhang

Copyright © 2014 Zhengwen Xu et al. This is an open access article distributed under the Creative Commons Attribution License, which permits unrestricted use, distribution, and reproduction in any medium, provided the original work is properly cited.

As new emerging pollutants, phthalic acid monoesters (PAMs) pose potential ecological and human health risks. In the present study, adsorption performance of monobutyl phthalate (MBP) onto two macroporous base anion-exchange resins (D-201 and D-301) was discussed. It was found that the adsorption isotherms were best fitted by the Langmuir equation while the adsorption kinetics were well described by pseudo-first-order model. Analyses of sorption isotherms and thermodynamics proved that the adsorption mechanisms for DBP onto D-201 were ion exchange. However, the obtained enthalpy values indicate that the sorption process of MBP onto D-301 is physical adsorption. The equilibrium adsorption capacities and adsorption rates of DBP on two different resins increased with the increasing temperature of the solution. D-301 exhibited a higher adsorption capacity of MBP than D-201. These results proved that D-301, as an effective sorbent, can be used to remove phthalic acid monoesters from aqueous solution.

1. Introduction

Water pollution by phthalic acid esters (PAEs) has attracted increasing attention in recent decades. They are widely used as plasticizers in the manufacture of polyvinyl chloride [1]. Phthalic acid monoesters (PAMs) as degradation products of PAEs or synthetic intermediates for the preparation of PAEs have attained more attention. They are mutagenic endocrine disrupting compounds, posing the adverse reproductive effects on humans and wildlife equal to PAEs. Some studies have shown that the hydrolytic breakdown products of some PAEs have higher toxicity than PAEs [2]. Recently, many PAMs have been detected in surface water, sea water, and landfill leachate [3]. Previous research proved that some PAMs have greater solubility than corresponding PAEs, especially for monomethyl phthalate (MMP, 3721 mg/L), monobutyl phthalate (MBP, 409 mg/L), and mono-ethyl-hexyl-phthalate (MEHP, 1.85 mg/L). Thus, some polluted

aquatic environment may contain high concentration of PAMs [4, 5]. For instance, Jonsson found that, in landfill leachate, MBP appeared at a concentration of 2500 µg/L that was much higher than that of dibutyl phthalate (DBP) (50 µg/L) [6]. Therefore, as a new type of organic pollutants, how to effectively remove PAMs from aqueous solution is an important issue.

Many previous studies have reported that PAMs can be removed from aqueous environment through different methods, such as activated sludge process [7] and adsorption [8, 9]. In the active sludge process, PAMs can be further broken down to phthalic acid, benzoic acid, and finally carbon dioxide [10, 11]. However, this process was reported to be relatively slow and is not expected to be an effective method, because of the toxicity of PAMs to microorganism [12, 13]. Earlier research results indicated that PAMs can be adsorbed by chitosan, but the adsorption capability (0.015 mg/g) was too low to application in practice [10].

TABLE 1: Salient properties of polymeric adsorbents.

	D201	D301
BET surface area (m^2/g)	25.6	31.8
Particle size (mm)	0.4~0.7	0.4~0.6
Cross-link density (%)	8	8
Appearance	Ivory white	Ivory white
Functional groups species	Quaternary amine (-CHN ⁺ (CH ₃) ₃)	Tertiary amine (-CH ₂ N(CH ₃) ₂)
Amino content (m mol/g)	3.7	4.9

The primary objective of the present study is to find a new method for effective removal of PAMs from aqueous solution. MBP is chosen as a representative target contaminant because of its widespread occurrence in aqueous environment. The adsorption performance of MBP onto a macroporous strongly basic anion exchanger D-201 and a macroporous weakly basic anion exchanger D-301 was investigated.

2. Materials and Methods

2.1. Materials. Sodium hydroxide, hydrochloric acid, phosphoric acid, ethanol, methanol, and monobutyl phthalate (MBP) were used in this study. All chemicals are of analytic grade and were purchased from Nanjing reagent station. D-201 and D-301 were provided by Hangzhou Zhengguang Resin Co. Ltd. (Zhejiang Province, China). Physicochemical properties of the sorbents used in this study are presented in Table 1.

2.2. Resin Pretreatment. Prior to use, all the resins were packed in column and first rinsed with DI (deionized), and then with 50 bed volumes (BV) of 1.0 N NaOH followed by DI washing until neutral pH was achieved. After this, the column was subjected to acidic flushing by introducing 50 BV of 1.0 N HCl and again DI flushing to neutral pH. Finally, the resin was washed with ethanol using the same method and desiccated at 308 K for 24 h before use [14].

2.3. Sorption Experiments. Batch sorption tests were carried out in 100 mL glass bottles. To start the experiment, 0.050 g of sorbent was introduced into 50 mL solution containing a known concentration (50, 100, 150, 200, 250, and 300 mg/L) of MBP. The flask then was transferred to a G24 model incubator shaker with thermostat (Jintan Medical Instrument Factory, Jiangsu Province, China) and shaken under 150 rpm for 24 h at desired temperature (288 K, 298 K, and 313 K) to ensure equilibrium of the adsorption process. A series of parallel kinetics experiments were carried out at different conditions: the concentration and volume of MBP solutions, mass of resins, agitated speed (DF-101B model stirrer, Nanjing Yuhua Instrument Co. Ltd., Jiangsu Province, China), and temperature (TH-10 model intelligence electrothermostatic water cabinet, Ningbo Tianheng instrument factory, Zhejiang Province, China) were 20 mg/L, 2000 mL, 1 g, 400 rpm, and 288 K, 298 K, and 313 K, respectively. With MBP sorption at

different time intervals, 1 mL solution of MBP was extracted for detecting.

2.4. Analysis. Measurements of the BET surface area were based on N₂ adsorption data from an Autosorb-IQ-AG-MP Sorptomatic apparatus (Quantachrome Instruments, USA).

Concentrations of MBP in the solution were analyzed by HPLC (Agilent, 1200, USA) equipped with a reverse phase column (Agilent, TC-C18, 3.19 mm × 150 mm) and a UV detector. The mobile phase was composed of 68% methanol and 32% purified water and the detective wavelength was 228 nm [15]. Prior to analysis, the phosphorous acid was used to adjust the sample solution to acidity [16] (about pH = 4.0).

The anion-exchange capacity of D-201 and D-301 was determined by the literature method [17].

The rate of MBP adsorption, q_t (mg/g), was calculated using the relation

$$q_t = \frac{(C_i - C_t)V}{M} \quad (1)$$

with C_i (mg/L) being the initial concentration of MBP, C_t (mg/L) representing the concentration of time, V (L) being the volume of solution, and M (g) the mass of dry adsorbents [10].

3. Result and Discussion

3.1. Characterization of Sorbent. Some important physical-chemical properties of D-201 and D-301 are present in Table 1. As can be seen from Table 1, the two exchangers have low surface area (less than 40 m^2/g) and a large number of functional groups. For the strongly basic anion-exchange resin D-201, it contains 3.7 mmol/g quaternary amine; for the weak base anion exchanger, the exchangeable capacity of D-301 is 4.9 mmol/g. These two adsorbents show a similar particle size and cross-link density.

3.2. Adsorption Isotherms. Adsorption isotherms of MBP onto D-201 and D-301 (in Figure 1) are represented by Langmuir model and Freundlich model [18]:

$$\frac{1}{q_e} = \frac{1}{K_L q_m C_e} + \frac{1}{q_m}, \quad (2)$$

$$q_e = K_f C_e^{1/n},$$

where q_e (mg/g) is the equilibrium adsorption capacity, C_e (mg/L) represents the solute concentration in equilibrium, K_f and n are the Freundlich constants to be determined, q_m (mg/g) is the maximal sorption capacity, and K_L (L/mg) is a binding constant.

It can be observed from Figure 1 that the amounts adsorbed of MBP on D-201 and D-301 are increased with the increase of equilibrium concentrations, indicating the spontaneous process. Results in Table 2 show that the Langmuir model and the Freundlich model representing the MBP adsorption isotherms were different by the value of R^2 . The Langmuir model may be more reasonable

TABLE 2: Adsorption isotherm parameters of D-201 and D-301.

Adsorbent	T/K	q_m (mg/g)	Langmuir		Freundlich		
			K_L (L/mg)	R^2	K_F	n	R^2
D-201	288	284.6	0.043	0.994	51.1	3.137	0.916
	298	287.8	0.050	0.990	57.0	3.283	0.913
	313	288.3	0.098	0.943	82.1	4.014	0.942
D-301	288	388.9	0.088	0.987	84.7	3.159	0.887
	298	390.7	0.107	0.987	98.7	3.462	0.901
	313	400.0	0.128	0.998	123.5	4.043	0.943

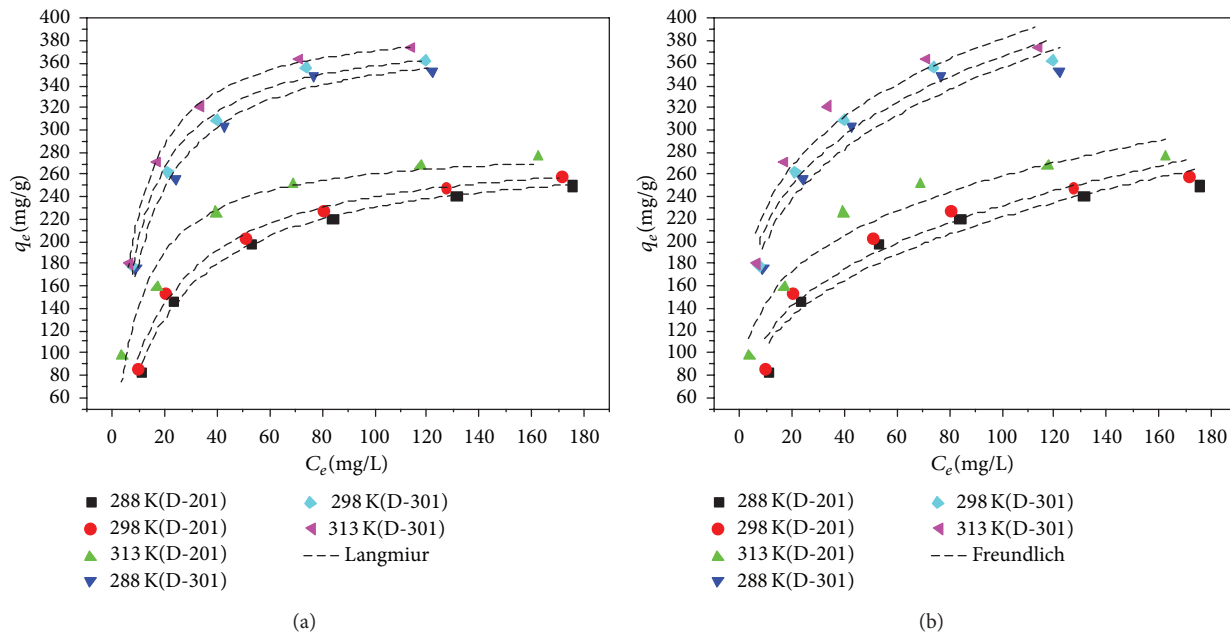


FIGURE 1: Equilibrium adsorption isotherms of MBP on D-201 and D-301. (a) Fitting by Langmuir equation. (b) Fitting by Freundlich equation.

than Freundlich model. q_m values increased by the rise of temperature, which may also indicate that the adsorption of MBP onto D-201 or D-301 was an endothermic process. In other words, higher temperature is more favorable for MBP adsorption onto D-201 and D-301. This result indicated that the function groups of D-201 and D-301 play an important role in the removal process of MBP from aqueous solution. As shown in Figure 1 and Table 2, the maximum adsorption capacity of MBP on D-301 is much higher than that on D-201. The more excellent adsorption property of D-301 than D-201 may be attributed to its large number of functional groups. In addition, all the values of n , the Freundlich parameter, are greater than one, which means that the adsorption of MBP on the two sorbents is the optimal adsorption [19].

3.3. Thermodynamic Analysis. Thermodynamic parameters for the adsorption process can be calculated as

$$\begin{aligned} \Delta G &= -RT \ln K_L, \\ \ln K_L &= -\frac{\Delta H}{RT} + A, \\ \Delta G &= \Delta H - T\Delta S, \end{aligned} \quad (3)$$

TABLE 3: Thermodynamic parameters of D-201 and D-301.

Adsorbent	ΔH (kJ/mol)	ΔG (kJ/mol)			ΔS (J/mol)
		288 K	298 K	313 K	
D-201	25.32	7.72	7.11	6.19	61.11
D-301	11.12	5.78	5.59	5.32	18.54

where T is the absolute temperature in K and K_L is the Langmuir adsorption constant. R is the gas constant with a value of $8.314 \text{ J}/(\text{mol}\cdot\text{K})$, and A is a constant [20, 21]. The enthalpy change ΔH was determined by plotting $\ln K_L$ versus $1/T$ (Figure 2). Thermodynamic parameters of MBP adsorption onto D-201 and D-301 are listed in Table 3.

Generally, the enthalpy change due to chemical adsorption ($>20 \text{ kJ/mol}$) is considerably larger than that due to physical adsorption ($<20 \text{ kJ/mol}$). The adsorption enthalpies in Table 3 suggest that the adsorption process of MBP on D-201 might be considered to be ion exchange in nature. However, the agreement of MBP adsorption enthalpy with values for physisorption (0 to 20 kJ/mol) indicates that MBP was adsorbed onto D-301 via physical adsorption.

TABLE 4: Adsorption kinetic parameters of D-201 and D-301.

Temperature	Pseudo-first-order kinetic model		Pseudo-second-order kinetic model	
	k_1 (1/min)	R^2	k_2 (g/kg·min)	R^2
D-201	0.016	0.996	185.5	0.979
D-301	0.016	0.998	189.4	0.990

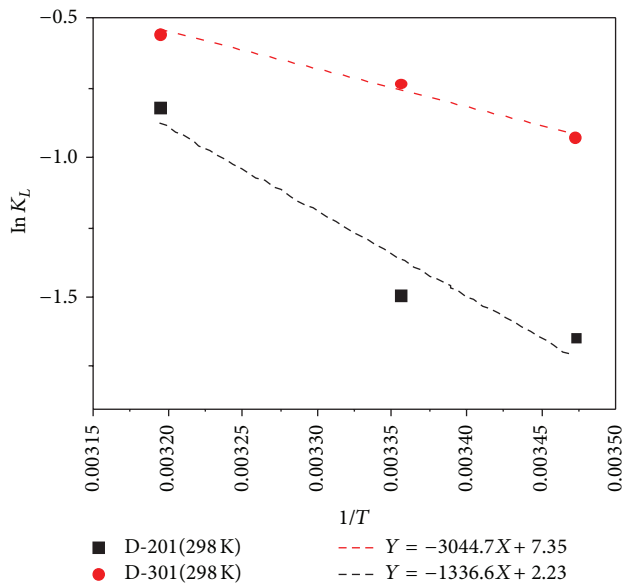


FIGURE 2: Van't Hoff plot for the adsorption of MBP onto D-201 and D-301.

The positive ΔS values in Table 3 imply that MBP adsorption onto D-201 and D-301 is entropy-driven process [22].

3.4. Adsorption Kinetic. Figure 3 shows sorption kinetics of MBP onto D-201 and D-301. It is clear that about 250 min was required to reach sorption equilibrium for the two adsorbents. Pseudo-first- and pseudo-second-order models were fitted to the kinetic data [23]:

$$\begin{aligned} \ln(q_e - q_t) &= \ln q_e - k_1 t, \\ \frac{1}{q_t} &= \frac{1}{k_2 q_e^2 t} + \frac{1}{q_e}, \end{aligned} \quad (4)$$

where k_1 and k_2 are the pseudo-first-order model and pseudo-second-order model constants to be determined. The kinetic parameters are determined and listed in Table 4.

From Table 4 we can see that the pseudo-first-order model gave a better representation of the data than the pseudo-second-order model. It is apparently clear that the values of the rate constant k_1 in Table 4 are similar to each adsorbent.

4. Conclusion

In summary, this work provides a new approach to remove MBP from an aqueous solution, using two macroporous

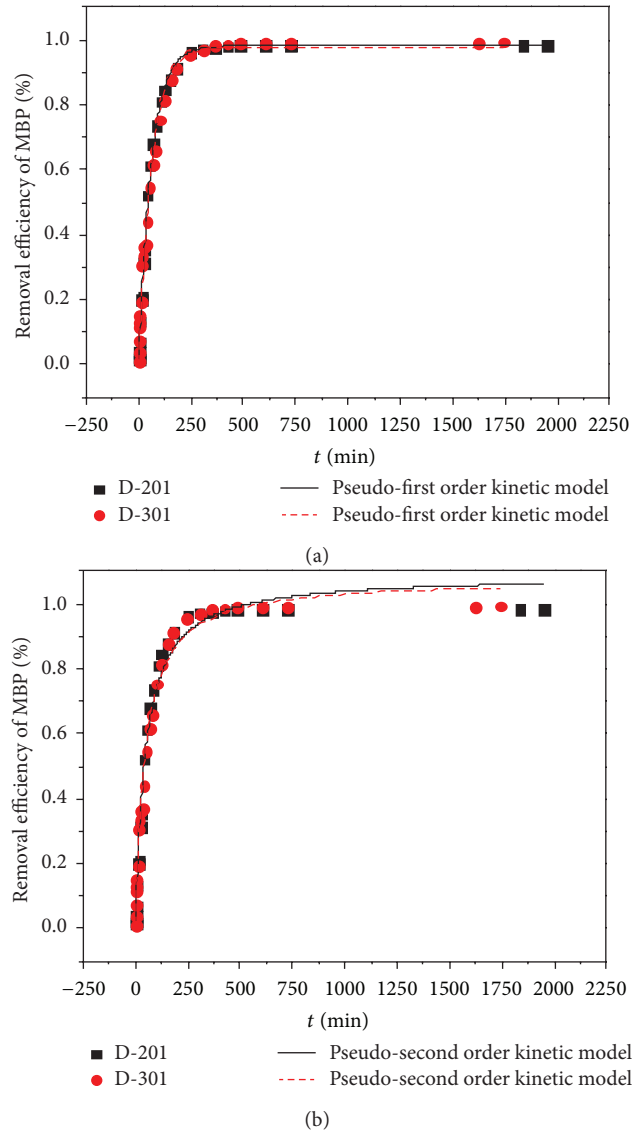


FIGURE 3: Adsorption kinetics of MBP onto D-201 and D-301 at 298 K. (a) Fitting by Pseudo-first-order equation. (b) Fitting by Pseudo-second-order equation.

anion-exchange resins. The results reported herein demonstrate that the macroporous weakly basic anion exchanger D-301 was a highly efficient material for MBP removal. The satisfactory adsorption capability of D-301 displays its potential for PAMs removal in aqueous environment.

Conflict of Interests

The authors declare that there is no conflict of interests regarding the publication of this paper.

Acknowledgments

The authors wish to thank the National Natural Science Foundation of China (Grant no. 21107050) and a project funded by the Priority Academic Program Development of Jiangsu Higher Education Institutions for supporting this study.

References

- [1] X. W. Peng, L. J. Feng, and X. G. Li, "Pathway of diethyl phthalate photolysis in sea-water determined by gas chromatography-mass spectrometry and compound-specific isotope analysis," *Chemosphere*, vol. 90, no. 2, pp. 220–226, 2013.
- [2] C. K. Lim, S. Kim, D. S. Ko et al., "Differential cytotoxic effects of mono-(2-ethylhexyl) phthalate on blastomere-derived embryonic stem cells and differentiating neurons," *Toxicology*, vol. 264, no. 3, pp. 145–154, 2009.
- [3] J. D. Blair, M. G. Ikonomou, B. C. Kelly, B. Surridge, and F. A. P. C. Gobas, "Ultra-trace determination of phthalate ester metabolites in seawater, sediments, and biota from an urbanized marine inlet by LC/ESI-MS/MS," *Environmental Science and Technology*, vol. 43, no. 16, pp. 6262–6268, 2009.
- [4] A. M. Calafat, A. R. Slakman, M. J. Silva, A. R. Herbert, and L. L. Needham, "Automated solid phase extraction and quantitative analysis of human milk for 13 phthalate metabolites," *Journal of Chromatography B*, vol. 805, no. 1, pp. 49–56, 2004.
- [5] S. Jonsson, J. Ejlertsson, A. Ledin, I. Mersiowsky, and B. H. Svensson, "Mono- and diesters from o-phthalic acid in leachates from different European landfills," *Water Research*, vol. 37, no. 3, pp. 609–617, 2003.
- [6] S. Jonsson, J. Ejlertsson, and B. H. Svensson, "Behaviour of mono- and diesters of o-phthalic acid in leachates released during digestion of municipal solid waste under landfill conditions," *Advances in Environmental Research*, vol. 7, no. 2, pp. 429–440, 2003.
- [7] S. V. Otton, S. Sura, J. Blair, M. G. Ikonomou, and F. A. P. C. Gobas, "Biodegradation of mono-alkyl phthalate esters in natural sediments," *Chemosphere*, vol. 71, no. 11, pp. 2011–2016, 2008.
- [8] B. V. Chang, Y. S. Lu, S. Y. Yuan, T. M. Tsao, and M. K. Wang, "Biodegradation of phthalate esters in compost-amended soil," *Chemosphere*, vol. 74, no. 6, pp. 873–877, 2009.
- [9] H. Liu, D. Zhang, M. J. Li, L. Tong, and L. Feng, "Competitive adsorption and transport of phthalate esters in the clay layer of JiangHan plain, China," *Chemosphere*, vol. 92, no. 11, pp. 1542–1549, 2013.
- [10] J. Catherine, S. H. Liu, and J. F. Kennedy, "Comparative study of the adsorption on chitosan beads of phthalate esters and their degradation products," *Carbohydrate Polymers*, vol. 81, no. 3, pp. 640–644, 2010.
- [11] T. T. H. Pham, R. D. Tyagi, S. K. Brar, and R. Y. Surampalli, "Effect of ultrasonication and Fenton oxidation on biodegradation of bis(2-ethylhexyl) phthalate (DEHP) in wastewater sludge," *Chemosphere*, vol. 82, no. 6, pp. 923–928, 2011.
- [12] S. Chatterjee and T. K. Dutta, "Metabolism of butyl benzyl phthalate by Gordonia sp. strain MTCC 4818," *Biochemical and Biophysical Research Communications*, vol. 309, no. 1, pp. 36–43, 2003.
- [13] T. Saito, P. Hong, R. Tanabe, K. Nagai, and K. Kato, "Enzymatic hydrolysis of structurally diverse phthalic acid esters by porcine and bovine pancreatic cholesterol esterases," *Chemosphere*, vol. 81, no. 11, pp. 1544–1548, 2010.
- [14] B. C. Pan, Q. X. Zhang, F. W. Meng et al., "Sorption enhancement of aromatic sulfonates onto an animated hyper-cross-linked polymer," *Environmental Science and Technology*, vol. 39, no. 9, pp. 3308–3313, 2005.
- [15] Z. W. Xu, W. Z. Zhang, L. Lv, B. C. Pan, P. Lan, and Q. Zhang, "A new approach to catalytic degradation of dimethyl phthalate by a macroporous OH-type strongly basic anion exchange resin," *Environmental Science and Technology*, vol. 44, no. 8, pp. 3130–3135, 2010.
- [16] K. Kato, M. J. Silva, L. L. Needham, and A. M. Calafat, "Determination of total phthalates in urine by isotope-dilution liquid chromatography-tandem mass spectrometry," *Journal of Chromatography B*, vol. 814, no. 2, pp. 355–360, 2005.
- [17] B. Von Oepen, W. Kordel, and W. Klein, "Sorption of nonpolar and polar compounds to soils: processes, measurements and experience with the applicability of the modified OECD-Guideline 106," *Chemosphere*, vol. 22, no. 3-4, pp. 285–304, 1991.
- [18] J. L. Wang, L. J. Chen, C. Shi, and Q. Yi, "Microbial degradation of phthalic acid esters under anaerobic digestion of sludge," *Chemosphere*, vol. 41, no. 8, pp. 1245–1248, 2000.
- [19] Q. J. Zhang, Z. W. Xu, K. Zheng et al., "Adsorption behavior of p-nitroaniline on macroporous polymer and its application," *Ion Exchange and Adsorption*, vol. 22, no. 6, pp. 503–511, 2006.
- [20] Y. Liu, "Is the free energy change of adsorption correctly calculated?" *Journal of Chemical and Engineering Data*, vol. 54, no. 7, pp. 1981–1985, 2009.
- [21] C. H. Wu, "Studies of the equilibrium and thermodynamics of the adsorption of Cu²⁺ onto as-produced and modified carbon nanotubes," *Journal of Colloid and Interface Science*, vol. 311, no. 2, pp. 338–346, 2007.
- [22] S. Shrestha, G. Son, S. H. Lee, and T. G. Lee, "Isotherm and thermodynamic studies of Zn (II) adsorption on lignite and coconut shell-based activated carbon fiber," *Chemosphere*, vol. 92, no. 8, pp. 1053–1106, 2013.
- [23] D. M. Neveskaia, A. Santianes, V. Muñoz, and A. Guerrero-Ruiz, "Interaction of aqueous solutions of phenol with commercial activated carbons: an adsorption and kinetic study," *Carbon*, vol. 37, no. 7, pp. 1065–1074, 1999.

Research Article

Investigation on the Structure and Electrochemical Properties of La-Ce-Mg-Al-Ni Hydrogen Storage Alloy

Yuqing Qiao,^{1,2} Jianyi Xi,² Minshou Zhao,² Guangjie Shao,²
Yongchun Luo,³ and Limin Wang¹

¹ State Key Laboratory of Rare Earth Resources Utilization, Changchun Institute of Applied Chemistry, CAS, Changchun 130022, China

² College of Environmental and Chemical Engineering, Yanshan University, Qinhuangdao, Hebei 066004, China

³ Department of Materials Science and Engineering, Lanzhou University of Technology, Lanzhou, Gansu 730050, China

Correspondence should be addressed to Yuqing Qiao; qiaoyq@ysu.edu.cn and Limin Wang; lmwang@ciac.jl.cn

Received 28 October 2013; Accepted 23 November 2013

Academic Editor: Xinqing Chen

Copyright © 2013 Yuqing Qiao et al. This is an open access article distributed under the Creative Commons Attribution License, which permits unrestricted use, distribution, and reproduction in any medium, provided the original work is properly cited.

Structure and electrochemical characteristics of $\text{La}_{0.96}\text{Ce}_{0.04}\text{Mg}_{0.15}\text{Al}_{0.05}\text{Ni}_{2.8}$ hydrogen storage alloy have been investigated. X-ray diffraction analyses reveal that the $\text{La}_{0.96}\text{Ce}_{0.04}\text{Mg}_{0.15}\text{Al}_{0.05}\text{Ni}_{2.8}$ hydrogen storage alloy consisted of a $(\text{La}, \text{Mg})\text{Ni}_3$ phase with the rhombohedral PuNi_3 -type structure and a LaNi_5 phase with the hexagonal CaCu_5 -type structure. TEM shows that the alloy is multicrystal with a lattice space 0.187 nm. EDS analyse shows that the content of Mg is 3.48% (atom) which coincide well with the designed composition of the electrode alloy. Electrochemical investigations show that the maximum discharge capacity of the alloy electrode is 325 mAh g^{-1} . The alloy electrode has higher discharge capacity within the discharge current density span from 60 mA g^{-1} to 300 mA g^{-1} . Electrochemical impedance spectroscopy measurements indicate that the charge transfer resistance R_T on the alloy electrode surface and the calculated exchange current density I_0 are 0.135 Ω and 1298 mA g^{-1} , respectively; the better electrochemical reaction kinetic of the alloy electrode may be responsible for the better high-rate dischargeability.

1. Introduction

La-Mg-Ni system alloys are promising materials owing to their higher electrochemical capacity compared to AB_5 -type alloys; however, the poor cycling stability and HRD of the La-Mg-Ni hydrogen storage alloys have prevented it from being practically used as electrode alloys for Ni-MH battery [1–14]. According to the literature [15], the capacity degradation during cycling of La-Mg-Ni based hydrogen storage electrode alloy is influenced mainly by two factors: the passivation due to the formation of $\text{La}(\text{OH})_3$ and $\text{Mg}(\text{OH})_2$ on the alloy surface and the accelerated corrosion rate of the active components due to the large molar volume of hydrogen V_H of the alloy hydrides. As the alloy electrode with a large V_H undergoes a large cell volume expansion/contraction during charge/discharge cycle, a higher degree of pulverization resulted and thus more surface area is exposed to the

corrosive electrolyte, which would lead to a lower cycling stability [16–18].

The partial substitution of Al for Ni in La-Mg-Ni based alloy can improve the cycling stability due to the noticeable decrease in the cell volume expansion rate ($\Delta V/V$) on hydriding [19, 20]. According to the literature [21], Al was helpful to the formation of LaNi_5 phase in $\text{La}_{0.67}\text{Mg}_{0.33}\text{Ni}_{3.0-x}\text{Al}_x$ ($x = 0, 0.1, 0.2, 0.3$) hydrogen storage alloys. LaNi_5 phase with CaCu_5 type appeared when Al was added. The increase of Al content leads to an increase of content of LaNi_5 phase, and the main phase of the alloy is LaNi_5 phase with $x = 0.3$. According to the literature [22, 23], rare earth elements (such as Dy and Pr) are helpful to decrease the cell volume of LaNi_5 phase. For V-based solid solution alloy [24], the addition of Ce can improve the dynamic performance, which makes the charge transfer resistance (R_T) decrease and the exchange current density (I_0) increase markedly. Just for

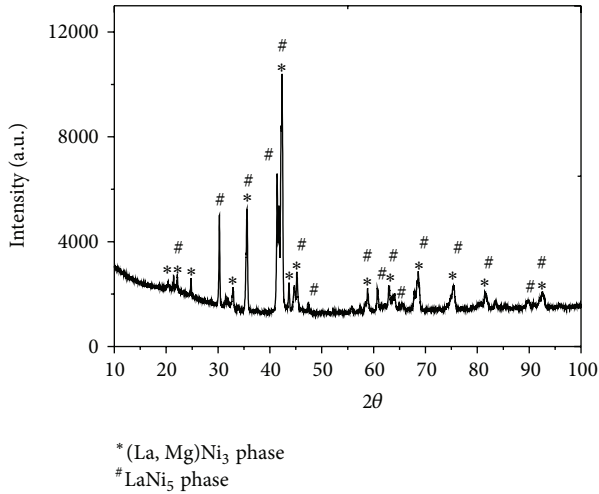


FIGURE 1: X-ray diffraction patterns of $\text{La}_{0.96}\text{Ce}_{0.04}\text{Mg}_{0.15}\text{Al}_{0.05}\text{Ni}_{2.8}$ alloy.

those considerations, Al has been used to partly substitution for Ni, Ce has been used to partly substitution for La, and the structure and electrochemical properties of the La-Ce-Mg-Al-Ni hydrogen storage electrode alloy have been investigated in this paper.

2. Experimental

$\text{La}_{0.96}\text{Ce}_{0.04}\text{Mg}_{0.15}\text{Al}_{0.05}\text{Ni}_{2.8}$ hydrogen storage electrode alloy was prepared by induction melting under argon and then remelted to ensure for homogeneity. The purity of the individual starting metal was higher than 99.5 mass%. The prepared electrode alloy was mechanically crushed to particles and then pulverized to a fine powder of about 300 mesh, and the sample powder was used for XRD, TEM, and electrochemical characteristics. Crystal structure of La-Ce-Mg-Al-Ni hydrogen storage electrode alloy was investigated by XRD (CuK α , Si internal standard) on Rigaku D/max 2500pc X-ray diffraction meter using JAD5 software and by TEM on JEM-2010.

The metal hydride electrode was prepared by pressing the mixture of alloy powder with carbonyl nickel powder in a weight ratio of 1:5 into a tablet with a diameter about 10 mm and a thickness about 1.5 mm. The electrochemical properties were performed on a DC-5 battery testing instrument using a half-cell system which consists of a metal hydride electrode as the negative electrode and a sintered $\text{Ni}(\text{OH})_2/\text{NiOOH}$ electrode with excess capacity in 6 mol L⁻¹ KOH electrolyte solution; the cut-off voltage for discharge was 0.8 V.

Electrochemical impedance spectroscopy (EIS) was used to clarify the kinetic properties of dehydrating action, such as the charge-transfer resistance (R_T) and the exchange current density (I_0). After the test electrodes were completely activated, EIS measurements were conducted at 50% depth of discharge (DOD) using a Solartron SI1187 electrochemical interface with ZPLOT electrochemical impedance software and 1255B frequency response analyzer. The EIS spectra of the

electrodes were obtained in the frequency range from 100 kHz to 10^{-2} Hz with alternating current amplitude of 5 mV under open-circuit conditions. According to the analysis model proposed by Kuriyama et al. [26], an equivalent circuit for the alloy electrode was used and the parameters in the equivalent circuit were fitted using least-square method with ZVIEW electrochemical impedance software; I_0 is calculated from the following formulation ($I_0 = RT/FR_T$).

3. Result and Discussion

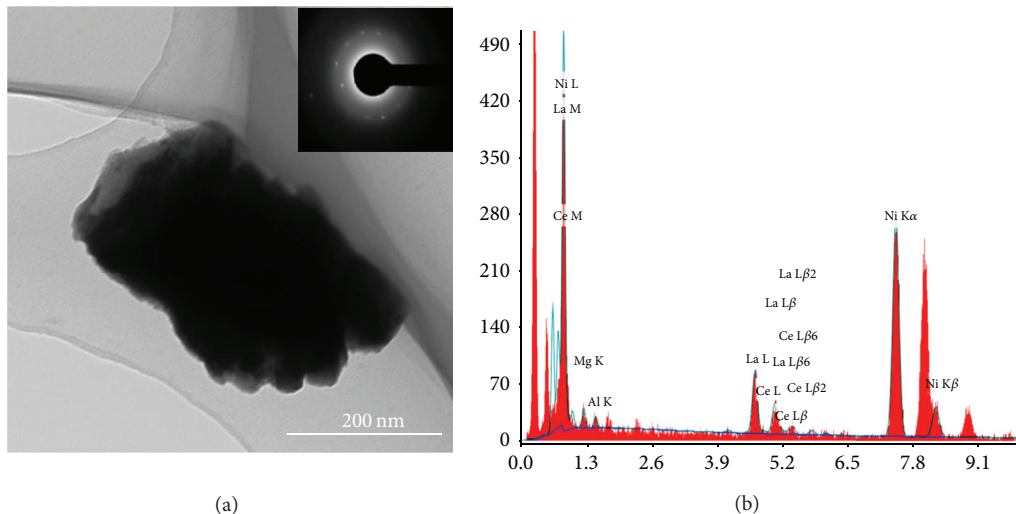
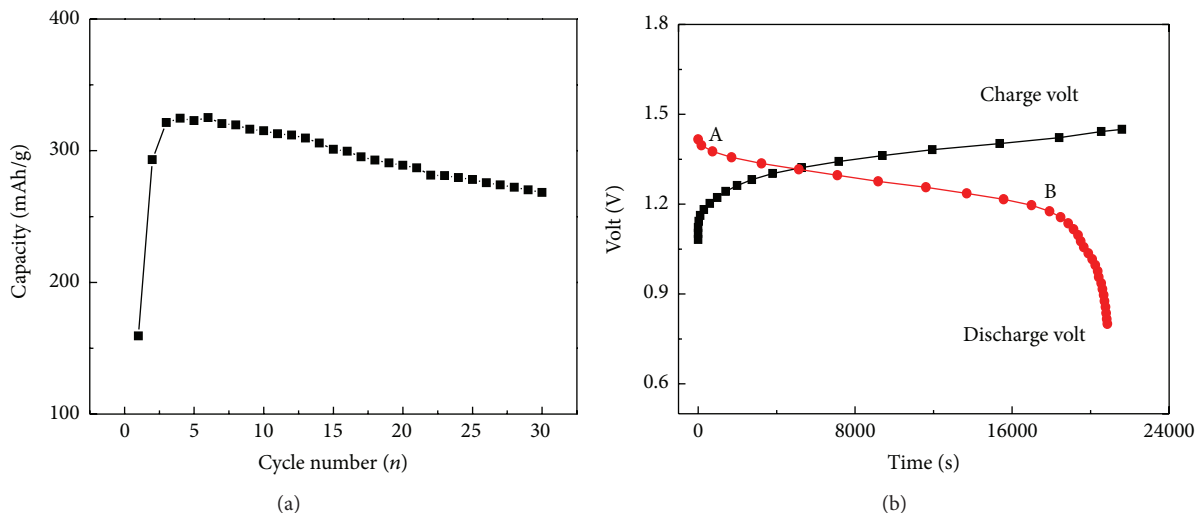
3.1. XRD. Figure 1 shows the XRD patterns of $\text{La}_{0.96}\text{Ce}_{0.04}\text{Mg}_{0.15}\text{Al}_{0.05}\text{Ni}_{2.8}$ alloy. It can be seen that the alloy consists of a $(\text{La}, \text{Mg})\text{Ni}_3$ phase with the rhombohedral PuNi₃-type structure (space group: $\bar{R}\bar{3}\text{m}$ (166)) and a LaNi₅ phase with the hexagonal CaCu₅-type structure (space group: $P6/m\bar{3}$ (191)). This result coincides well with that reported by Zhang et al. [21] and Liao et al. [15]: Al was helpful to the formation of LaNi₅ phase with CaCu₅ type in La-Mg-Ni hydrogen storage alloys, and also the content of Al decides the content of LaNi₅ phase. According to the literature, about 2% Al has been used to substitute for Ni in the La-Mg-Ni alloy in this paper to form PuNi₃-type structure and CaCu₅-type structure.

The lattice parameters of a , c , and the cell volume of LaNi₅ phase are 0.5012 nm, 0.3984 nm, and 86.7×10^{-3} nm³, respectively. Each one of those parameters is smaller than the relevant one of La-Mg-Al-Ni alloy [25] ($a = 0.5058$ nm, $b = 0.4042$ nm, cell volume = 89.5×10^{-3} nm³), respectively. According to the literature [22, 23], rare earth elements (such as Dy and Pr) were helpful to decrease the cell volume of LaNi₅ phase, as shown in Table 1. The cell volume of LaNi₅ phase without rare earth element was larger than 87×10^{-3} nm³, while it is smaller than 87×10^{-3} nm³ for the alloys with rare earth element. It should be pointed out that the smaller the cell volume of the main phase (LaNi₅ phase) would decrease the cell volume expansion rate ($\Delta V/V$) on hydriding, and it is favorable for the alloy to decrease pulverization.

3.2. TEM. Figure 2 shows the TEM and EDS micrographs of $\text{La}_{0.96}\text{Ce}_{0.04}\text{Mg}_{0.15}\text{Al}_{0.05}\text{Ni}_{2.8}$ electrode alloy. It is obvious that the alloy is composed of multicrystal. The lattice space d can be calculated from the following formulation ($d = \lambda L/r$), where L means the length of the camera (0.2 m), λ means the wavelength of the accelerated voltage (0.00370 nm), and r means the radius of the diffractive spot (0.593 cm). The result shows that the d is 0.187 nm.

The phase composition of the alloy has been semiquantitatively analyzed with EDS which is shown in Figure 2 and the results are shown in Table 2. It can be seen that electrode alloy is composed of La, Ce, Mg, Al, and Ni, and the content of Mg is 3.48% (atom), which coincide well with the designed composition of the electrode alloy.

3.3. Cycle Stability and Discharge Profile. The cycle stability of $\text{La}_{0.96}\text{Ce}_{0.04}\text{Mg}_{0.15}\text{Al}_{0.05}\text{Ni}_{2.8}$ alloy electrode is shown in Figure 3(a). The alloy electrode is gradually activated during

FIGURE 2: TEM and EDS $\text{La}_{0.96}\text{Ce}_{0.04}\text{Mg}_{0.15}\text{Al}_{0.05}\text{Ni}_{2.8}$ alloy.FIGURE 3: Discharge capacity and discharge profile for $\text{La}_{0.96}\text{Ce}_{0.04}\text{Mg}_{0.15}\text{Al}_{0.05}\text{Ni}_{2.8}$ alloy.

charge/discharge cycle process and reached maximum discharge capacity of 325 mAh g^{-1} at 4th cycles to be proved to have the higher electrochemical activity. According to the literature [21], Al was helpful to the formation of LaNi_5 phase in La-Mg-Ni hydrogen storage alloys, but the content of Al would lead to some decrease in discharge capacity. The result also shows that the discharge capacity at 30th cycles is 268 mAh g^{-1} , which is about 82.5% of the maximum discharge capacity (325 mAh g^{-1}), and implies that cycle stability of the alloy electrode is acceptable.

Figure 3(b) shows the typical discharge capacity-potential curves for $\text{La}_{0.96}\text{Ce}_{0.04}\text{Mg}_{0.15}\text{Al}_{0.05}\text{Ni}_{2.8}$ alloy electrode. It can be clearly seen that the alloy electrode has a wider discharge voltage plateau. It is about 4.5 h for the battery to hold the discharge voltage above 1.2 V with a wider discharge voltage plateau from 1.38 V to 1.20. It was reported by Iwakura et al. [27] that the curve of equilibrium potential-discharge capacity and the curve of P-C isotherm were rather

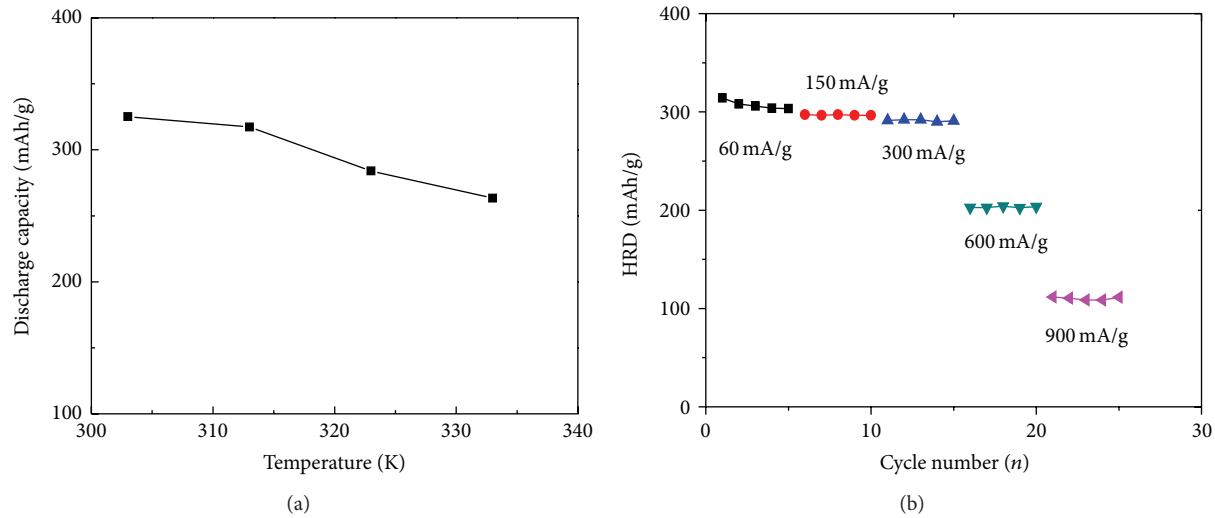
coordinate, especially for the tendency of the plateau region; that was to say, the plateau region of equilibrium potential for $\text{La}_{0.96}\text{Ce}_{0.04}\text{Mg}_{0.15}\text{Al}_{0.05}\text{Ni}_{2.8}$ alloy electrode has a good discharge characteristics.

3.4. Temperature Effect and High-Rate Dischargeability. Figure 4(a) shows the dependence of the discharge capacity of $\text{La}_{0.96}\text{Ce}_{0.04}\text{Mg}_{0.15}\text{Al}_{0.05}\text{Ni}_{2.8}$ alloy electrode on different temperatures. As can be seen in the figure, the discharge capacity of the alloy electrode is decreased as the temperature increased from 303 K to 333 K. For example, the discharge capacity of the alloy electrode is 284 mAh g^{-1} and 263 mAh g^{-1} at 323 K and at 333 K, respectively. It implies that the discharge capacity of $\text{La}_{0.96}\text{Ce}_{0.04}\text{Mg}_{0.15}\text{Al}_{0.05}\text{Ni}_{2.8}$ alloy electrode is sensitive to temperature within the temperature span.

HRD is an important property of electrode alloy used as negative electrode material in Ni-MH battery, especially

TABLE 1: Lattice constant and cell volume for La-RE-Mg-Al-Ni phydrogen storage alloys [22, 23, 25].

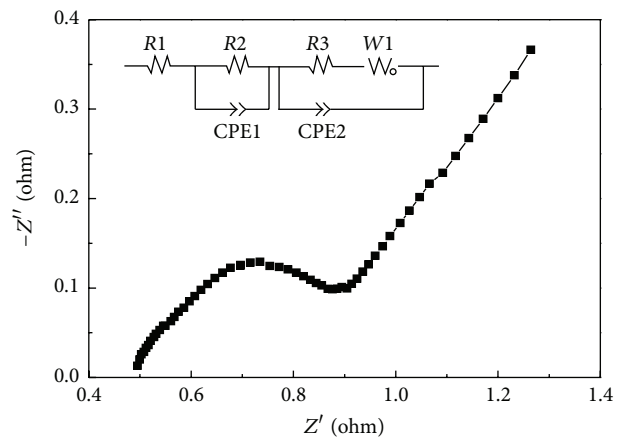
Alloy	a/nm	c/nm	$V \times 10^{-3}/\text{nm}^3$
La-Mg-Al-Ni	0.5058	0.4042	89.5
La-Ce-Mg-Al-Ni	0.5012	0.3984	86.7
(La _{1-x} Dy _x) _{0.8} Mg _{0.2} Ni _{3.4} Al _{0.1} ($x = 0$)	0.5024	0.3982	87.0
(La _{1-x} Dy _x) _{0.8} Mg _{0.2} Ni _{3.4} Al _{0.1} ($x = 0.05$)	0.5019	0.3978	86.8
(La _{1-x} Dy _x) _{0.8} Mg _{0.2} Ni _{3.4} Al _{0.1} ($x = 0.2$)	0.4993	0.3909	84.4
La _{0.8-x} Pr _x Mg _{0.2} Ni _{3.8} ($x = 0$)	0.5028	0.3989	87.3
La _{0.8-x} Pr _x Mg _{0.2} Ni _{3.8} ($x = 0.15$)	0.5012	0.3983	86.7
La _{0.8-x} Pr _x Mg _{0.2} Ni _{3.8} ($x = 0.40$)	0.4998	0.3982	86.1

FIGURE 4: Effect of temperature and discharge current density on the discharge capacity for La_{0.96}Ce_{0.04}Mg_{0.15}Al_{0.05}Ni_{2.8} alloy.TABLE 2: Phase composition and interplanar distance for La_{0.24}Ce_{0.01}Mg_{0.04}Al_{0.01}Ni_{0.70} alloy.

Composition (atom %)					d (nm)
La	Ce	Mg	Al	Ni	
23.93	1.29	3.48	1.47	69.82	0.187

used in electric vehicles. Figure 4(b) shows the relationship between the discharge capacity and the discharge current density of La_{0.96}Ce_{0.04}Mg_{0.15}Al_{0.05}Ni_{2.8} alloy electrode. It can be clearly seen that the alloy electrode has higher discharge capacity within the discharge current density span from 60 mA g⁻¹ to 300 mA g⁻¹, and the cycle stability of alloy electrode is accepted. It is worthy of notice that the discharge capacity of the alloy electrode is higher than 200 mAh g⁻¹ at 600 mA g⁻¹ and 100 mAh g⁻¹ at 900 mA g⁻¹, respectively. This characteristic of the alloy is crucial for it to be used as a negative electrode material of Ni-MH batteries.

3.5. EIS. Figure 5 shows the EIS of La_{0.96}Ce_{0.04}Mg_{0.15}Al_{0.05}Ni_{2.8} alloy electrode at 50% DOD. EIS has been used for determining R_T and I_0 to clarify the kinetic properties of dehydrating action at 303 K. According to the equivalent circuits [26], the large semicircle in the low-frequency region

FIGURE 5: EIS of La_{0.96}Ce_{0.04}Mg_{0.15}Al_{0.05}Ni_{2.8} alloy electrode at 50% DOD.

is attributed to the charge transfer resistance R_T on the alloy surface, and the fitted result shows that the R_T is 0.135 Ω. The exchange current density I_0 for the alloy electrode can be calculated by the following formulation: $I_0 = RT/FR_T$, where R , T , F , and R_T denote the gas constant, the absolute temperature, the Faraday constant, and charge transfer resistance on

TABLE 3: Self-discharge characteristics of $\text{La}_{0.96}\text{Ce}_{0.04}\text{Mg}_{0.15}\text{Al}_{0.05}\text{Ni}_{2.8}$ alloy electrode at 293 K.

Day	C_1/mAh^{-1}	C_2/mAhg^{-1}	C_3/mAhg^{-1}	C_1-C_3/mAhg^{-1}	C_3-C_2/mAhg^{-1}	Self-discharge rate/%
1	296.1	283.3	293.2	2.9	9.9	3.9
2	287.5	270.8	383.1	4.4	12.3	5.1
4	278.9	190.3	258.2	20.7	67.9	7.3

the alloy surface, respectively. The calculated result shows that I_0 is 1298 mA g^{-1} , which is much larger than that in V-based solid solution electrode alloy [28]. This may be responsible for the better high-rate dischargeability.

3.6. Self-Discharge. According to the literature [29], self-discharge of the hydrogen storage alloy can be divided into two parts, the reversible (C_3-C_2) and irreversible (C_1-C_3), respectively. The self-discharge rate of the alloy electrode can be calculated with $\{1 - 2C_2/(C_1 + C_3)\} \times 100\%$ day. C_1 , C_2 , and C_3 have been determined with the tested alloy electrode standing at open circuit for 1, 2, and 4 days, respectively, as shown in Table 3. The results indicate that the self-discharge rate of the alloy electrode is increased as the time standing increased from 1 day to 4 days, also, the reversible part (C_3-C_2) which due to desorption of hydrogen is larger than that of irreversible (C_1-C_3) part which was due to deterioration of the hydrogen storage alloy.

4. Conclusion

The structure and electrochemical properties of $\text{La}_{0.96}\text{Ce}_{0.04}\text{Mg}_{0.15}\text{Al}_{0.05}\text{Ni}_{2.8}$ alloy electrode have been studied. The conclusions can be drawn as follows.

- (1) The hydrogen storage alloy is consisted of a $(\text{La}, \text{Mg})\text{Ni}_3$ phase with the rhombohedral PuNi_3 -type structure and a LaNi_5 phase with the hexagonal CaCu_5 -type structure.
- (2) The maximum discharge capacity 325 mAh g^{-1} and cyclic stability 82.5% after 30 cycles are obtained; the discharge capacity is decreased as the temperature increased from 303 K to 333 K; the alloy electrode has higher discharge capacity within the discharge current density span from 60 mA g^{-1} to 300 mA g^{-1} .
- (3) The charge transfer resistance R_T on the alloy surface is 0.135Ω and the exchange current density I_0 is 1298 mA g^{-1} , respectively.
- (4) The self-discharge rate of the alloy electrode is increased as the time standing increases (increased), and also the reversible part (C_3-C_2) is larger than that of irreversible (C_1-C_3) part.

Conflict of Interests

The authors declare that they have no conflict of interests.

Acknowledgments

This work was supported by Ministry of Science and Technology of China (2011AA03A408), the Foundation of State Key Laboratory of Rare Earth Resources Utilization (RERU2013021), and Doctoral Foundation of Yanshan University (B330).

References

- [1] J. J. Liu, S. M. Han, Y. Li et al., "Phase structure and electrochemical characteristics of high-pressure-sintered La-Mg-Ni-based hydrogen storage alloys," *Electrochimica Acta*, vol. 111, pp. 18–24, 2013.
- [2] L. Zhang, S. M. Han, Y. Li et al., "Formation mechanism, phase structure and electrochemical properties of the La-Mg-Ni-based multiphase alloys by powder sintering LaNi_5 and LaMgNi_4 ," *International Journal of Hydrogen Energy*, vol. 38, no. 25, pp. 10431–10437, 2013.
- [3] J. L. Zhang, S. M. Han, Y. Li et al., "Effects of PuNi_3 and Ce_2Ni_7 -type phase abundance on electrochemical characteristics of La-Mg-Ni-based alloys," *Journal of Alloys and Compounds*, vol. 581, pp. 693–698, 2013.
- [4] C. C. Nwakwuo, T. Holm, R. V. Denys et al., "Effect of magnesium content and quenching rate on the phase structure and composition of rapidly solidified La_2MgNi_9 metal hydride battery electrode alloy," *Journal of Alloys and Compounds*, vol. 555, pp. 201–208, 2013.
- [5] Y. H. Zhang, Z. H. Hou, B. W. Li, H. P. Ren, G. F. Zhang, and D. L. Zhao, "An investigation on electrochemical hydrogen storage performances of the as-cast and -annealed $\text{La}_{0.8-x}\text{Sm}_x\text{Mg}_{0.2}\text{Ni}_{3.35}\text{Al}_{0.1}\text{Si}_{0.05}$ ($x = 0\text{--}0.4$) alloys," *Journal of Alloys and Compounds*, vol. 537, pp. 175–182, 2013.
- [6] B. P. Wang, Y. Z. Chen, and Y. N. Liu, "Structure and electrochemical properties of $(\text{La}_{1-x}\text{Dy}_x)_0.8\text{Mg}_{0.2}\text{Ni}_{3.4}\text{Al}_{0.1}$ ($x = 0.0\text{--}0.20$) hydrogen storage alloys," *International Journal of Hydrogen Energy*, vol. 37, no. 11, pp. 9082–9087, 2012.
- [7] H. X. Huang and K. L. Huang, "Effect of AB_5 alloy on electrochemical properties of $\text{Mm}_{0.80}\text{Mg}_{0.20}\text{Ni}_{2.56}\text{Co}_{0.50}\text{Mn}_{0.14}\text{Al}_{0.12}$ hydrogen storage alloy," *Powder Technology*, vol. 221, pp. 365–370, 2012.
- [8] X. P. Dong, L. Y. Yang, X. T. Li, Q. Wang, L. H. Ma, and Y. F. Lin, "Effect of substitution of aluminum for nickel on electrochemical properties of $\text{La}_{0.75}\text{Mg}_{0.25}\text{Ni}_{3.5-x}\text{Co}_{0.2}\text{Al}_x$ hydrogen storage alloys," *Journal of Rare Earths*, vol. 29, no. 2, pp. 143–149, 2011.
- [9] Y. H. Zhang, Y. Cai, C. Zhao, T. T. Zhai, G. F. Zhang, and D. L. Zhao, "Electrochemical performances of the as-melt $\text{La}_{0.75-x}\text{M}_x\text{Mg}_{0.25}\text{Ni}_{3.2}\text{Co}_{0.2}\text{Al}_{0.1}$ ($\text{M} = \text{Pr}, \text{Zr}, x = 0, 0.2$) alloys applied to Ni/metal hydride (MH) battery," *International Journal of Hydrogen Energy*, vol. 37, no. 19, pp. 14590–14597, 2012.
- [10] Y. Liu, Y. Cao, L. Huang, M. Gao, and H. Pan, "Rare earth-Mg-Ni-based hydrogen storage alloys as negative electrode materials for Ni/MH batteries," *Journal of Alloys and Compounds*, vol. 509, no. 3, pp. 675–686, 2011.

- [11] K. Kadir, T. Sakai, and I. Uehara, "Synthesis and structure determination of a new series of hydrogen storage alloys; RMg₂Ni₉ (R = La, Ce, Pr, Nd, Sm and Gd) built from MgNi₂ laves-type layers alternating with AB₅ layers," *Journal of Alloys and Compounds*, vol. 257, no. 1-2, pp. 115–121, 1997.
- [12] K. Kadir, N. Kuriyama, T. Sakai, I. Uehara, and L. Eriksson, "Structural investigation and hydrogen capacity of CaMg₂Ni₉: a new phase in the AB₂C₉ system isostructural with LaMg₂Ni₉," *Journal of Alloys and Compounds*, vol. 284, no. 1-2, pp. 145–154, 1999.
- [13] K. Kadir, T. Sakai, and I. Uehara, "Structural investigation and hydrogen storage capacity of LaMg₂Ni₉ and (La_{0.65}Ca_{0.35})(Mg_{1.32}Ca_{0.68})Ni₉ of the AB₂C₉ type structure," *Journal of Alloys and Compounds*, vol. 302, no. 1-2, pp. 112–117, 2000.
- [14] J. Chen, H. T. Takeshita, H. Tanaka et al., "Hydriding properties of LaNi₃ and CaNi₃ and their substitutes with PuNi₃-type structure," *Journal of Alloys and Compounds*, vol. 302, no. 1-2, pp. 304–313, 2000.
- [15] B. Liao, Y. Q. Lei, L. X. Chen, G. L. Lu, H. G. Pan, and Q. D. Wang, "The structural and electrochemical properties of La₂Mg(Ni_{0.8-x}Co_{0.2}Al_x)₉ (x = 0–0.03) hydrogen storage electrode alloys," *Journal of Alloys and Compounds*, vol. 415, no. 1-2, pp. 239–243, 2006.
- [16] B. Liao, Y. Q. Lei, L. X. Chen, G. L. Lu, H. G. Pan, and Q. D. Wang, "Effect of the La/Mg ratio on the structure and electrochemical properties of La_xMg_{3-x}Ni₉ (x = 1.6–2.2) hydrogen storage electrode alloys for nickel-metal hydride batteries," *Journal of Power Sources*, vol. 129, no. 2, pp. 358–367, 2004.
- [17] H. Miao, H. Pan, S. C. Zhang, N. Chen, R. Li, and M. X. Gao, "Influences of Co substitution and annealing treatment on the structure and electrochemical properties of hydrogen storage alloys La_{0.7}Mg_{0.3}Ni_{2.45-x}Co_{0.75+x}Mn_{0.1}Al_{0.2} (x = 0.00, 0.15, 0.30)," *International Journal of Hydrogen Energy*, vol. 32, no. 15, pp. 3387–3394, 2007.
- [18] H. G. Pan, Y. F. Liu, M. X. Gao, R. Li, and Y. Q. Lei, "Function of cobalt in the new type rare-earth Mg-based hydrogen storage electrode alloys," *Intermetallics*, vol. 13, no. 7, pp. 770–777, 2005.
- [19] B. Liao, Y. Q. Lei, L. X. Chen, G. L. Lu, H. G. Pan, and Q. D. Wang, "Effect of Co substitution for Ni on the structural and electrochemical properties of La₂Mg(Ni_{1-x}Co_x)₉ (x = 0.1–0.5) hydrogen storage electrode alloys," *Electrochimica Acta*, vol. 50, no. 4, pp. 1057–1063, 2004.
- [20] B. Liao, Y. Q. Lei, L. X. Chen, G. L. Lu, H. G. Pan, and Q. D. Wang, "The effect of Al substitution for Ni on the structure and electrochemical properties of AB₃-type La₂Mg(Ni_{1-x}Al_x)₉ (x = 0–0.05) alloys," *Journal of Alloys and Compounds*, vol. 404–406, pp. 665–668, 2005.
- [21] X.-Y. Zhang, Y.-C. Luo, D.-H. Wang, R.-X. Yan, Y. Zhang, and L. Kang, "A study on the structure and electrochemical properties of La_{0.67}Mg_{0.33}Ni_{3.0-x}Al_x (x = 0, 0.1, 0.2, 0.3) hydrogen storage alloys," *Journal of Functional Materials*, vol. 36, no. 7, pp. 1034–1040, 2005.
- [22] B. P. Wang, Y. Z. Chen, and Y. N. Liu, "Structure and electrochemical properties of (La_{1-x}Dy_x)_{0.8}Mg_{0.2}Ni_{3.4}Al_{0.1} (x = 0.0–0.20) hydrogen storage alloys," *International Journal of Hydrogen Energy*, vol. 37, no. 11, pp. 9082–9087, 2012.
- [23] J. B. Fan, A. Q. Deng, G. J. Xia, K. N. Qian, and Y. C. Luo, "Phase structure and electrochemical properties of the AB_{3.8}-type La-Mg-Ni system hydrogen storage alloys," *Rare Metal Materials and Engineering*, vol. 39, no. 12, pp. 2142–2146, 2010.
- [24] Y. Q. Qiao, M. S. Zhao, X. J. Zhu, and G. Cao, "Microstructure and some dynamic performances of Ti_{0.17}Zr_{0.08}V_{0.34}RE_{0.01}Cr_{0.1}Ni_{0.3}(RE = Ce, Dy) hydrogen storage electrode alloys," *International Journal of Hydrogen Energy*, vol. 32, no. 15, pp. 3427–3434, 2007.
- [25] H. Miao, H. Pan, S. Zhang, N. Chen, R. Li, and M. Gao, "Influences of Co substitution and annealing treatment on the structure and electrochemical properties of hydrogen storage alloys La_{0.7}Mg_{0.3}Ni_{2.45-x}Co_{0.75+x}Mn_{0.1}Al_{0.2} (x = 0.00, 0.15, 0.30)," *International Journal of Hydrogen Energy*, vol. 32, no. 15, pp. 3387–3394, 2007.
- [26] N. Kuriyama, T. Sakai, H. Miyamura, I. Uehara, H. Ishikawa, and T. Iwasaki, "Electrochemical impedance and deterioration behavior of metal hydride electrodes," *Journal of Alloys and Compounds*, vol. 202, no. 1-2, pp. 183–197, 1993.
- [27] C. Iwakura, T. Askahiko, H. Yoneyama, T. Sakai, K. Oguro, and H. Ishikawa, "Electrochemical characteristics of LaNi₅ system hydrogen-absorbing alloys as negative electrode materials for nickel-hydrogen batteries," *The Chemical Society of Japan*, vol. 8, pp. 1482–1488, 1988.
- [28] Y. Q. Qiao, M. S. Zhao, M. Y. Li, X. J. Zhu, and G. Y. Cao, "Microstructure and electrochemical performance of Ti_{0.17}Zr_{0.08}V_{0.34}Pd_{0.01}Cr_{0.1}Ni_{0.3} electrode alloy," *Scripta Materialia*, vol. 55, no. 3, pp. 279–282, 2006.
- [29] C. Iwakura, Y. Kajiya, H. Yoneyama, T. Saki, K. Oguro, and H. Ishikawa, "Self-discharge mechanism of nickel-hydrogen batteries using metal hydride anodes," *Journal of the Electrochemical Society*, vol. 136, no. 5, pp. 1351–1355, 1989.

Research Article

A Novel Absorbent of Nano-Fe Loaded Biomass Char and Its Enhanced Adsorption Capacity for Phosphate in Water

Hongguang Zhou, Zhenmao Jiang, and Shiqiang Wei

College of Resources and Environment, Southwest University, Chongqing Key Laboratory of Agricultural Resources and Environment, Key Laboratory of Eco-environments of Three Gorges Reservoir Region, Chongqing 400716, China

Correspondence should be addressed to Shiqiang Wei; sqwei@swu.edu.cn

Received 26 September 2013; Accepted 21 October 2013

Academic Editor: Tifeng Jiao

Copyright © 2013 Hongguang Zhou et al. This is an open access article distributed under the Creative Commons Attribution License, which permits unrestricted use, distribution, and reproduction in any medium, provided the original work is properly cited.

A novel composite adsorbent of Fe loaded biomass char (Fe-BC) was fabricated to treat phosphorus in water. Fe-BC was prepared by a procedure including metal complex anion incorporation and precipitation with the pyrolysis char of corn straw as supporting material. The abundant porous structures of the as-prepared sample can be easily observed from its scanning electron microscopy (SEM) images. Observations by X-ray diffraction (XRD) and X-ray photoelectron spectroscopy (XPS) analyses show that inorganic nanoiron oxides deposited in the composite could be amorphous hydrous iron oxide α -FeOOH. Adsorption of phosphate onto the Fe-BC composite and its precursor (BC) from aqueous solutions were investigated and discussed. The equilibrium adsorption data of phosphate was described by Langmuir and Freundlich models, and Langmuir isotherm was found to be better fitted than Freundlich isotherm. The maximum phosphate adsorption capacity for phosphate of Fe-BC was as high as 35.43 mg/g, approximately 2.3 times of BC at 25°C. The adsorption kinetics data were better fitted by pseudo-second-order model and intraparticle diffusion model, indicating that the adsorption process was complex. The Fe-BC composite has been proved as an effective adsorbent of phosphate from aqueous solutions owing to its unique porous structures and the greater Lewis basicity of the α -FeOOH.

1. Introduction

Phosphorus is considered as the main culprit of lake eutrophication [1]. Excess phosphorus will stimulate the algal blooms, causing deterioration of water quality [2]. In recent years, human activities dramatically increased the loads of phosphate in environment and its cycling rate on Earth, such as the production and application of a plenty of detergents, agricultural pesticides, and fertilizers [3]. The increased amount of phosphorus in water bodies poses greater potentials to the occurring of eutrophication. It has been reported that the red tide may occur at concentration of phosphorus higher than 0.03 mg/L in the lake (sea) [4].

Municipal wastewater may contain variety concentrations of phosphate ranging from 4 to 15 mg-P/L, and industrial wastewater (such as detergent manufacturing) may contain phosphate levels well in excess of 10 mg-P/L [5]. Hence high effective methods for the removal of phosphate from wastewater need to be established. Traditional

biological treatment of phosphorus has been proved to be highly variable due to its hard operation conditions [6]; thus discharge limits of phosphate were hardly matched depending only on this technology regardless of its high cost. Chemical precipitation technology has been wildly used in phosphate removal, usually with salts of iron (such as ferric chloride) [7–9], aluminum [10, 11], or lime [12]. However, the difficulties of excessive sludge handling and cost of added chemical materials would hinder its widespread application. Other effective phosphorus removal techniques such as ion exchange and electrodialysis also encountered difficulties of complicated management and high cost. Adsorption has been regarded as one of the most effective and economical methods for the removal of phosphorus. The key to the success of the method depends on the selection of adsorbent with high adsorption capacity. Numerous studies have been conducted for this purpose, such as activated alumina [4, 13], metal oxide hydroxides [14–21], hydrotalcite [22], palygorskite [23, 24], zeolite [13, 25–27], slag [28–31] and layered double hydroxides

[32–36], as well as some waste materials such as red mud [37, 38], fly ash [39, 40], activated carbon [41], modified wheat residues [42, 43], and peat [44].

Metal oxides are well known for their industrial applications as adsorbents, catalysts, and catalyst supports [45]. Hydrous iron oxides performance is highlighted in phosphate removal, and their adsorption capacity of phosphorus can reach up to 17 mg-P/g [21]. This is mainly attributed to the formation of a stable bidentate ligand between ion oxides and phosphate. In particular, with the rapid development of nanotechnology, these kinds of metal oxide hydroxides have been prepared in nanoscale size by some researchers (Pan et al. 2009) [46]. Inorganic nanosize adsorbents showed high adsorption capacity due to their surface effect and the small size effect brought by the miniaturization of the particle size. However, conventional nanosized powder adsorbent has intrinsic drawback due to the difficulties of sedimentation and separation in such a slurry type system. Many efforts had been made to structure inorganic or organic materials with specific size, aperture, and morphology to overcome this limitation and extend its environmental applications, such as microspheres [47]. Precursor immersion-surface deposition method is another useful way to solve these problems; nanosize materials were well diffused into the precursor and then fixed by changing its chemical speciation.

There are various kinds of materials which can be used as precursor. Biomass char (BC) was considered as one of the best for its large surface areas, richness of inherent porous structures, and low cost. Biomass char can be obtained from biomass waste easily. Biomass wastes, derived from plants, are the most widely available renewable resource [48]. However, improper disposal of the increasing quantities of biomass waste may lead to various environmental issues. Agriculture produces large amount of biomass waste; for example, the annual production of corn straw reached about 0.22 billion tons only in China in 2009 [49], most of which were burnt directly outside in the field, causing atmospheric pollution, such as increased concentration of PM2.5, enhanced carbon emission, and CO₂ concentration. The pyrolysis technology of biomass waste for bioenergy production had been considered as a promising method with higher energy conversion efficiency [50]. Recently, biomass waste pyrolysis for fuel gas or biooil also aroused some attention [51, 52].

As a byproduct of biomass waste pyrolysis, biomass char is only about 10–40% of the total production [53]. BC deriving from biomass waste pyrolysis has relatively high fixed-carbon content and inherent porous structures. It has been reported that BC obtained from biomass pyrolysis at 673–873 K has a surface area ranging from 80 to 450 m²/g [43–57]. Thus BC could be a potential adsorbent for the removal of pollutants from water. Some studies have showed that biomass char could effectively adsorb many kinds of cation [53, 56] and anion [55–57], including phosphate anion. In order to make use of the advantages of abundant biomass based BC and the high adsorptive capacity of nanohydrous iron oxides, a novel composite adsorbent has been fabricated following the procedure of incorporation of hydrous iron oxides nanoparticles into the biochar from the pyrolysis

of corn straw. The basic physicochemical properties of the composite and its precursor were characterized and their performances on phosphate adsorption were investigated. Adsorption isotherms and the kinetics of phosphate adsorption on the composite adsorbents were compared with its precursor and some similar absorbents from literature; the results show that the synthesized Fe-BC is a promising adsorbent for phosphate with remarkably high adsorption capacity.

2. Experimental

2.1. Materials and Methods. The raw biomass material was corn straw, a common agricultural waste, obtained from the countryside in Pengshui, Chongqing Province, China. Fresh corn straw was air-dried, cut into 1–4 cm small pieces, washed several times with deionized water, dried in a furnace at 333 K for 24 h, and then being sieved to the particle diameters 1 mm after grated for pyrolysis. The phosphate solution was prepared by dissolving potassium dihydrogen phosphate (KH₂PO₄) in deionized water. All chemicals used were of analytical grade.

2.1.1. Pyrolysis Experiments. The biochar samples were obtained by pyrolysis experiments, which were carried out in a packed bed reactor in flowing nitrogen atmosphere with a heating rate of 5°C/min. The final temperature was kept at 773 K and the solid residence time was about one hour.

2.1.2. Preparation of Nano-Fe Loaded Biochar. There are some basic groups on the BC as well as some acidic functional groups, which provide different adsorption active sites. The acidic functional groups may be more dominant than the basic groups on BC. In our preliminary experiment, the mass of Fe loaded on the composite with FeCl₄⁻ is 3.7 times higher than the FeCl₃. BC was weighed and immersed into 1 mol/L FeCl₄⁻ aqueous solution (ratio of solid/solution is 1: 20) at pH 2.0 under continuous stirring at room temperature for 24 h. Then it was filtered by a 0.45 μm microfiltration membrane to collect the upside solid and washed with deionized water until the filtrate becomes clear. The solid sample was transferred into a saturated NaCl solution, and the pH of the solution was maintained at 12.0 by adding 0.1 M NaOH solutions. During this process it was stirred by mixer, and the mixing time lasts for 30 minutes. After that, the sample was filtered off, washed thoroughly three times with deionized water, and then dried in a vacuum oven with a -0.05 Kpa vacuum at 60°C for 24 h. The dried power was kept in a drier to make sure it was totally dried. The amount of Fe(III) loaded onto BC was then measured using atomic absorption spectroscopy (AAS) method [58].

2.2. Characterization Methods. The specific surface area of obtained biomass char (BC) and Fe loaded BC was analyzed by nitrogen adsorption using the Brunauer-Eett-Teller (BET) method with a Micromeritics ASAP-2010C automatic analyzer (Micromeritics Col Inc., Australia) at the temperature of 77 K. Also, the char was also observed using Scanning

Electron microscopy (SEM) analysis by SEM-EDS (S-3400N HITACHI Japan). X-ray powder diffraction (XRD) experiments were performed on a D/max-3B diffractometer with Cu K α irradiation at a scan rate of $0.02^\circ 2\theta s^{-1}$, to determine the identity of any phase present and its crystallite size. The composites were vacuum-dried at $30^\circ C$ before characterization and ground for SEM and XRD analysis. XPS spectra of the Fe-BC adsorbent before and after adsorption were performed by an X-ray photoelectron spectroscopy (Kratos AXIS Ultra, UK) with the monochromatic Al K α X-ray radiation (1486.7 eV). The wide scans were conducted from 0 to 1400 eV with pass energy of 160 eV. The high resolution scans were conducted according to the peak being examined with pass energy of 40 eV. The energy scale of the XPS spectra was calibrated with graphitic carbon as the reference at a binding energy of 284.8 eV due to the surface contamination. The XPS spectra peaks of Fe 2s were fitted using the XPS peak software.

2.3. Kinetic Adsorption Experiments. Simulation phosphate solutions were used throughout the adsorption tests. Initially, a stock solution was prepared by dissolving a certain amount of analytically pure KH₂PO₄ in deionized water. For adsorption experiments, the phosphate solutions with concentrations in the range of 1–100 mg/L were prepared by successive dilution of the stock solution with deionized water at room temperature. The supernatant solution was separated from the adsorbent by microfiltration membrane. Phosphate concentration in the supernatant was estimated spectrophotometrically by the molybdenum blue method; absorbance at 700 nm was monitored by UV-vis spectrophotometer.

Kinetic studies were carried out to establish the effect of contact time on the adsorption process and to quantify the adsorption rate. For kinetics adsorption experiments, each 0.05 g of adsorbents (BC, Fe-BC) was added into a series of flasks containing 50 mL phosphate solution (20 mg-P/L), separately. The initial pH of the solution was maintained at 3.0 by adding 0.1 M NaOH or 0.1 M HCl solutions. The flasks were placed in a thermostatic shaker at $25^\circ C$. At given time, each one of the flasks was taken out and immediately filtered by a 0.45 μ m microfiltration membrane to collect the filtrate and then the concentration of residual phosphate in the filtrate was determined by the method mentioned above.

2.4. Equilibrium Adsorption Experiments. For the equilibrium adsorption experiments, each 0.05 g of adsorbents was added into a series of flasks containing 50 mL solution with phosphate concentration ranging from 1 to 100 mg-P/L. The flasks were then sealed and put in a thermostatic shaker at various constant temperatures and shaken at the 120 rpm for 240 min. Then the solution in the flasks was filtered and the phosphate concentration in the filtrate was measured. The phosphate absorbed at equilibrium was calculated using the following equation:

$$Q = \frac{V(C_0 - C_e)}{m}, \quad (1)$$

where Q (mg/g) is the amount of phosphate adsorbed, V (mL) is the volume of the solution, C_0 and C_e (mg/L) are the initial

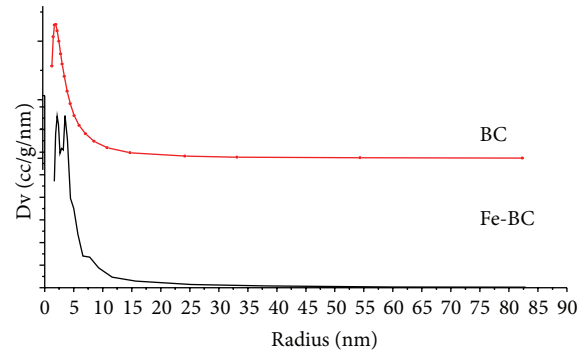


FIGURE 1: The pore size distribution of samples BC and Fe-BC.

and equilibrium concentrations of phosphate, respectively, and m (g) is the weight of adsorbent.

3. Results and Discussion

3.1. Characterization of BC Samples. The BC sample with very high BET surface area ($434.7 \text{ m}^2/\text{g}$) and narrow pore size distribution (Figure 1), its average pore diameter is about 3.5 nm. It may provide very good adsorption capacity and modified potentialities. The loaded treatment may decrease the BET surface area of composite which is only $18.71 \text{ m}^2/\text{g}$. As suggested, the preloaded nano-Fe particles would block some inner pores or make the pores narrower. Similar result was also reported by Shi concerning the effect of Fe(III) loadings on the pore volume and surface area of the resulting hybrid [58]. The mass of Fe in hybrid treated by FeCl₄⁻ is about 4.53%. And the curve of average pore diameter performs a bimodal distribution, which means that the loaded treatment changed the structure and property. Incorporation of nano-Fe into BC also altered its surface and textural morphology as shown by the SEM images in Figure 2. With different magnification ($\times 600$ and $\times 3000$), different surface and structure can be seen clearly. The more irregular fragmented structure and pore structure of BC sample may contribute to its high surface area and pore volume.

As shown in Figure 3, there are no obvious peaks in the XRD patterns which indicated that the iron oxides in the samples existed as amorphous state.

3.2. Adsorption Kinetics. The adsorption kinetics curves of phosphate adsorption on BC and Fe-BC are shown in Figure 4, which may reflect the differences of adsorption rates and their rate control steps. The adsorption curves of BC and Fe-BC go as the same tendency; they rise sharply at the first 5 min and tend to be gentle after 60 and 120 min, respectively, which means that the adsorption speed is not constant during the whole process and the adsorption equilibrium time on BC is shorter than that on Fe-BC. But the y value of BC at the equilibrium condition is lower than that of Fe-BC, indicating that the adsorption capacity of BC is lower than Fe-BC.

Four kinetic models were adopted to describe the adsorption process. The pseudo-first-order kinetic model has been widely used to predict sorption kinetics. The adsorption rate

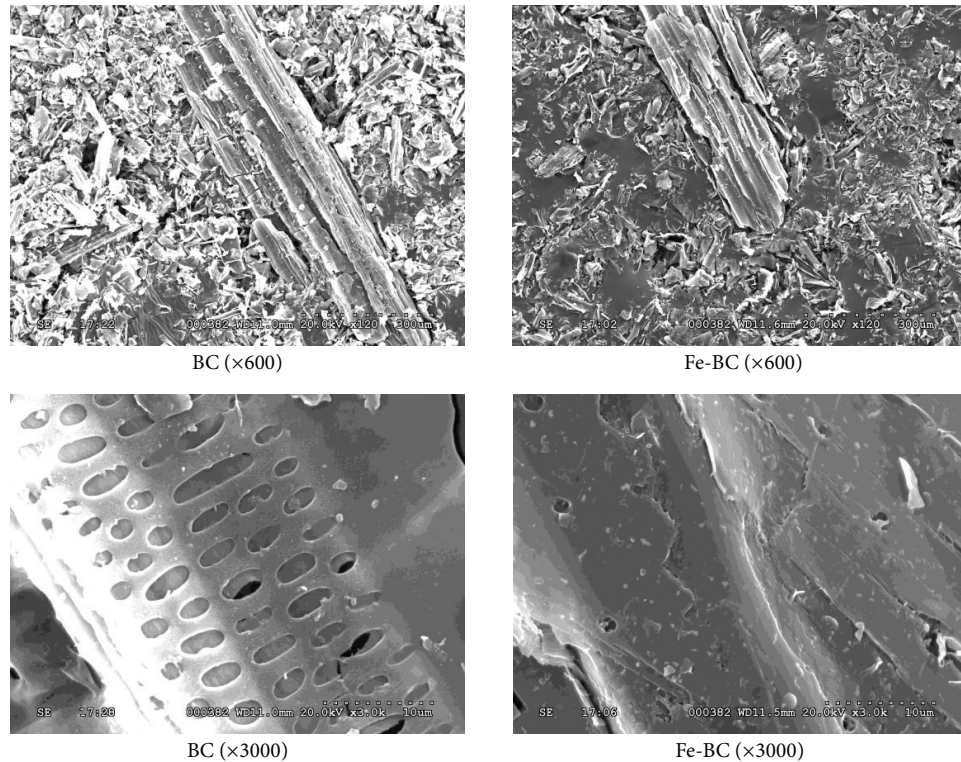


FIGURE 2: SEM images of samples BC and Fe-BC.

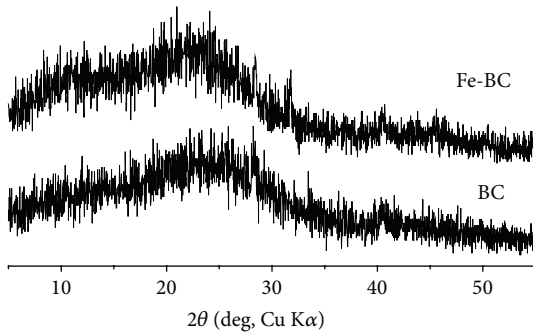


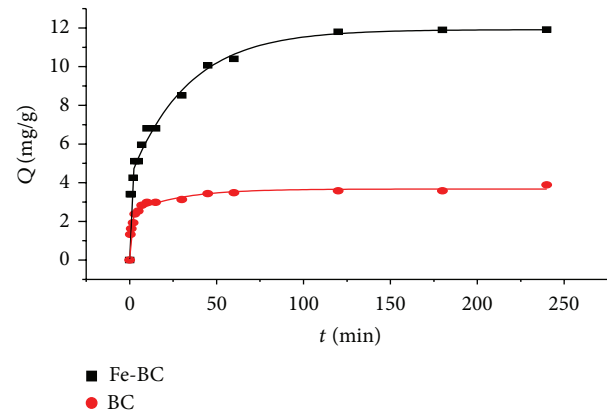
FIGURE 3: XRD diffraction pattern of BC and Fe-BC.

is proportional to the concentration of adsorbate. It can be used to describe the simple surface physical absorption. The model is defined as

$$\ln(Q_e - Q_t) = \ln Q_e - k_1 t. \quad (2)$$

The pseudo-second-order equation assumed that the adsorption mechanism was dominant by chemisorption. The adsorption rate is proportional to square of adsorbate concentration. The pseudo-second-order equation can be expressed as

$$\frac{t}{Q_t} = \frac{1}{k_2 Q_e^2} + \frac{t}{Q_e}, \quad (3)$$

FIGURE 4: The variation of adsorption capacity with adsorption time for phosphate on samples BC and Fe-BC ($T = 25^\circ\text{C}$; adsorbent dose = 1 g/L; phosphate concentration = 20 mg/L, and pH = 3).

where k_1 (min^{-1}) and k_2 are the pseudo-first-order rate constant and the pseudo-second-order rate constant, respectively, reflecting the adsorption rate change along with the concentration change. The results are showed in Table 1.

Compared with pseudo-second-order kinetic, the experimental $Q_{e,\text{exp}}$ values of first-order kinetic do not well agree with the calculated $Q_{e,\text{cal}}$ values obtained from the curve plots, suggesting that the adsorption process is not maintained by simple surface physical absorption, and some other adsorption mechanisms were involved.

TABLE 1: Pseudo-first-order and Pseudo-second-order adsorption kinetic constants of samples BC and Fe-BC.

Samples	$Q_{e,exp}$ (mg/g)	Pseudo-first-order model				Pseudo-second-order model			
		$Q_{e,cal}$ (mg/g)	k_1 (min^{-1})	R^2	S.D. (%)	$Q_{e,cal}$ (mg/g)	k_2 ($\text{gmg}^{-1}\text{min}^{-1}$)	R^2	S.D. (%)
BC	3.58	3.34	0.508	0.905	16.22	3.52	0.211	0.967	9.51
Fe-BC	11.94	10.58	0.135	0.813	32.30	11.31	0.019	0.905	24.24

TABLE 2: Liquid film diffusion model and Intraparticle diffusion constants for phosphate.

Samples	$Q_{e,exp}$ (mg/g)	liquid film diffusion model				Intraparticle diffusion model			
		$Q_{e,cal}$ (mg/g)	R (min^{-1})	R^2	S.D. (%)	C	K_3 ($\text{mg/gmin}^{1/2}$)	R^2	S.D. (%)
C	3.58	3.34	0.508	0.905	16.22	1.70	0.271	0.770	25.52
BC-Fe	11.94	10.58	0.135	0.813	32.30	2.93	1.025	0.975	20.56

Generally, the process of the adsorbate adsorbed by adsorbent can be divided into four steps: firstly, adsorbate molecules transferred to the nearby adsorbent from solution; secondly, adsorbate molecules diffusion through the liquid film up to the surface of absorbent particles, this step usually was called external diffusion or mass transfer; thirdly, adsorbate molecules diffused through the absorbent particles and reached the inner side; this step is usually called intraparticle diffusion or diffusion; fourthly, adsorbate molecules were attracted at the active sites in the interior of the particles. Step one and four were not the rate-controlling steps due to their happening so fast. And the kinetics of the adsorption will be governed either by diffusion or by a mass transfer mechanism depending on which of the above steps is the slowest. Hence, in this study, two models were investigated to find out the rate-controlling step of the adsorption process.

Intraparticle diffusion model is based on the theory proposed by Weber and Morris [60]. It was used to identify the diffusion mechanism. According to this theory,

$$Q_t = k_3 \sqrt{t} + C, \quad (4)$$

where k_3 is the intra-particular diffusion rate constant ($\text{mg g}^{-1} \text{min}^{-1/2}$). If intraparticle diffusion is rate-limited, the plots of adsorbates uptake Q_t versus the square root of time ($t^{1/2}$) would result in a linear relationship. k_3 and C values can be obtained from these plots.

The result of Q_t versus $t^{1/2}$ is shown in Table 2. In diffusion model, the first step is the mass transfer of adsorbates molecule from the bulk solution to the adsorbent surface and second stage is the intraparticle diffusion on samples.

Liquid film diffusion model is based on the theory proposed by Boyd et al. [61]. It was also used to identify the diffusion mechanism and find out which step is the rate-controlling step. According to this theory,

$$\log(1 - F) = \frac{R}{2.303} t, \quad (5)$$

where F represents the degree of exchange of adsorbate which was adsorbed onto the particles and can be described as Q_t/Q_e , R is a constant about the particle characters and it can be described as $R = 3D^l/r_0\delta k$, D^l is the diffusion constant in the liquid, r_0 is the radius of spherical adsorbent, δ is the thickness of liquid film, and k is distribution efficient.

Normalized standard deviation (S.D.) (%) is used to find the most applicable model that could describe the kinetic study of adsorption of phosphate on samples A and B. The normalized standard deviation (S.D.) (%) was calculated using the following equation [62]:

$$\text{S.D. (\%)} = \sqrt{\sum \left\{ \frac{[(Q_{t,exp} - Q_{t,cal})/Q_{t,exp}]^2}{N-1} \right\}}, \quad (6)$$

where N is the number of data points, $Q_{t,exp}$ is the experimental values, and $Q_{t,cal}$ is the calculated value by the above four models, respectively. According to the values of S.D. (%) given in Tables 1 and 2, it is clear that pseudo-second-order equation is better in describing the adsorption kinetics of phosphate by samples BC and Fe-BC. And Fe-BC sample is better fitting intraparticle diffusion model than liquid film diffusion model while the carrier material BC shows the opposite result. However, the difference of S.D. values for liquid film diffusion model and Intra-particle diffusion model was not significant, indicating that both intra-particle diffusion and mass transfer were the rate controlling steps.

3.3. Adsorption Isotherm Models. Equilibrium adsorption curves of BC and Fe-BC are showed in Figure 5. With the concentration of phosphate increasing, the equilibrium adsorption capacity Q_e increased at the low concentration level and remained unchanged when the concentration is higher than a certain value.

Langmuir and Freundlich isotherms were applied to describe the relationship between the amount of phosphate absorbed on adsorbent and its equilibrium concentration in aqueous solution. The Langmuir and Freundlich equations were listed in Table 3, where k_l (L/mg) is Langmuir constants related to adsorption capacity and energy of adsorption and k_f (mg/g) and n are the constants of the Freundlich isotherm that measure the adsorption capacity and intensity of adsorption, respectively. In Freundlich equation, $1/n$ values between 0 and 1 indicated a good adsorption.

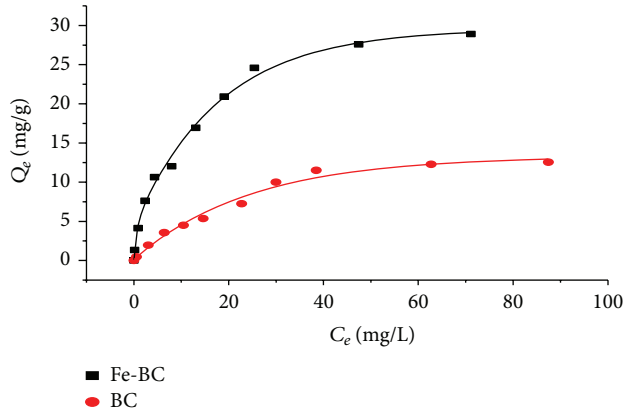
The equilibrium adsorption data was analyzed using the Langmuir and Freundlich models. The estimated adsorption constants with corresponding correlation coefficients (R^2) are summarized in Table 3. The results indicate that both models can be used to describe the adsorption isotherms, while the

TABLE 3: Adsorption isotherm parameters of samples BC and Fe-BC.

Samples	Langmuir isotherm model $C_e/Q_e = 1/(Q_{\max}k_l) + C_e/Q_{\max}$			Freundlich isotherm model $\lg Q_e = \lg k_f + n^{-1}\lg C_e$		
	Q_{\max} (mg/g)	k_l (L/mg)	R^2	k_f (mg/g) $(L/mg)^{1/n}$	n^{-1}	R^2
BC	15.44	0.038	0.978	1.628	0.484	0.943
Fe-BC	35.43	0.091	0.985	6.045	0.388	0.968

TABLE 4: Phosphate adsorption parameters of different waste materials.

Materials	Adsorption capacity (mg/g)	k_l	k_f	n^{-1}	Reference
Red mud	0.58	146.39	0.632	4.281	[38]
Wheat straw	2.81	0.008	0.044	1.087	[43]
ZnCl ₂ -activated coir pith carbon	5.1	0.282	1.482	0.330	[41]
Zeolite	6.45	0.139	0.91	0.437	[59]
Peat	8.91	0.033	0.713	2.042	[44]
Nano Fe loaded BC	35.43	0.091	6.045	0.388	This study

FIGURE 5: The adsorption capacity of phosphate onto samples BC and Fe-BC at variety initial concentration ($T = 25^\circ\text{C}$, adsorbent dose = 1 g/L, and pH = 3).

Langmuir model provides a better fitness than Freundlich model for phosphorus adsorption on BC absorbents. The maximum adsorption capacity obtained from Langmuir equation was 15.44 mg/g and 35.43 mg/g for BC and Fe-BC, respectively, indicating that incorporation of nanohydrous iron oxides into the biochar greatly increased the adsorption capacity for phosphate.

As shown in Figure 6, the XPS patterns indicated that the iron oxides mainly exist in FeOOH forms. In addition, from XRD patterns there is no fixed crystal, confirming that the iron oxides might be amorphous α -FeOOH, which is more active than other species [16]. Several signals of the iron oxide shell (peaks at 711.5 and 724.3 eV [63] for FeOOH) were observed. After adsorption, the banding energy of iron oxides is lower than before, and a new peak appeared at 712.8 eV [64], suggesting that a kind of iron oxide was formed during the adsorption process.

The significant increase of adsorption capacity for Fe-BC is probably due to the greater Lewis basicity of the FeOOH incorporated. The pH of the solution was maintained at 3.0,

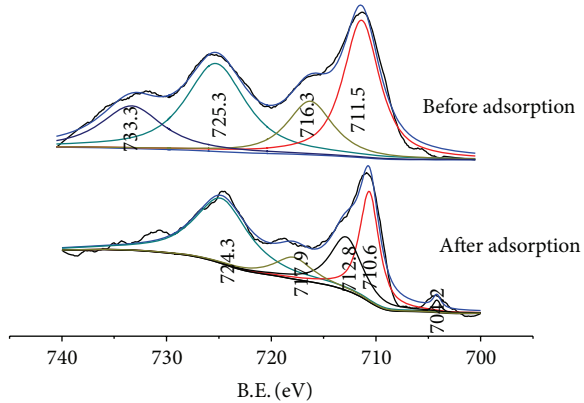


FIGURE 6: Fe 2s XPS spectra of BC-Fe before and after phosphate adsorption.

which was lower than the isoelectric point of FeOOH (8.7) [65], causing positively charged FeOOH surface. Therefore, it is not surprising that negative phosphate molecules are easily adsorbed on the Fe-BC surface at a low pH range due to strong electrostatic attraction between phosphate and FeOOH.

To compare the phosphate adsorption capacity of the synthesized composite in this study, the phosphate adsorption parameters of several other waste materials at similar conditions are cited from literature as shown in Table 4. It can be seen that the phosphate adsorption capacity of Fe-BC was fairly large and its adsorption rate and intensity are higher than most of other materials. Thus, the Fe-BC was a potentially adsorbent to remove phosphate from waste water for its high adsorption capacity and rate.

4. Conclusions

The findings of this work indicated that the new iron-containing BC material Fe-BC had great adsorption of phosphate ions. Adsorption fitted better to Langmuir isotherms

than to Freundlich isotherm and the maximum phosphate adsorption for Fe-BC was found to be 35.43 mg/g at 25°C which is approximately 2.3 times of BC. Kinetic data were well fit to a pseudo-second-order model and intraparticle diffusion model. The as-prepared Fe-BC is found to be effective adsorbent for the removal of phosphate from aqueous solutions because of its unique hierarchical porous structure and the greater Lewis basicity of the α -FeOOH. This indicated that it is a potential adsorbent material for water treatment.

Acknowledgments

This research is supported by the National Major Science and Technology Projects for Water Pollution Control and Management (Grant no. 2012ZX07104-003), the Natural Scientific Foundation of China (Grants nos. 21207110 and 41171198), China Postdoctoral Science Foundation Funded Project (Grant no. 2013M540691), and the Fundamental Research Funds for the Central Universities (Grant no. XDJK2014C102).

References

- [1] C. L. Schelske, "Eutrophication: focus on phosphorus," *Science*, vol. 324, no. 5928, p. 722, 2009.
- [2] V. H. Smith, G. D. Tilman, and J. C. Nekola, "Eutrophication: impacts of excess nutrient inputs on freshwater, marine, and terrestrial ecosystems," *Environmental Pollution*, vol. 100, no. 1-3, pp. 179–196, 1999.
- [3] P. J. A. Withers and H. P. Jarvie, "Delivery and cycling of phosphorus in rivers: a review," *Science of the Total Environment*, vol. 400, no. 1-3, pp. 379–395, 2008.
- [4] S. Tanada, M. Kabayama, N. Kawasaki et al., "Removal of phosphate by aluminum oxide hydroxide," *Journal of Colloid and Interface Science*, vol. 257, no. 1, pp. 135–140, 2003.
- [5] G. Akay, B. Keskinler, A. Çakici, and U. Danis, "Phosphate removal from water by red mud using crossflow microfiltration," *Water Research*, vol. 32, no. 3, pp. 717–726, 1998.
- [6] G. Tchobanoglou and F. L. Burton, *Wastewater Engineering*, McGraw-Hill, 1991.
- [7] R. L. McLaughlin and I. D. Brindle, "A laboratory-scale investigation into the use of powdered iron for in situ removal of phosphorus from treated sewage effluent with constructed wetlands," *Water Quality Research Journal of Canada*, vol. 36, no. 4, pp. 759–779, 2001.
- [8] Y. Zhou, X.-H. Xing, Z. Liu et al., "Enhanced coagulation of ferric chloride aided by tannic acid for phosphorus removal from wastewater," *Chemosphere*, vol. 72, no. 2, pp. 290–298, 2008.
- [9] N. Boujelben, J. Bouzid, Z. Elouear, M. Feki, F. Jamoussi, and A. Montiel, "Phosphorus removal from aqueous solution using iron coated natural and engineered sorbents," *Journal of Hazardous Materials*, vol. 151, no. 1, pp. 103–110, 2008.
- [10] G. G. Timby, T. C. Danieli, R. W. McNew, and P. A. Moore Jr., "Polymer type and aluminum chloride affect screened solids and phosphorus removal from liquid dairy manure," *Applied Engineering in Agriculture*, vol. 20, no. 1, pp. 57–64, 2004.
- [11] G. M. Ayoub, B. Koopman, and N. Pandya, "Iron and aluminum hydroxy (oxide) coated filter media for low-concentration phosphorus removal," *Water Environment Research*, vol. 73, no. 4, pp. 478–485, 2001.
- [12] D. Seyhan and A. Erdinclar, "Effect of lime stabilisation of enhanced biological phosphorus removal sludges on the phosphorus availability to plants," *Water Science and Technology*, vol. 48, no. 1, pp. 155–162, 2003.
- [13] J.-W. Choi, S.-Y. Lee, S.-H. Lee, K.-B. Lee, D.-J. Kim, and S.-W. Hong, "Adsorption of Phosphate by amino-functionalized and co-condensed SBA-15," *Water, Air and Soil Pollution*, vol. 223, no. 5, pp. 2551–2562, 2012.
- [14] A. Genz, A. Kornmüller, and M. Jekel, "Advanced phosphorus removal from membrane filtrates by adsorption on activated aluminium oxide and granulated ferric hydroxide," *Water Research*, vol. 38, no. 16, pp. 3523–3530, 2004.
- [15] Y. Seida and Y. Nakano, "Removal of phosphate by layered double hydroxides containing iron," *Water Research*, vol. 36, no. 5, pp. 1306–1312, 2002.
- [16] R. Chitrakar, S. Tezuka, A. Sonoda, K. Sakane, K. Ooi, and T. Hirotsu, "Phosphate adsorption on synthetic goethite and akaganeite," *Journal of Colloid and Interface Science*, vol. 298, no. 2, pp. 602–608, 2006.
- [17] L. A. Rodrigues and M. L. C. P. da Silva, "Thermodynamic and kinetic investigations of phosphate adsorption onto hydrous niobium oxide prepared by homogeneous solution method," *Desalination*, vol. 263, no. 1-3, pp. 29–35, 2010.
- [18] L. A. Rodrigues and M. L. C. P. da Silva, "An investigation of phosphate adsorption from aqueous solution onto hydrous niobium oxide prepared by co-precipitation method," *Colloids and Surfaces A*, vol. 334, no. 1-3, pp. 191–196, 2009.
- [19] X. Yang, D. Wang, Z. Sun, and H. Tang, "Adsorption of phosphate at the aluminum (hydr)oxides-water interface: role of the surface acid-base properties," *Colloids and Surfaces A*, vol. 297, no. 1-3, pp. 84–90, 2007.
- [20] B. Nowack and A. T. Stone, "Competitive adsorption of phosphate and phosphonates onto goethite," *Water Research*, vol. 40, no. 11, pp. 2201–2209, 2006.
- [21] R. Chitrakar, S. Tezuka, A. Sonoda, K. Sakane, K. Ooi, and T. Hirotsu, "Selective adsorption of phosphate from seawater and wastewater by amorphous zirconium hydroxide," *Journal of Colloid and Interface Science*, vol. 297, no. 2, pp. 426–433, 2006.
- [22] Z. Z. Huang, W. Q. Zhang, Y. D. Liu, H. J. TangBo, and Y. J. Zhu, "Adsorption characteristics of Hydrotalcite and the influencing factors," *Water Treatment Technology*, vol. 36, no. 8, pp. 49–52, 2010.
- [23] A. Genz, A. Kornmüller, and M. Jekel, "Advanced phosphorus removal from membrane filtrates by adsorption on activated aluminium oxide and granulated ferric hydroxide," *Water Research*, vol. 38, no. 16, pp. 3523–3530, 2004.
- [24] H. Ye, F. Chen, Y. Sheng, G. Sheng, and J. Fu, "Adsorption of phosphate from aqueous solution onto modified palygorskites," *Separation and Purification Technology*, vol. 50, no. 3, pp. 283–290, 2006.
- [25] J. Xie, C. J. Li, L. N. Chi, and D. Y. Wu, "Chitosan modified zeolite as a versatile adsorbent for the removal of different pollutants from water," *Fuel*, vol. 103, pp. 480–485, 2013.
- [26] L. L. Gan, J. N. Zuo, B. M. Xie, P. Li, and X. Huang, "Zeolite (Na) modified by nano-Fe particles adsorbing phosphate in rainwater runoff," *Journal of Environmental Sciences*, vol. 24, no. 11, pp. 1929–1933, 2012.
- [27] P. Ning, H.-J. Bart, B. Li, X. Lu, and Y. Zhang, "Phosphate removal from wastewater by model-La(III) zeolite adsorbents,"

- Journal of Environmental Sciences*, vol. 20, no. 6, pp. 670–674, 2008.
- [28] V. K. Jha, Y. Kameshima, A. Nakajima, and K. Okada, “Utilization of steel-making slag for the uptake of ammonium and phosphate ions from aqueous solution,” *Journal of Hazardous Materials*, vol. 156, no. 1–3, pp. 156–162, 2008.
- [29] J. Xiong, Z. He, Q. Mahmood, D. Liu, X. Yang, and E. Islam, “Phosphate removal from solution using steel slag through magnetic separation,” *Journal of Hazardous Materials*, vol. 152, no. 1, pp. 211–215, 2008.
- [30] L. Zeng, X. Li, and J. Liu, “Adsorptive removal of phosphate from aqueous solutions using iron oxide tailings,” *Water Research*, vol. 38, no. 5, pp. 1318–1326, 2004.
- [31] L. Johansson and J. P. Gustafsson, “Phosphate removal using blast furnace slags and opoka-mechanisms,” *Water Research*, vol. 34, no. 1, pp. 259–265, 2000.
- [32] N. I. Chubar, V. A. Kanibolotskyy, V. V. Strelko et al., “Adsorption of phosphate ions on novel inorganic ion exchangers,” *Colloids and Surfaces A*, vol. 255, no. 1–3, pp. 55–63, 2005.
- [33] R. Chitrakar, S. Tezuka, A. Sonoda, K. Sakane, K. Ooi, and T. Hirotsu, “Adsorption of phosphate from seawater on calcined MgMn-layered double hydroxides,” *Journal of Colloid and Interface Science*, vol. 290, no. 1, pp. 45–51, 2005.
- [34] J. Das, B. S. Patra, N. Baliarsingh, and K. M. Parida, “Adsorption of phosphate by layered double hydroxides in aqueous solutions,” *Applied Clay Science*, vol. 32, no. 3–4, pp. 252–260, 2006.
- [35] G. Zhang, H. Liu, R. Liu, and J. Qu, “Removal of phosphate from water by a Fe-Mn binary oxide adsorbent,” *Journal of Colloid and Interface Science*, vol. 335, no. 2, pp. 168–174, 2009.
- [36] O. R. Harvey and R. D. Rhue, “Kinetics and energetics of phosphate sorption in a multi-component Al(III)-Fe(III) hydr(oxide) sorbent system,” *Journal of Colloid and Interface Science*, vol. 322, no. 2, pp. 384–393, 2008.
- [37] G. Akay, B. Keskinler, A. Çakici, and U. Danis, “Phosphate removal from water by red mud using crossflow microfiltration,” *Water Research*, vol. 32, no. 3, pp. 717–726, 1998.
- [38] W. Huang, S. Wang, Z. Zhu et al., “Phosphate removal from wastewater using red mud,” *Journal of Hazardous Materials*, vol. 158, no. 1, pp. 35–42, 2008.
- [39] N. M. Agyei, C. A. Strydom, and J. H. Potgieter, “The removal of phosphate ions from aqueous solution by fly ash, slag, ordinary Portland cement and related blends,” *Cement and Concrete Research*, vol. 32, no. 12, pp. 1889–1897, 2002.
- [40] J. Chen, H. Kong, D. Wu, Z. Hu, Z. Wang, and Y. Wang, “Removal of phosphate from aqueous solution by zeolite synthesized from fly ash,” *Journal of Colloid and Interface Science*, vol. 300, no. 2, pp. 491–497, 2006.
- [41] C. Namasivayam and D. Sangeetha, “Equilibrium and kinetic studies of adsorption of phosphate onto ZnCl₂ activated coir pith carbon,” *Journal of Colloid and Interface Science*, vol. 280, no. 2, pp. 359–365, 2004.
- [42] X. Xu, B. Gao, W. Wang, Q. Yue, Y. Wang, and S. Ni, “Adsorption of phosphate from aqueous solutions onto modified wheat residue: characteristics, kinetic and column studies,” *Colloids and Surfaces B*, vol. 70, no. 1, pp. 46–52, 2009.
- [43] Z. Ma, Q. Li, Q. Yue et al., “Adsorption removal of ammonium and phosphate from water by fertilizer controlled release agent prepared from wheat straw,” *Chemical Engineering Journal*, vol. 171, no. 3, pp. 1209–1217, 2011.
- [44] J. B. Xiong and Q. Mahmood, “Adsorptive removal of phosphate from aqueous media by peat,” *Desalination*, vol. 259, no. 1–3, pp. 59–64, 2010.
- [45] H. Thakuria, B. M. Borah, and G. Das, “Macroporous metal oxides as an efficient heterogeneous catalyst for various organic transformations—a comparative study,” *Journal of Molecular Catalysis A*, vol. 274, no. 1–2, pp. 1–10, 2007.
- [46] B. Pan, J. Wu, B. Pan et al., “Development of polymer-based nanosized hydrated ferric oxides (HFOs) for enhanced phosphate removal from waste effluents,” *Water Research*, vol. 43, no. 17, pp. 4421–4429, 2009.
- [47] J. Dai, H. Yang, H. Yan, Y. Shangguan, Q. Zheng, and R. Cheng, “Phosphate adsorption from aqueous solutions by disused adsorbents: chitosan hydrogel beads after the removal of copper(II),” *Chemical Engineering Journal*, vol. 166, no. 3, pp. 970–977, 2011.
- [48] A. V. Esin and E. P. Ayse, “Preparation and characterization of pyrolytic chars from different biomass samples,” *Journal of Analytical and Applied Pyrolysis*, vol. 98, pp. 29–36, 2012.
- [49] Y. Liang, L. Y. Liang, and F. Y. Xu, “The study of corn straw liquefaction technology,” *Anhui Agricultural Sciences*, vol. 37, no. 27, pp. 13428–13429, 2009.
- [50] H. Qinglan, W. Chang, L. Dingqiang, W. Yao, L. Dan, and L. Guiju, “Production of hydrogen-rich gas from plant biomass by catalytic pyrolysis at low temperature,” *International Journal of Hydrogen Energy*, vol. 35, no. 17, pp. 8884–8890, 2010.
- [51] F. Abnisa, W. M. A. W. Daud W.M.A. Wan, W. N. W. Husin, and J. Sahu, “Utilization possibilities of palm shell as a source of biomass energy in Malaysia by producing bio-oil in pyrolysis process,” *Biomass and Bioenergy*, vol. 35, no. 5, pp. 1863–1872, 2011.
- [52] H. Y. Zhang, J. Zheng, R. Xiao et al., “Co-catalytic pyrolysis of biomass and waste triglyceride seed oil in a novel fluidized bed reactor to produce olefins and aromatics integrated with self-heating and catalyst regeneration processes,” *RSC Advances*, vol. 17, pp. 5769–5774, 2013.
- [53] F. Peng, P. W. He, Y. Luo, X. Lu, Y. Liang, and J. Fu, “Adsorption of phosphate by biomass char deriving from fast pyrolysis of biomass waste,” *Clean Soil, Air, Water*, vol. 40, no. 5, pp. 493–498, 2012.
- [54] Y. Chun, G. Sheng, G. T. Chiou, and B. Xing, “Compositions and sorptive properties of crop residue-derived chars,” *Environmental Science and Technology*, vol. 38, no. 17, pp. 4649–4655, 2004.
- [55] Y.-N. Chen, L.-Y. Chai, and Y.-D. Shu, “Study of arsenic(V) adsorption on bone char from aqueous solution,” *Journal of Hazardous Materials*, vol. 160, no. 1, pp. 168–172, 2008.
- [56] E. L. K. Mui, W. H. Cheung, M. Valix, and G. McKay, “Dye adsorption onto char from bamboo,” *Journal of Hazardous Materials*, vol. 177, no. 1–3, pp. 1001–1005, 2010.
- [57] G. Sheng, Y. Yang, M. Huang, and K. Yang, “Influence of pH on pesticide sorption by soil containing wheat residue-derived char,” *Environmental Pollution*, vol. 134, no. 3, pp. 457–463, 2005.
- [58] Z. L. Shi, F. M. Liu, and S. H. Yao, “Adsorptive removal of phosphate from aqueous solutions using activated carbon loaded with Fe(III) oxide,” *New Carbon Materials*, vol. 26, no. 4, pp. 299–306, 2011.
- [59] K. Sakadevan and H. J. Bavor, “Phosphate adsorption characteristics of soils, slags and zeolite to be used as substrates in constructed wetland systems,” *Water Research*, vol. 32, no. 2, pp. 393–399, 1998.
- [60] W. J. Weber and J. C. Morris, “Advances in water pollution research: removal of biologically resistant pollutant from waste water by adsorption,” in *Proceedings of the International Conference on Water Pollution Symposium*, vol. 2, pp. 231–266, Pergamon Press, Oxford, UK, 1962.

- [61] G. E. Boyd, A. W. Adamson, and L. S. Myers Jr., "The exchange adsorption of ions from aqueous solutions by organic zeolites. II. Kinetics," *Journal of the American Chemical Society*, vol. 69, no. 11, pp. 2836–2848, 1947.
- [62] J. Zhou, S. Yang, and J. Yu, "Facile fabrication of mesoporous MgO microspheres and their enhanced adsorption performance for phosphate from aqueous solutions," *Colloids and Surfaces A*, vol. 379, no. 1–3, pp. 102–108, 2011.
- [63] B. J. Tan, K. J. Klabunde, and P. M. A. Sherwood, "X-ray photoelectron spectroscopy studies of solvated metal atom dispersed catalysts. Monometallic iron and bimetallic iron-cobalt particles on alumina," *Chemistry of Materials*, vol. 2, no. 2, pp. 186–191, 1990.
- [64] V. V. Nemoshalenko, V. V. Didyk, V. P. Krivitskii, and A. I. Senekevich, "Study of the Change State of Atoms in Iron, Cobalt and Nickel Phosphides," *Zhurnal Neorganicheskoi Khimii*, vol. 28, p. 2182, 1983.
- [65] M. J. McGuire, J. Addai-Mensah, and K. E. Bremmell, "The effect of polymer structure type, pH and shear on the interfacial chemistry, rheology and dewaterability of model iron oxide dispersions," *Colloids and Surfaces A*, vol. 275, no. 1–3, pp. 153–160, 2006.

Research Article

Mesoporous Metal-Containing Carbon Nitrides for Improved Photocatalytic Activities

Jie Luo,¹ Zhao-Jie Cui,¹ and Guo-Long Zang²

¹ School of Environmental Science and Engineering, Shandong University, Jinan 250100, China

² Tianjin Renewable Resources Institute, All China Federation of Supply and Marketing Cooperatives, Tianjin 300191, China

Correspondence should be addressed to Zhao-Jie Cui; cuizj@sdu.edu.cn and Guo-Long Zang; guolongz@gmail.com

Received 30 September 2013; Accepted 14 October 2013

Academic Editor: Tifeng Jiao

Copyright © 2013 Jie Luo et al. This is an open access article distributed under the Creative Commons Attribution License, which permits unrestricted use, distribution, and reproduction in any medium, provided the original work is properly cited.

Graphitic carbon nitrides ($\text{g-C}_3\text{N}_4$) have attracted increasing interest due to their unusual properties and promising applications in water splitting, heterogeneous catalysis, and organic contaminant degradation. In this study, a new method was developed for the synthesis of mesoporous Fe contained $\text{g-C}_3\text{N}_4$ ($\text{m-Fe-C}_3\text{N}_4$) photocatalyst by using SiO_2 nanoparticles as hard template and dicyandiamide as precursor. The physicochemical properties of $\text{m-Fe-C}_3\text{N}_4$ were thoroughly investigated. The XRD and XPS results indicated that Fe was strongly coordinated with the $\text{g-C}_3\text{N}_4$ matrix and that the doping and mesoporous structure partially deteriorated its crystalline structure. The UV-visible absorption spectra revealed that $\text{m-Fe-C}_3\text{N}_4$ with a unique electronic structure displays an increased band gap in combination with a slightly reduced absorbance, implying that mesoporous structure modified the electronic properties of $\text{g-Fe-C}_3\text{N}_4$. The photocatalytic activity of $\text{m-Fe-C}_3\text{N}_4$ for photodegradation of Rhodamine B (RhB) was much higher than that of $\text{g-Fe-C}_3\text{N}_4$, clearly demonstrating porous structure positive effect.

1. Introduction

Carbon nitride has been widely regarded as the most promising candidate to complement carbon in materials applications. Among various carbon nitride compounds, graphitic carbon nitride ($\text{g-C}_3\text{N}_4$) is the most stable allotrope, which has attracted much attention for its potential application in splitting water, decomposing organic pollutants, and photosynthesis under visible light [1–5]. The polymeric $\text{g-C}_3\text{N}_4$ material contains graphitic stacking of C_3N_4 layers, which are constructed from tri-s-triazine units connected by planar amino groups [2, 6]. To further improve the performance of $\text{g-C}_3\text{N}_4$, many methods such as introducing functional atoms (B, F, S, P, etc.), controlling shape, and oxidation reaction have been used for its modification [1, 7–10].

One important way to improve its light utilization efficiency is to reduce the band gap and extend the light absorption range. Metal element dopants are usually introduced to prepare functional organic-metal hybrid material based on $\text{g-C}_3\text{N}_4$. Wang et al. firstly reported the synthesis of metal (Fe^{3+})-containing carbon nitride compounds using

dicyandiamide and metal chloride as precursors, and such synthesized carbon nitride showed high photocatalytic activities for the degradation of various organic dyes [11]. $\text{g-C}_3\text{N}_4$ photocatalyst was also modified with other transition metal elements (Co, Ni, Mn, Cu [12], or Zn [13]) to obtain the high photocatalytic activity and good stability. It also was active for the direct oxidation of benzene to phenol using hydrogen peroxide [14].

The porous structure can increase the semiconductor surface area, which contributes to an enhancement in energy conversion efficiency [15, 16]. Herein, we report the synthesis of porous $\text{m-Fe-C}_3\text{N}_4$ photocatalysts by using SiO_2 nanoparticles as template and dicyandiamide as precursor, and the physicochemical properties of synthesized $\text{m-Fe-C}_3\text{N}_4$ and $\text{g-Fe-C}_3\text{N}_4$ were characterized by X-ray diffractometer (XRD), transmission electron microscopy (TEM), UV-visible spectrophotometer (UV-vis), X-ray photoelectron spectroscopy (XPS), Fourier transform infrared (FTIR) spectra, and N_2 adsorption-desorption measurement. Moreover, their performance for photodegradation of Rhodamine B (RhB) was evaluated.

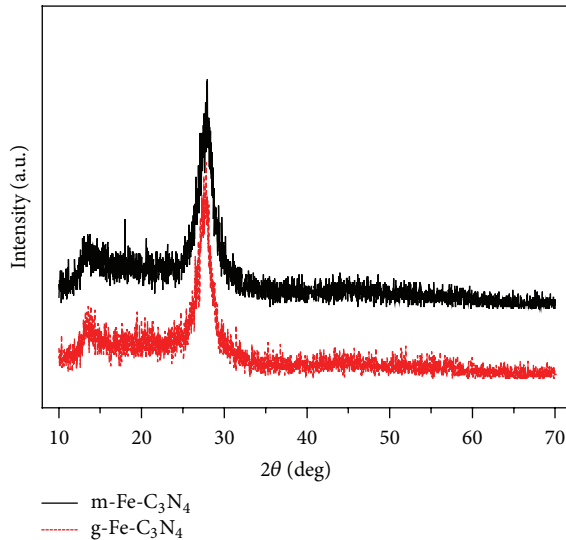


FIGURE 1: XRD patterns of the g-Fe-C₃N₄ and m-Fe-C₃N₄ samples.

2. Materials and Methods

2.1. Preparation of g-Fe-C₃N₄. Graphitic metal-containing carbon nitride compounds were synthesized according to the procedure reported previously [11]. Dicyandiamide was mixed with 0.12 g FeCl₃ in water (20 mL) under stirring, and then the mixed solution was heated at 100°C to remove water. The resulting powder was then heated at a rate of 2.3°C min⁻¹ for about 4 h to reach a temperature of 550°C and then held at this temperature for an additional 4 h under flowing nitrogen gas. The sample was then cooled to room temperature and was denoted as g-Fe-C₃N₄.

2.2. Preparation of m-Fe-C₃N₄. A 5 wt% dispersion of 15 ± 5 nm SiO₂ particles in water (20 mL) was heated and stirred at 100°C with dicyandiamide (4 g, Aldrich) and FeCl₃ (0.12 g) added. The mixed solution was treated following the same procedures as mentioned above to obtain high-temperature power. The resulting power was then stirred in 200 mL of 4 mol/L NH₄HF₂ for 12 h, followed by filtration and washing with water. After that, the sample was cooled to room temperature and was denoted as m-Fe-C₃N₄.

3. Characterization

The morphology of the samples were observed using transmission electron microscopy (TEM, JEM-2011, JEOL Co., Japan). The nitrogen adsorption-desorption isotherms and Brunauer-Emmett-Teller (BET) surface areas were measured using a TriStar II 3020M instrument at 77 K. The crystal properties of the samples were identified by an 18 kW rotating anode X-ray diffractometer (MAP18AHF, MAC Sci. Co., Japan). The optical absorbance spectra of the samples were recorded using a UV-visible spectrophotometer (SolidSpec-3700, Shimadzu Co., Japan). The samples were ground with KBr power and pressed to form a uniform disk prior to FTIR analysis (Magna-IR 750, Nicolet Instrument Co., USA).

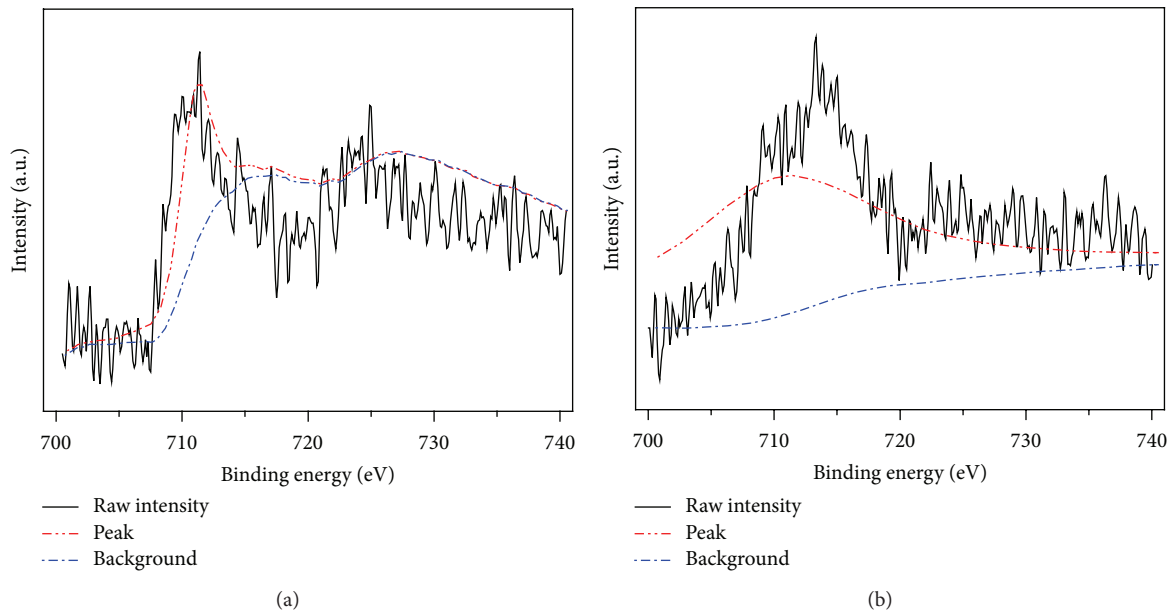
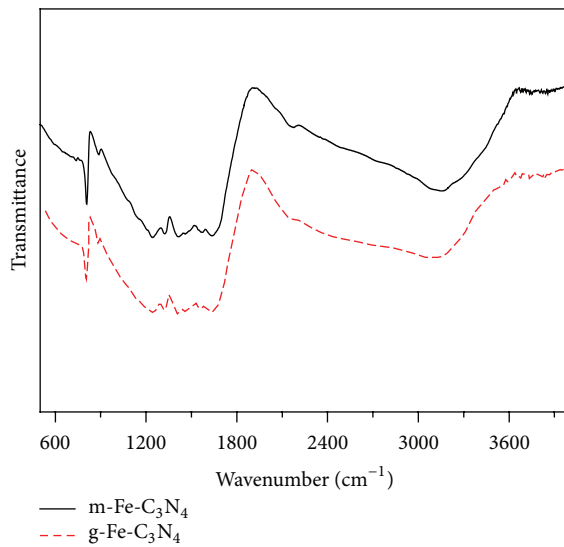
4. Photocatalytic Activity Measurement

Photocatalytic activities of samples for RhB degradation were evaluated with irradiation by a 500 W Xe lamp. In a Pyrex glass reactor, a total amount of 20 mg photocatalyst powder was dispersed in 40 mL of 5 mg L⁻¹ aqueous solution of RhB. One mL suspension was sampled at fixed time intervals during the reaction. The suspension was centrifuged to remove the photocatalyst and then the concentration variation of RhB was examined by UV-vis spectrophotometer (UV-2450, Shimadzu Co., Japan).

5. Results and Discussion

XRD data obtained from both g-Fe-C₃N₄ and m-Fe-C₃N₄ are illustrated in Figure 1. All these patterns indicate a structural similarity between g-Fe-C₃N₄ and m-Fe-C₃N₄. There were two peaks in both samples. The strongest peak at 27.6, corresponding to an interlayer distance of 0.33 nm, could be indexed as the (002) peak of the stacking of the conjugated aromatic system [17]. However, XRD peak originated from iron species was not found in both samples. This indicates that mesoporous structure of metal-containing carbon nitride compounds did not disrupt the crystal structure of graphitic metal-containing carbon nitride compounds. Thus, it could be inferred that the iron species in m-Fe-C₃N₄ was chemically coordinated to the g-C₃N₄ host [12].

To get insight into the surface functionalities created by mesoporous structure, XPS measurements were performed. XPS survey scan spectra show C1s and N1s peaks at 288.1 eV and 398.7 eV in both the g-Fe-C₃N₄ and m-Fe-C₃N₄ samples (data not shown). The C1s binding energy shows mainly one carbon species, corresponding to a C–N–C coordination. In the N1s spectrum the main signal shows the existence of C–N–C groups [18]. The assignment of peaks in the C1s and N1s spectra of two samples was in good agreement with the literature report [12]. It could be seen that C–N bonds were

FIGURE 2: XPS spectra of Fe2p for g-Fe-C₃N₄ (a) and m-Fe-C₃N₄ (b).FIGURE 3: FTIR spectra of the g-Fe-C₃N₄ and m-Fe-C₃N₄ samples.

not broken by doping Fe and the formation of mesoporous structure, while the mesoporous structure strengthened C1s and N1s peaks. The high resolution Fe2p XPS spectra shown in Figure 2 are characterized by a broad peak in the range of 700–740 eV. The typical XPS spectrum of m-Fe-C₃N₄ revealed a Fe2p binding energy peak at 710.1 eV, which was lower than the value of 711.2 eV measured for g-Fe-C₃N₄. They all fell within the range of binding energy of Fe(III) state, and only a small amount of Cl could be detected. This result implies that Fe(III) is connected to C₃N₄ framework mainly through Fe–N bonds, while little was used for charge balance by Cl[−] ions. Thus, Fe(III) in m-Fe-C₃N₄ might also be stabilized in the electron-rich C₃N₄ structure like g-Fe-C₃N₄.

Figure 3 shows the FTIR spectra of the g-Fe-C₃N₄ and m-Fe-C₃N₄ samples. They exhibit a peak at 808 cm⁻¹ and several other major bands from 1200 to 1700 cm⁻¹. The two samples show stretching modes in the 1200–1700 cm⁻¹ region, which were typical stretching modes of CN heterocycles originating from the extended C₃N₄ network [19], whereas the sharp band at about 808 cm⁻¹ should be attributed to ring-sextant bending vibration characteristic of triazine or heptazine ring systems [20, 21]. The results indicate that both the samples were chemically coordinated to the C₃N₄ host and formed no metal nitrides or metal carbides.

Figure 4 shows TEM images of the g-Fe-C₃N₄ and m-Fe-C₃N₄ samples. These results indicate that the pore size

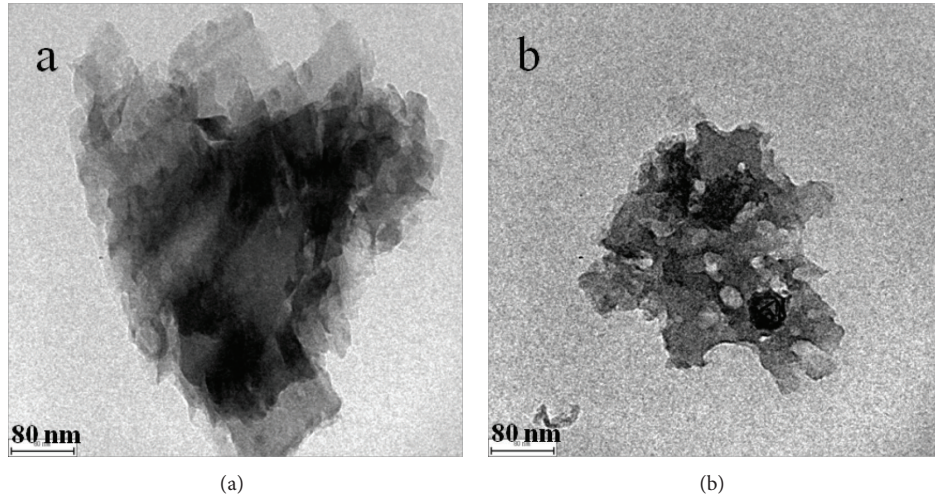


FIGURE 4: TEM images of the g-Fe-C₃N₄ and m-Fe-C₃N₄ samples.

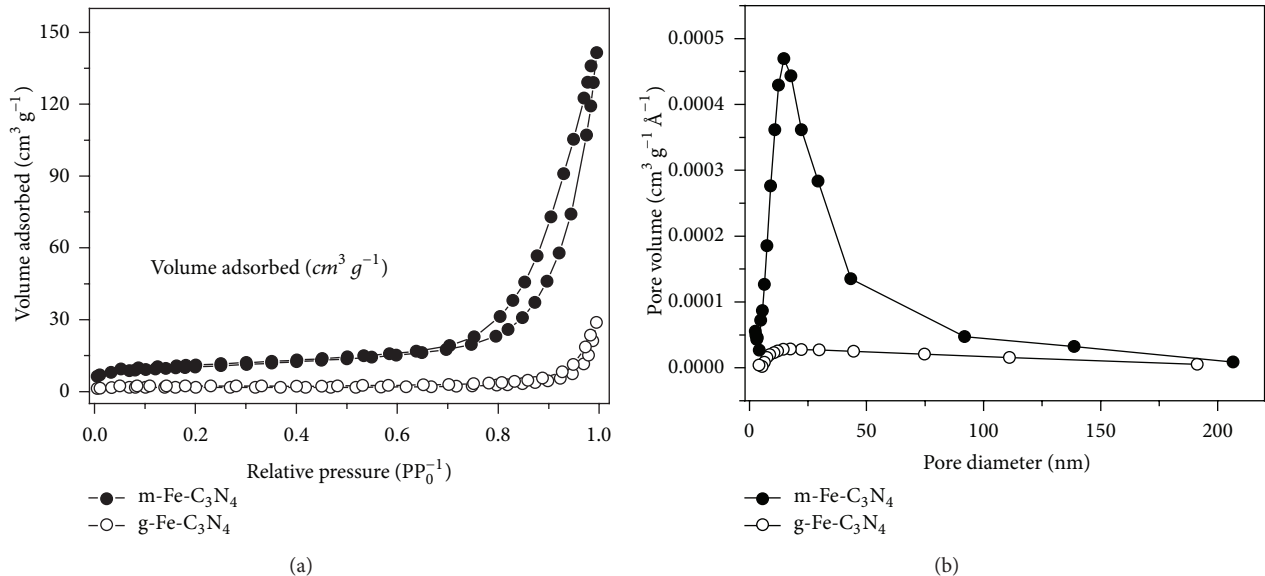


FIGURE 5: N₂ adsorption-desorption isotherms (a) and Barret-Joyner-Halenda (BJH) pore size distribution plots (b) of g-Fe-C₃N₄ and m-Fe-C₃N₄ samples.

and connectivity of those powders exactly reflect the geometric properties of the original template [2]. The g-Fe-C₃N₄ shows a graphitic-like and two-dimensional layer structure (Figure 4(a)), which is similar to that of pure g-C₃N₄. The TEM image of m-Fe-C₃N₄ in Figure 4(b) shows disordered pore system of spherical pores with diameter of 15–20 nm, which is consistent with the size of SiO₂ template. Compared to g-Fe-C₃N₄, m-Fe-C₃N₄ exhibited a slightly less dense structure and a higher surface area.

Figure 5 shows nitrogen adsorption/desorption isotherms of the g-Fe-C₃N₄ and m-Fe-C₃N₄ samples. The isotherms of both samples exhibit type III behavior according to the IUPAC classification, indicating the existence of porous structures in the samples [22]. The BET surface area of the m-Fe-C₃N₄ sample ($35.9 \text{ m}^2 \text{ g}^{-1}$) was much higher than that

of m-Fe-C₃N₄ sample ($5.7 \text{ m}^2 \text{ g}^{-1}$). The larger pore volume of m-Fe-C₃N₄ sample ($0.17 \text{ cm}^3 \text{ g}^{-1}$) suggested that it was more porous compared with that of g-Fe-C₃N₄ sample ($0.02 \text{ cm}^3 \text{ g}^{-1}$). An average pore diameter of 18.4 nm for m-Fe-C₃N₄ can be estimated from the BJH pore size distribution (Figure 5(b)). The pore size distribution of the two samples obtained from its absorption isotherm is consistent with the observed pore sizes from the TEM image. These results illustrate that m-Fe-C₃N₄ sample has been introduced with porous structure, which results in an increased surface area, enlarged pore volume, and narrow pore size distribution.

Figure 6 shows the optical absorbance spectra of the g-Fe-C₃N₄ and m-Fe-C₃N₄ samples. The absorption edge was at about 480 nm for g-Fe-C₃N₄ and 460 nm for m-Fe-C₃N₄, corresponding to the calculated band gap of ca. 2.58 and

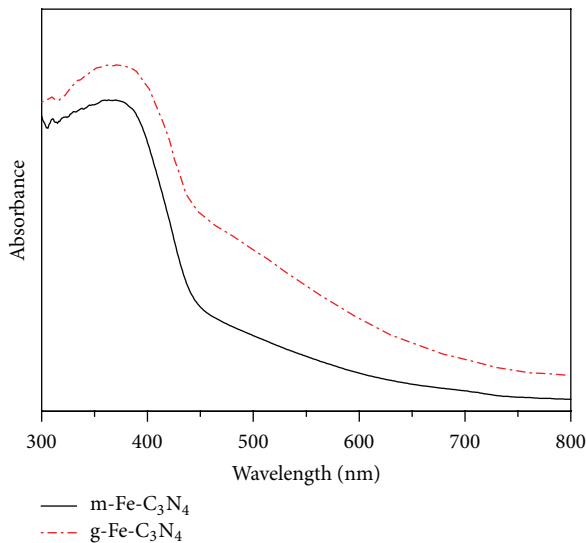


FIGURE 6: UV-vis absorption spectra of the g-Fe-C₃N₄ and m-Fe-C₃N₄ samples.

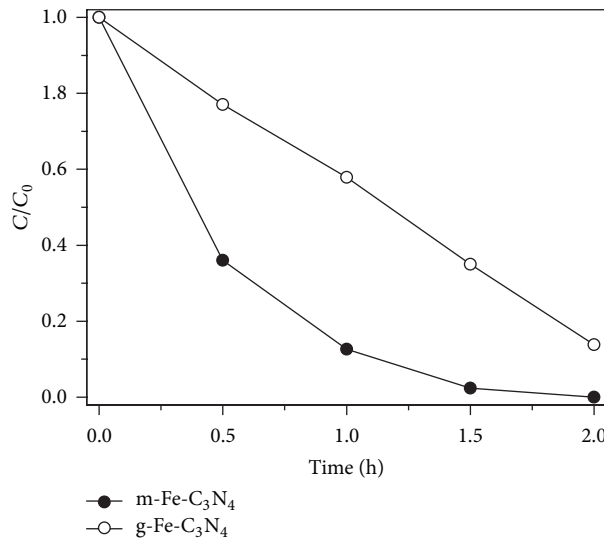


FIGURE 7: Comparison of the activities of g-Fe-C₃N₄ and m-Fe-C₃N₄ samples for RhB photocatalytic degradation.

2.70 eV, respectively. The comparison on the spectra of g-Fe-C₃N₄ and m-Fe-C₃N₄ samples indicates that the mesoporous structure of metal-containing carbon nitride compounds altered the electronic structure, and meantime the band gap was increased. Such structural change would lower the visible light response, though it might enhance the transport efficiencies of electrons and holes.

The photocatalytic performance of the resultant samples for RhB degradation under irradiation is shown in Figure 7. The results indicate that the mesoporous structure greatly influences the photocatalytic performance of g-Fe-C₃N₄ materials. The g-Fe-C₃N₄ showed a moderate photoreactivity toward organics degradation, which is consistent with the literature report [11]. Only ~42% of RhB was degraded in 60 min by g-Fe-C₃N₄ under irradiation, which is much lower than that of mesoporous samples. The m-Fe-C₃N₄ sample exhibits a higher photocatalytic activity, with nearly 88%

and 98% of RhB degraded after 60 and 90 min irradiation, respectively. The m-Fe-C₃N₄ sample showed much higher efficiency in RhB degradation than g-Fe-C₃N₄ under irradiation. It is known that the photooxidation reactions of organic molecules can directly utilize the generated valence band holes or the main generated active species, ·OH radicals, from the reaction of holes with surface adsorbed water or hydroxyl groups [10]. The mesoporous structure is beneficial for promoting the mass transfer of reactants and products, enhancing the photocatalytic activity by facilitating access to the reactive sites on the surface photocatalyst. Generally, a larger surface area of photocatalysts is favorable for photocatalytic reaction by providing more possible reaction sites [23]. In addition, the unique electronic structure of m-Fe-C₃N₄ may also contribute considerably to the excellent photooxidation reactivity.

6. Conclusions

In summary, *in situ* Fe-doped mesoporous g-C₃N₄ was synthesized from a single precursor, dicyandiamide, by using SiO₂ nanoparticles as the template. The XRD results indicate that Fe is strongly coordinated with the g-C₃N₄ matrix and that the doping and mesoporous structure partly deteriorates its crystalline structure. The XPS analysis confirmed that Fe species was coordinated with the g-Fe-C₃N₄ and m-Fe-C₃N₄ framework through Fe–N bonds. The UV-visible absorption spectra reveal that the absorption edge of g-Fe-C₃N₄ was redshifted from 460 nm of the m-Fe-C₃N₄ sample to 480 nm together with a stronger light absorbance, implying that the formation of mesoporous structure changes the electronic properties of g-Fe-C₃N₄. The obtained Fe-doped mesoporous g-C₃N₄ shows much higher activity than the g-Fe-C₃N₄ for RhB degradation. This activity enhancement could be attributed to the increased surface area and unique mesoporous structure.

References

- [1] Y. Wang, X. Wang, and M. Antonietti, “Polymeric graphitic carbon nitride as a heterogeneous organocatalyst: from photochemistry to multipurpose catalysis to sustainable chemistry,” *Angewandte Chemie—International Edition*, vol. 51, no. 1, pp. 68–89, 2012.
- [2] F. Goettmann, A. Fischer, M. Antonietti, and A. Thomas, “Chemical synthesis of mesoporous carbon nitrides using hard templates and their use as a metal-free catalyst for Friedel–Crafts reaction of benzene,” *Angewandte Chemie—International Edition*, vol. 45, no. 27, pp. 4467–4471, 2006.
- [3] X. Wang, K. Maeda, A. Thomas et al., “A metal-free polymeric photocatalyst for hydrogen production from water under visible light,” *Nature Materials*, vol. 8, no. 1, pp. 76–80, 2009.
- [4] P. Niu, G. Liu, and H. M. Cheng, “Nitrogen vacancy-promoted photocatalytic activity of graphitic carbon nitride,” *The Journal of Physical Chemistry C*, vol. 116, no. 20, pp. 11013–11018, 2012.
- [5] S. C. Yan, Z. S. Li, and Z. G. Zou, “Photodegradation performance of g-C₃N₄ fabricated by directly heating melamine,” *Langmuir*, vol. 25, no. 17, pp. 10397–10401, 2009.
- [6] M. Groenewolt and M. Antonietti, “Synthesis of g-C₃N₄ nanoparticles in mesoporous silica host matrices,” *Advanced Materials*, vol. 17, no. 14, pp. 1789–1792, 2005.
- [7] Y. Wang, H. Li, J. Yao, X. Wang, and M. Antonietti, “Synthesis of boron doped polymeric carbon nitride solids and their use as metal-free catalysts for aliphatic C–H bond oxidation,” *Chemical Science*, vol. 2, no. 3, pp. 446–450, 2011.
- [8] X. Wang, K. Maeda, X. Chen et al., “Polymer semiconductors for artificial photosynthesis: hydrogen evolution by mesoporous graphitic carbon nitride with visible light,” *Journal of the American Chemical Society*, vol. 131, no. 5, pp. 1680–1681, 2009.
- [9] Y. Wang, Y. Di, M. Antonietti, H. Li, X. Chen, and X. Wang, “Excellent visible-light photocatalysis of fluorinated polymeric carbon nitride solids,” *Chemistry of Materials*, vol. 22, no. 18, pp. 5119–5121, 2010.
- [10] G. Liu, P. Niu, C. Sun et al., “Unique electronic structure induced high photoreactivity of sulfur-doped graphitic C₃N₄,” *Journal of the American Chemical Society*, vol. 132, no. 33, pp. 11642–11648, 2010.
- [11] X. Wang, X. Chen, A. Thomas, X. Fu, and M. Antonietti, “Metal-containing carbon nitride compounds: a new functional organic–metal hybrid material,” *Advanced Materials*, vol. 21, no. 16, pp. 1609–1612, 2009.
- [12] Z. Ding, X. Chen, M. Antonietti, and X. Wang, “Synthesis of transition metal-modified carbon nitride polymers for selective hydrocarbon oxidation,” *ChemSusChem*, vol. 4, no. 2, pp. 274–281, 2011.
- [13] B. Yue, Q. Li, H. Iwai, T. Kako, and J. Ye, “Hydrogen production using zinc-doped carbon nitride catalyst irradiated with visible light,” *Science and Technology of Advanced Materials*, vol. 12, no. 3, Article ID 034401, 7 pages, 2011.
- [14] X. Chen, J. Zhang, X. Fu, M. Antonietti, and X. Wang, “Fe-g-C₃N₄-catalyzed oxidation of benzene to phenol using hydrogen peroxide and visible light,” *Journal of the American Chemical Society*, vol. 131, no. 33, pp. 11658–11659, 2009.
- [15] G. J. D. A. A. Soler-Illia, C. Sanchez, B. Lebeau, and J. Patarin, “Chemical strategies to design textured materials: from microporous and mesoporous oxides to nanonetworks and hierarchical structures,” *Chemical Reviews*, vol. 102, no. 11, pp. 4093–4138, 2002.
- [16] Y. Zhang, J. Liu, G. Wu, and W. Chen, “Porous graphitic carbon nitride synthesized via direct polymerization of urea for efficient sunlight-driven photocatalytic hydrogen production,” *Nanoscale*, vol. 4, no. 17, pp. 5300–5303, 2012.
- [17] F. Dong, L. Wu, Y. Sun, M. Fu, Z. Wu, and S. C. Lee, “Efficient synthesis of polymeric g-C₃N₄ layered materials as novel efficient visible light driven photocatalysts,” *Journal of Materials Chemistry*, vol. 21, no. 39, pp. 15171–15174, 2011.
- [18] A. Thomas, A. Fischer, F. Goettmann et al., “Graphitic carbon nitride materials: variation of structure and morphology and their use as metal-free catalysts,” *Journal of Materials Chemistry*, vol. 18, no. 41, pp. 4893–4908, 2008.
- [19] J. D. Hong, X. Y. Xia, Y. S. Wang, and R. Xu, “Mesoporous carbon nitride with *in situ* sulfur doping for enhanced photocatalytic hydrogen evolution from water under visible light,” *Journal of Materials Chemistry*, vol. 22, pp. 15006–15012, 2012.
- [20] B. V. Lotsch, M. Döblinger, J. Sehnert et al., “Unmasking melon by a complementary approach employing electron diffraction, solid-state NMR spectroscopy, and theoretical calculations—structural characterization of a carbon nitride polymer,” *Chemistry—A European Journal*, vol. 13, no. 17, pp. 4969–4980, 2007.
- [21] B. V. Lotsch and W. Schnick, “From triazines to heptazines: novel nonmetal tricyanomelamines as precursors for graphitic carbon nitride materials,” *Chemistry of Materials*, vol. 18, no. 7, pp. 1891–1900, 2006.
- [22] G. Dong and L. Zhang, “Porous structure dependent photoreactivity of graphitic carbon nitride under visible light,” *Journal of Materials Chemistry*, vol. 22, no. 3, pp. 1160–1166, 2012.
- [23] E. Martínez-Ferrero, Y. Sakatani, C. Boissière et al., “Nanostructured titanium oxynitride porous thin films as efficient visible-active photocatalysts,” *Advanced Functional Materials*, vol. 17, no. 16, pp. 3348–3354, 2007.

Research Article

Electrochemiluminescent Detection of Hydrogen Peroxide via Some Luminol Imide Derivatives with Different Substituent Groups

Tifeng Jiao,^{1,2} Qinjin Huang,¹ Yong Xiao,³ Xihai Shen,^{1,4} Jingxin Zhou,¹ and Faming Gao¹

¹ Hebei Key Laboratory of Applied Chemistry, School of Environmental and Chemical Engineering, Yanshan University, Qinhuangdao 066004, China

² State Key Laboratory of Solid Lubrication, Lanzhou Institute of Chemical Physics, Chinese Academy of Sciences, Lanzhou 730000, China

³ Environmental Protection Sciences Research Institute of Qinhuangdao City, Qinhuangdao 066001, China

⁴ College of Physics and Chemistry, Hebei Normal University of Science and Technology, Qinhuangdao 066004, China

Correspondence should be addressed to Tifeng Jiao; tfjiao@ysu.edu.cn

Received 28 September 2013; Accepted 21 October 2013

Academic Editor: Xinqing Chen

Copyright © 2013 Tifeng Jiao et al. This is an open access article distributed under the Creative Commons Attribution License, which permits unrestricted use, distribution, and reproduction in any medium, provided the original work is properly cited.

Some luminol imide derivatives with different substituent groups have been designed and synthesized. Their electrochemiluminescence properties have been measured with a view to developing new biosensors. The ECL response to hydrogen peroxide in the presence of these luminescent derivatives has been investigated taking into account crucial factors such as the applied potential value, injection volume of hydrogen peroxide, and the substituent groups in molecular structures. The experimental data demonstrated that the substituent groups in these imide derivatives can have a profound effect upon the ECL abilities of these studied compounds. The present research work affords new and useful exploration for the design and development of new soft matter for ECL biosensors with luminol functional groups.

1. Introduction

In recent several decades, in the development of biomimetic optoelectronic nanosensors, luminol is considered as an efficient system in chemiluminescence (CL) and electrochemiluminescence (ECL) measurements for the detection of hydrogen peroxide [1–3]. It is well-known that luminol CL in the presence of hydrogen peroxide can be produced through the action of a chemical catalyst like ferricyanide or a biocatalyst such as peroxidase. On the other hand, the application of a potential to oxidize luminol can successfully replace a catalyst to provoke luminol electrogenerated chemiluminescence with inherent high sensitivities and wide linear working ranges [4–8]. For this electrochemical process, as shown in Figure 1, screen-printed electrodes have been demonstrated to trigger luminol ECL as efficiently as glassy carbon macroelectrodes [9–12].

In the previous work, we reported the design and synthesis of functional luminol derivatives with different substituted groups and investigated the interfacial assembly of these compounds with different methods [13–15]. At the same time, their potential for ECL measurement has been demonstrated first [16]. Meanwhile, their interfacial behavior and the morphologies of pure or mixed monolayers used to develop the biomimetic membrane were investigated [17]. The introduction of different substituted groups into those functional compounds can lead to new conjugated structures and new properties are expected. In addition, some luminol imide derivatives with different alkyl substituent chains could form different organogels in various organic solvents [18]. Characterization of the organogels revealed different structures of the aggregates in the gels. We have investigated the effect of the length and number of alkyl substituent chains in gelators

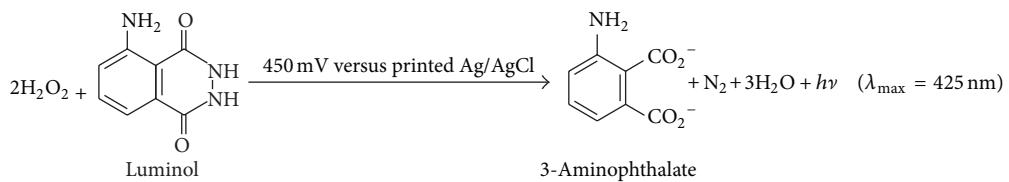


FIGURE 1: Electrochemiluminescence (ECL) reaction of luminol in the presence of hydrogen peroxide.

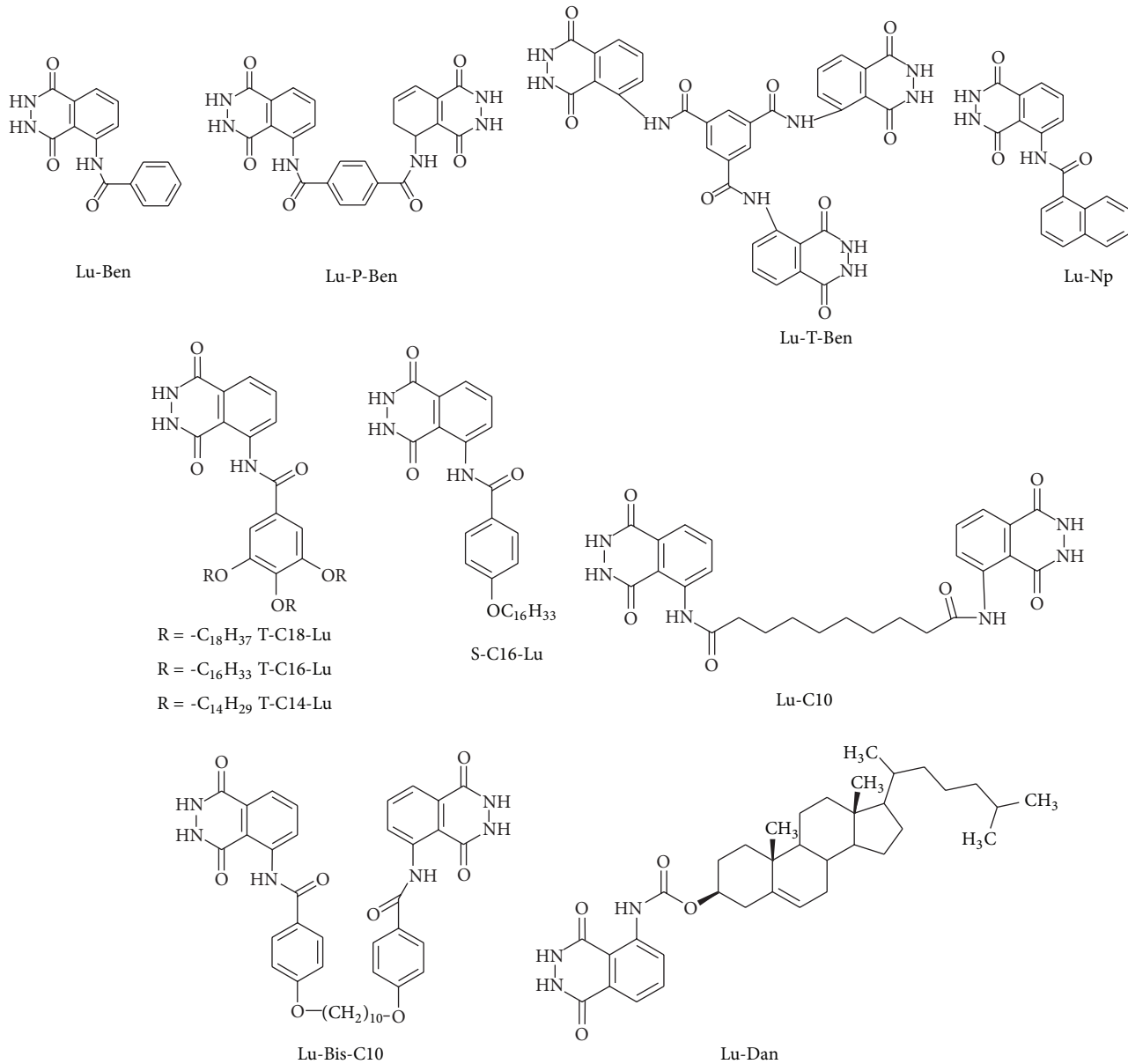


FIGURE 2: Molecular structures and abbreviations of present luminol derivatives with different substituent groups.

on the microstructures of such organogels in detail and found different kinds of hydrogen bond interactions between amide groups.

As an extension work, we reported here the electro-chemiluminescence properties of functional luminol derivative containing different substituted groups with a view to developing new biosensors. The ECL response to hydrogen

peroxide in the presence of these luminescent derivatives has been investigated taking into account crucial factors such as the applied potential value, injection volume of hydrogen peroxide, and the substituent groups in molecular structures. The present results may give useful clues for the design and development of new ECL biosensors with luminol functional groups.

2. Experiments

2.1. Reagents. All materials, luminol, cholestryl chloroformate, benzoyl chloride, 1-naphthoyl chloride, methyl 3,4,5-trihydroxybenzoate, 4-hydroxybenzenecarboxylic acid, and other used reagents were obtained commercially from Alfa Aesar Chemicals, TCI Shanghai Chemicals, Sinopharm Chemical Reagent Co., Ltd (China), and used without further purification. All used solvents were obtained from Beijing Chemicals and were distilled before use. Deionized water was used in all cases. 4-Alkyloxy-benzoic acid and 3,4,5-tris(alkyloxy)benzoic acid with different alkyl substituent chains were synthesized in our laboratory according to our previous report [19] and confirmed by ^1H NMR. These luminol derivatives were synthesized by the reaction of the corresponding chloride precursors with luminol according to slight modifications of procedures already reported in the literature [20, 21]. The final products and their abbreviations are shown in Figure 2, which were confirmed by ^1H NMR.

2.2. Apparatus. The ECL setup was described previously in our reports [17]. The screen-printed sensor ($4\text{ cm} \times 0.6\text{ cm}$) was comprised of a graphite working electrode (0.19 cm^2) and a printed Ag/AgCl reference electrode (0.30 cm^2). The screen-printed sensor is connected to a potentiostat. A liquid core optical fiber connected at one end to the photomultiplier tube of a luminometer faced the electrode. Electrochemiluminescence measurements in arbitrary units (a.u.) were recorded with a graphic recorder.

2.3. Characterization. Stock solutions of luminol and present luminol derivatives were dispersed into PBS buffer (pH 8.0) under vigorous stirring prior to use to avoid any precipitation. The screen-printed sensor was immersed in a glass cuvette protected by black paper to avoid light and filled with a PBS buffer (pH 8.0) containing luminol or its derivatives. After the application of a cyclic voltammetry potential (between 450 mV and 850 mV versusprinted Ag/AgCl) and stabilization of the luminescent background signal, the ECL reaction was initiated by the injection of hydrogen peroxide solution in the buffer-filled cell. A steady-state light signal was reached after *ca.* 1 min. The working condition (PBS buffer, pH 9.0, 25°C) was optimized for ECL detection to perform below measurements.

3. Results and Discussion

3.1. Effect of Some Factors on ECL Detection. It was reported previously that the screen-printed electrodes can be efficiently used in PBS buffer (pH 8.0). In addition, a cyclic voltammetry potential of $-0.40\text{ V} \sim -0.80\text{ V}$ versusprinted Ag/AgCl was described as an optimized value for hydrogen peroxide-detecting optical fiber biosensors based on luminol ECL. In the present work, the best optimal potential value for ECL of luminol derivatives is required to be determined. Consequently, the relationship of ECL intensity as a function of potential was investigated, as shown in Figure 3. For the case of T-C14-Lu, 30 uL (50 uM) hydrogen peroxide solution

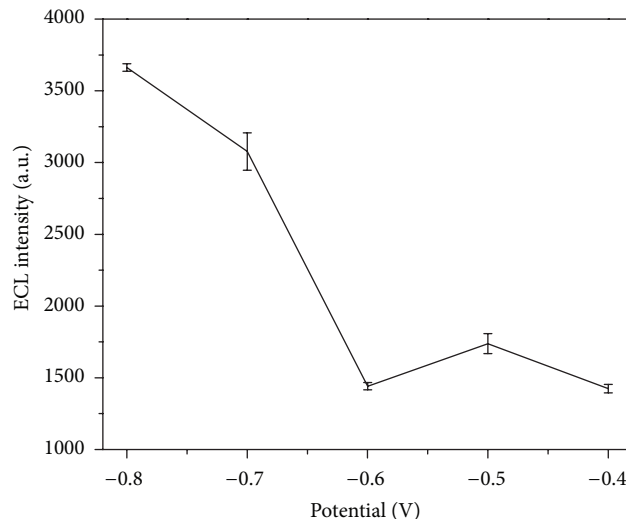


FIGURE 3: ECL intensity as a function of potential for T-C14-Lu. The measurements were performed in PBS buffer (pH 8.0) containing 50 uM of T-C14-Lu. The ECL reaction was initiated by sequential injection of 30 uL hydrogen peroxide solution in the working medium.

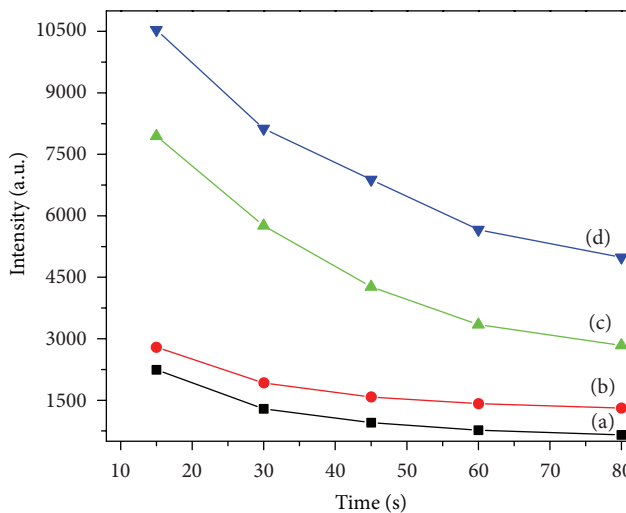


FIGURE 4: Calibration curves for hydrogen peroxide detection. The measurements were performed in PBS buffer (pH 8.0) containing Lu-P-Ben at concentrations of 50 uM. The ECL reaction was initiated by sequential injections of hydrogen peroxide in the working medium at volumes of 10 uL (a), 20 uL (b), 30 uL (c), and 40 uL (d), respectively.

was injected to the working medium. In the same concentration of hydrogen peroxide solution, it can be observed that with the increment of potential value from -0.45 V to -0.80 V , ECL intensity increased. So, the value of 0.80 V was preferred to measure other present systems.

In addition, at a potential value of -0.80 V , the ECL detection with different concentrations of hydrogen peroxide detection was performed for Lu-P-Ben, as shown in Figure 4. The measurements were performed in PBS buffer (pH 8.0)

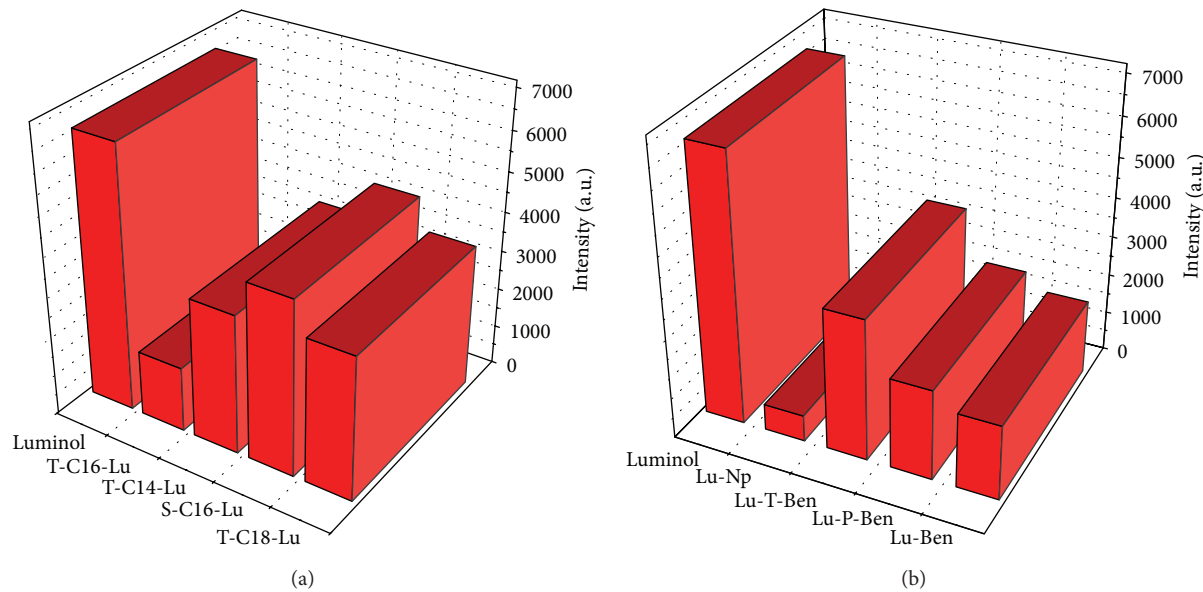


FIGURE 5: Calibration columns for ECL detection of hydrogen peroxide. The measurements were performed in PBS buffer (pH 8.0). The ECL reaction was initiated by sequential injection of 30 uL hydrogen peroxide in the working medium.

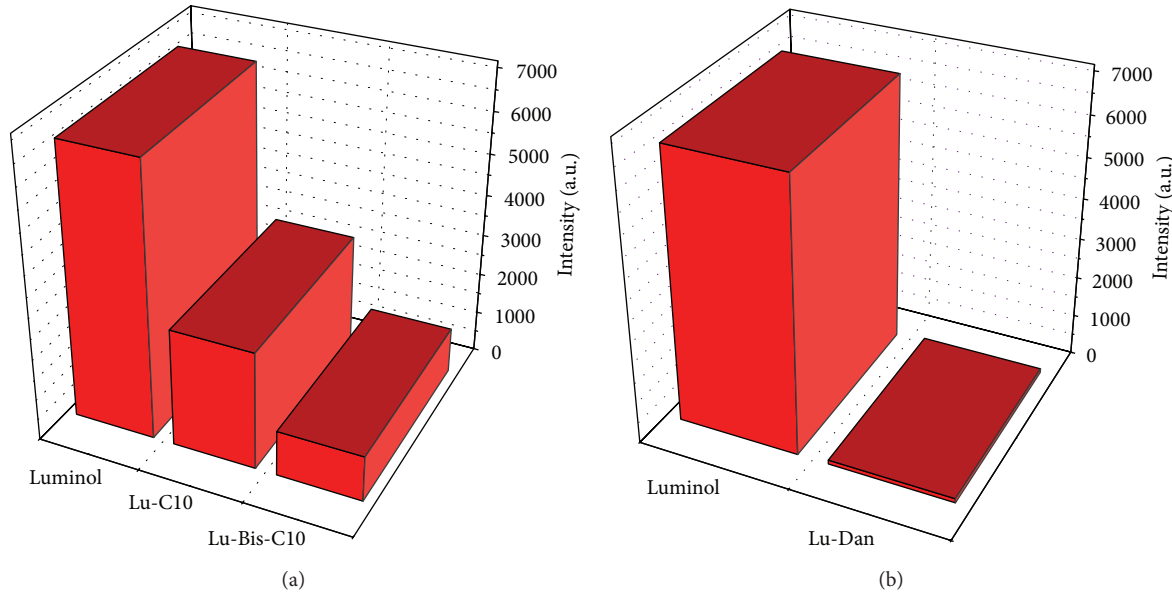


FIGURE 6: Calibration columns for ECL detection of hydrogen peroxide. The measurements were performed in PBS buffer (pH 8.0). The ECL reaction was initiated by sequential injection of 30 uL hydrogen peroxide in the working medium.

containing Lu-P-Ben at concentrations of 50 uM. The ECL reaction was initiated by sequential injections of hydrogen peroxide in the working medium at different volumes. It can be observed that with the increment of injection volumes of hydrogen peroxide in the working medium, ECL intensity increased with nonlinear style. The ECL intensity is not strong enough with low injection volumes due to the delay in the dispersion process. So, the injection volume of 30 uL for hydrogen peroxide was chosen to measure the next research work.

Moreover, ECL measurements of luminol derivatives with different substituted groups were compared, as shown in

Figures 5 and 6, respectively. The measurements were performed in PBS buffer (pH 8.0). The ECL reaction was initiated by sequential injection of 30 uL hydrogen peroxide in the working medium. Firstly, the ECL intensities of luminol derivatives with single/multialkyl chains connected to benzene ring substituted groups were compared. The results showed that among the present four compounds, S-C16-Lu with single alkyl chain showed better ECL property than the other compounds with multialkyl chains. In addition, as for the present luminol derivatives with aromatic substituted groups, Lu-T-Ben with C3-symmetrical skeleton showed

better ECL behaviors than those of the other compounds with phenyl or naphthyl substituted groups. Interestingly, it should be noted that Lu-Dan with large cholesteryl substituted group showed a weaker ECL property than that of the luminol. For all luminol derivatives, the ECL properties showed a more decrement tendency than that of the luminol, which may be due to the weak solubility, poor dispersion in water, and effect of substituted groups.

3.2. Discussion. In our previous work, we reported the synthesis and characterization of some luminol derivatives containing aromatic/alkyl substituted groups [13, 14]. The introduction of different aromatic substituted groups into the present functional compounds can lead to larger conjugated structures and new properties are expected. At the same time, the size and rigidity/flexibility of functional amphiphiles could regulate the potential properties both in solution and at interface, which demonstrated the advantage of precise molecular design. In addition, we have found that most compounds could form different organogels in various organic solvents [18]. We have investigated the effect of the length and number of alkyl substituent chains in gelators on the microstructures of organogels in detail and found different kinds of hydrogen bond interactions between amide groups. Therein, the alkyl substituent chains in luminol derivatives had played a very important role in regulating the assembly modes and nanostructures in these organogels. Now, the ECL properties generated by the present luminol derivatives in the presence of choline chloride and choline oxidase are under investigation to display the relationship between the molecular structures, as-formed nanostructures, and ECL sensors [22].

4. Conclusions

Some luminol imide derivatives with different substituent groups have been designed and synthesized. Their electrochemiluminescence properties have been measured with a view to developing new biosensors. The ECL response to hydrogen peroxide in the presence of these luminescent derivatives has been investigated taking into account crucial factors such as the applied potential value, injection volume of hydrogen peroxide, and the substituent groups in molecular structures. The experimental data demonstrated that the substituent groups in these imide derivatives can have a profound effect upon the ECL abilities of these studied compounds. The present research work affords new and useful exploration for the design and development of new soft matter for ECL biosensors with luminol functional groups.

Conflict of Interests

The authors declare that they have no direct financial relation with the commercial identities mentioned in this paper that might lead to a conflict of interests for any of them.

Acknowledgments

This work was financially supported by the National Natural Science Foundation of China (Grant nos. 20903078,

21207112), the Natural Science Foundation of Hebei Province (Grant nos. B2012203060, B2013203108), the China Postdoctoral Science Foundation (Grant nos. 2011M500540, 2012M510770, and 2013T60265), the Science Foundation for the Excellent Youth Scholars from Universities and Colleges of Hebei Province (Grant nos. Y201113, YQ2013026), the Scientific Research Foundation for Returned Overseas Chinese Scholars of Hebei Province (Grant no. 2011052), and the Open Foundation of State Key Laboratory of Solid Lubrication (Grant no. 1002).

References

- [1] B. Leca and L. J. Blum, "Luminol electrochemiluminescence with screen-printed electrodes for low-cost disposable oxidase-based optical sensors," *Analyst*, vol. 125, no. 5, pp. 789–791, 2000.
- [2] S. Sakura, "Electrochemiluminescence of hydrogen peroxide-luminol at a carbon electrode," *Analytica Chimica Acta*, vol. 262, no. 1, pp. 49–57, 1992.
- [3] C. A. Marquette and L. J. Blum, "Electro-chemiluminescent bio-sensing," *Analytical and Bioanalytical Chemistry*, vol. 390, no. 1, pp. 155–168, 2008.
- [4] V. C. Tsafack, C. A. Marquette, B. Leca, and L. J. Blum, "An electrochemiluminescence-based fibre optic biosensor for choline flow injection analysis," *Analyst*, vol. 125, no. 1, pp. 151–155, 2000.
- [5] A. Sassolas, L. J. Blum, and B. D. Leca-Bouvier, "Electrogeneration of polyluminol and chemiluminescence for new disposable reagentless optical sensors," *Analytical and Bioanalytical Chemistry*, vol. 390, no. 3, pp. 865–871, 2008.
- [6] S. Godoy, B. Leca-Bouvier, P. Boullanger, L. J. Blum, and A. P. Girard-Egrot, "Electrochemiluminescent detection of acetylcholine using acetylcholinesterase immobilized in a biomimetic Langmuir-Blodgett nanostructure," *Sensors and Actuators B*, vol. 107, no. 1, pp. 82–87, 2005.
- [7] L. J. Blum, S. M. Gautier, and P. R. Coulet, "Design of luminescence photobiosensors," *Journal of Bioluminescence and Chemiluminescence*, vol. 4, no. 1, pp. 543–550, 1989.
- [8] C. A. Marquette and L. J. Blum, "Luminol electrochemiluminescence-based fibre optic biosensors for flow injection analysis of glucose and lactate in natural samples," *Analytica Chimica Acta*, vol. 381, no. 1, pp. 1–10, 1999.
- [9] L. Zhu, Y. Li, and G. Zhu, "A novel flow through optical fiber biosensor for glucose based on luminol electrochemiluminescence," *Sensors and Actuators B*, vol. 86, no. 2–3, pp. 209–214, 2002.
- [10] S. Godoy, S. Violot, P. Boullanger et al., "Kinetics study of *Bungarus fasciatus* venom acetylcholinesterase immobilised on a Langmuir-Blodgett proteo-glycolipidic bilayer," *ChemBioChem*, vol. 6, no. 2, pp. 395–404, 2005.
- [11] A. P. Girard-Egrot, S. Godoy, and L. J. Blum, "Enzyme association with lipidic Langmuir-Blodgett films: interests and applications in nanobioscience," *Advances in Colloid and Interface Science*, vol. 116, no. 1–3, pp. 205–225, 2005.
- [12] P. Boullanger, M.-R. Sancho-Camborieu, M.-N. Bouchu, L. Marron-Brignone, R. M. Morelis, and P. R. Coulet, "Synthesis and interfacial behavior of three homologous glycerol neoglycolipids with various chain lengths," *Chemistry and Physics of Lipids*, vol. 90, no. 1–2, pp. 63–74, 1997.
- [13] T. Jiao, Y. Xing, and J. Zhou, "Synthesis and characterization of functional cholesteryl substituted luminol derivative," *Materials Science Forum*, vol. 694, pp. 565–569, 2011.

- [14] T. F. Jiao, Y. Y. Xing, J. X. Zhou, and W. Wang, "Synthesis and characterization of some functional luminol derivatives with aromatic substituted groups," *Advanced Materials Research*, vol. 197-198, pp. 606–609, 2011.
- [15] T. Jiao, B. D. Leca-Bouvier, P. Boullanger, L. J. Blum, and A. P. Girard-Egrot, "Phase behavior and optical investigation of two synthetic luminol derivatives and glycolipid mixed monolayers at the air-water interface," *Colloids and Surfaces A*, vol. 321, no. 1–3, pp. 137–142, 2008.
- [16] T. Jiao, B. D. Leca-Bouvier, P. Boullanger, L. J. Blum, and A. P. Girard-Egrot, "Electrochemiluminescent detection of hydrogen peroxide using amphiphilic luminol derivatives in solution," *Colloids and Surfaces A*, vol. 321, no. 1–3, pp. 143–146, 2008.
- [17] T. Jiao, B. D. Leca-Bouvier, P. Boullanger, L. J. Blum, and A. P. Girard-Egrot, "A chemiluminescent Langmuir-Blodgett membrane as the sensing layer for the reagentless monitoring of an immobilized enzyme activity," *Colloids and Surfaces A*, vol. 354, no. 1–3, pp. 284–290, 2010.
- [18] T. F. Jiao, Q. Q. Huang, Q. R. Zhang, D. B. Xiao, J. X. Zhou, and F. M. Gao, "Self-assembly of organogels via new luminol imide derivatives: diverse nanostructures and substituent chain effect," *Nanoscale Research Letters*, vol. 8, no. 1, article 278, 2013.
- [19] H. Yang, T. Yi, Z. Zhou et al., "Switchable fluorescent organogels and mesomorphic superstructure based on naphthalene derivatives," *Langmuir*, vol. 23, no. 15, pp. 8224–8230, 2007.
- [20] Y. Omote, T. Miyake, S. Ohmori, and N. Sugiyama, "The chemiluminescence of acyl luminols," *Bulletin of the Chemical Society of Japan*, vol. 39, no. 5, pp. 932–935, 1966.
- [21] Y. Omote, T. Miyake, S. Ohmori, and N. Sugiyama, "The chemiluminescence of luminol and acetyl-luminol," *Bulletin of the Chemical Society of Japan*, vol. 40, no. 5, pp. 899–903, 1967.
- [22] A. P. Girard-Egrot, C. A. Marquette, and L. J. Blum, "Biomimetic membranes and biomolecule immobilisation strategies for nanobiotechnology applications," *International Journal of Nanotechnology*, vol. 7, no. 4–8, pp. 753–780, 2010.